National Library
of Canada

Acquisitions and
Bibliographic Services Branch

395 Wellington Street
Ottawa, Ontario
K1A 0N4

Bibliothèque nationale
du Canada

Direction des acquisitions et
des services bibliographiques

395, rue Wellington
Ottawa (Ontario)
K1A 0N4

Your file Votre référence

Our file Notre référence

NOTICE

The quality of this microform is heavily dependent upon the quality of the original thesis submitted for microfilming. Every effort has been made to ensure the highest quality of reproduction possible.

If pages are missing, contact the university which granted the degree.

Some pages may have indistinct print especially if the original pages were typed with a poor typewriter ribbon or if the university sent us an inferior photocopy.

Reproduction in full or in part of this microform is governed by the Canadian Copyright Act, R.S.C. 1970, c. C-30, and subsequent amendments.

AVIS

La qualité de cette microforme dépend grandement de la qualité de la thèse soumise au microfilmage. Nous avons tout fait pour assurer une qualité supérieure de reproduction.

S'il manque des pages, veuillez communiquer avec l'université qui a conféré le grade.

La qualité d'impression de certaines pages peut laisser à désirer, surtout si les pages originales ont été dactylographiées à l'aide d'un ruban usé ou si l'université nous a fait parvenir une photocopie de qualité inférieure.

La reproduction, même partielle, de cette microforme est soumise à la Loi canadienne sur le droit d'auteur, SRC 1970, c. C-30, et ses amendements subséquents.

Canada

DISEQUILIBRIUM TEXTURES IN THE CENTRE HILL COMPLEX, MUNRO TOWNSHIP, ONTARIO

by

Robert Thériault

A thesis submitted to the School of Graduate Studies
in partial fulfillment of the requirements
for the degree of M.Sc. in Geology

© Robert Thériault, Ottawa, Canada, 1992

National Library
of Canada

Acquisitions and
Bibliographic Services Branch

395 Wellington Street
Ottawa, Ontario
K1A 0N4

Bibliothèque nationale
du Canada

Direction des acquisitions et
des services bibliographiques

395, rue Wellington
Ottawa (Ontario)
K1A 0N4

Your file Votre référence

Our file Notre référence

The author has granted an irrevocable non-exclusive licence allowing the National Library of Canada to reproduce, loan, distribute or sell copies of his/her thesis by any means and in any form or format, making this thesis available to interested persons.

L'auteur a accordé une licence irrévocable et non exclusive permettant à la Bibliothèque nationale du Canada de reproduire, prêter, distribuer ou vendre des copies de sa thèse de quelque manière et sous quelque forme que ce soit pour mettre des exemplaires de cette thèse à la disposition des personnes intéressées.

The author retains ownership of the copyright in his/her thesis. Neither the thesis nor substantial extracts from it may be printed or otherwise reproduced without his/her permission.

L'auteur conserve la propriété du droit d'auteur qui protège sa thèse. Ni la thèse ni des extraits substantiels de celle-ci ne doivent être imprimés ou autrement reproduits sans son autorisation.

ISBN 0-315-85849-4

Canada

UNIVERSITÉ D'OTTAWA
UNIVERSITY OF OTTAWA

The basic mechanism of evolution is based on the play between bifurcations as mechanisms of exploration and the selection of chemical interactions stabilizing a particular trajectory.

- ILYA PRIGOGINE

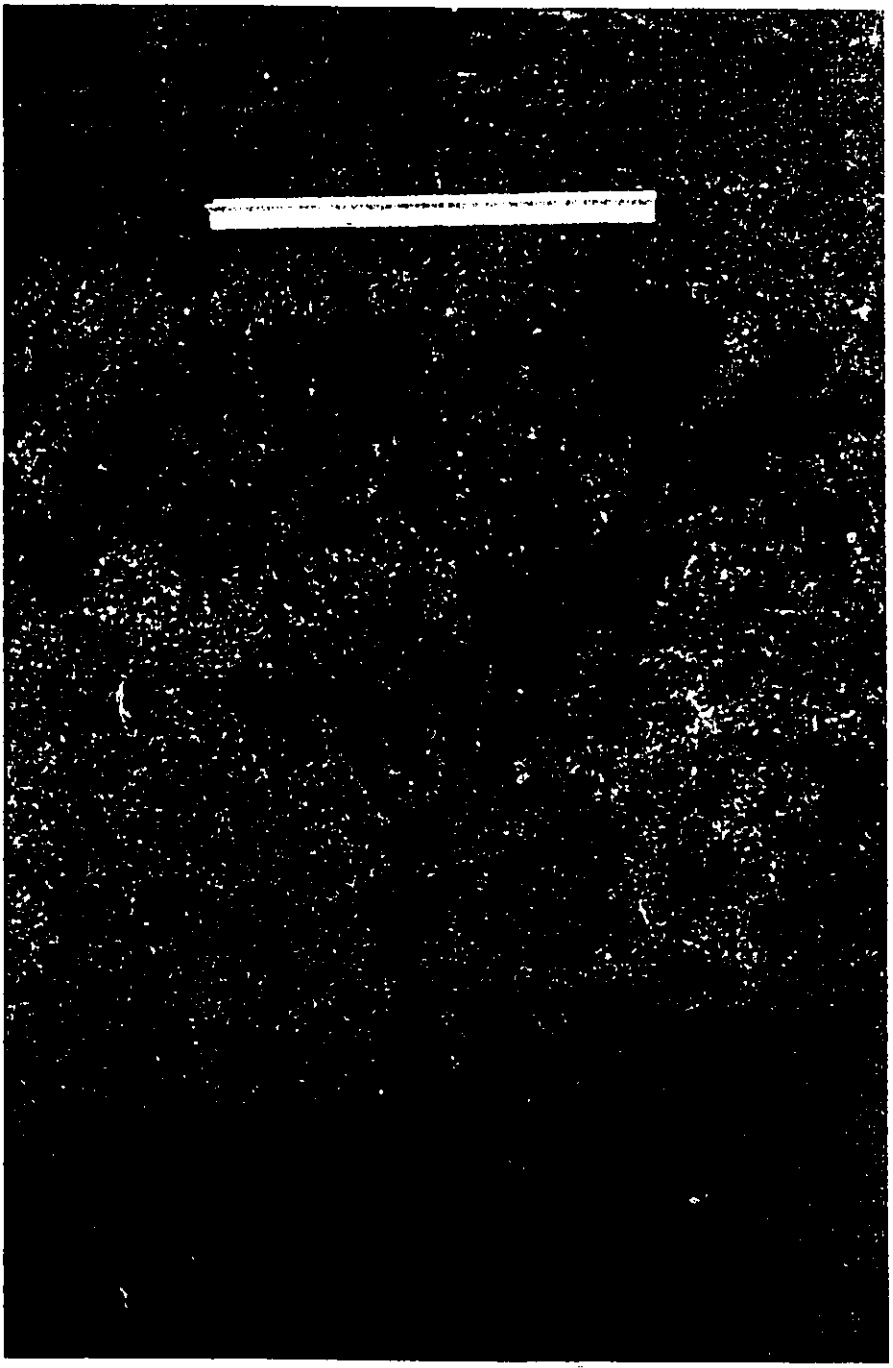

ABSTRACT

The Centre Hill complex is part of the mafic to ultramafic Munro Lake sill that occurs within the Stoughton-Roquemaure Group of the Abitibi Subprovince. The complex is approximately 450 m thick and consists of alternating layers of peridotite and clinopyroxenite overlain by 250 m of gabbroic rocks. Two distinct occurrences of cyclic layering are observed: 1) cyclic units of peridotite and clinopyroxenite in the bottom half of the intrusion; and 2) cyclic units of branching-textured gabbro (BTG) and clotted-textured gabbro (CTG) characteristic of the upper layer of gabbro. It is proposed that both types of cyclic units are genetically related and associated with periodic replenishment of parental magma to the chamber.

The upper part of the gabbro is characterized by the presence of spectacular branching crystals that extend away from the upper contact. The primary composition of the branches is interpreted to have been that of Fe-rich olivine based on the actual secondary assemblage. From petrological observations and geochemical data, it is suggested that the branching olivine crystals grew within a crystal-liquid mush in the later stages of fractionation. Two models based on their appearance within the petrogenetic sequence are proposed: 1) the branching olivine crystals grew from the residual melt of the last batch of magma only; or 2) the branching olivine crystallized in the later stages of each cyclic event.

The branching textures are truly fractal objects as they are self-similar over a large range of scale. They consistently yield fractal dimensions approximating 1.6. The branching morphologies were qualitatively and quantitatively simulated on the computer using a variation of the Witten-Sander diffusion limited aggregation (DLA) algorithm. From the simulations, it is established that the growth of branching crystals was limited by diffusion of molecules to the crystal-liquid interface, and that the resulting morphology was controlled by two opposing phenomenon: 1) the random aggregation of growth molecules along the crystal periphery without relocation; and 2) the systematic arrangement of molecules onto the growing interface according to the internal crystal structure of the mineral.

Other factors that may have contributed to the development of the branching olivine crystals include: 1) the high concentration of olivine components in the melt; 2) the very low nucleation rate of olivine; 3) the rapid growth of olivine crystals; and 4) the viscous nature of the residual liquid.

SOMMAIRE

Le complexe de Centre Hill fait partie du filon-couche stratifié de Munro Lake, lequel se trouve dans le Groupe Stoughton-Roquemaure de la Province de l'Abitibi. Le complexe est d'une épaisseur approximative de 450 mètres, et est formé d'une alternance de peridotites et de clinopyroxenites, recouvert d'environ 250 mètres de roches gabbroïques. On observe deux cas de stratification cyclique: 1) dans la partie inférieure de l'intrusion, sous forme d'unités cycliques de peridotite et de clinopyroxenite; et 2) dans la couche supérieure de gabbro, sous forme d'unités cycliques de gabbro à textures en forme de branches et de gabbro à textures en forme de grumeaux. Il est proposé que ces deux types de stratification cyclique sont génétiquement liés, et associés à un réapprovisionnement périodique de magma dans le réservoir.

La couche supérieure de gabbro est caractérisée par la présence de spectaculaires cristaux en forme de branches s'étendant vers l'intérieur en s'éloignant du sommet du filon. L'assemblage métamorphique actuel de ces roches nous permet de déduire que la composition primaire des cristaux était celle d'une olivine riche en fer. Les cristaux d'olivine se sont apparemment développés tardivement dans un mélange de cristaux et d'un fondu silicaté, tel que laisse croire les observations pétrologiques et les données géochimiques. Deux modèles liés à l'apparition des cristaux en forme de branches sont proposés:

1) les cristaux d'olivine se sont formés à partir du magma résiduel provenant de la dernière injection de magma dans le réservoir; ou 2) l'olivine a cristallisé à la fin de chaque événement cyclique.

Les cristaux en forme de branches sont des objets fractals, car ils sont auto-semblables à plusieurs échelles de grandeur. Leur dimension fractale est approximativement égale à 1,6. Les formes de cristaux furent reproduites de façon qualitative et quantitative sur ordinateur à l'aide d'un algorithme d'agrégation limitée par diffusion. Par l'étude des simulations, il est suggéré que la croissance des cristaux était contrôlée par une diffusion limitée de molécules vers l'interface du cristal, et que la morphologie complexe résulte de l'interaction de deux phénomènes: 1) l'agrégation aléatoire de molécules sur l'interface du cristal; et 2) l'arrangement systématique de molécules sur l'interface correspondant à la structure cristalline interne du minéral.

D'autres facteurs pouvant avoir contribué au développement des cristaux d'olivine en forme de branches incluent: 1) la concentration élevée de constituants d'olivine dans le magma résiduel; 2) le taux de nucléation réduit d'olivine; 3) le taux de croissance élevé des cristaux d'olivine; et 4) la nature visqueuse du magma résiduel.

ACKNOWLEDGEMENTS

I wish to thank first my supervisor, Dr. Anthony Fowler, for his guidance, patience, and continual support throughout the duration of this project. His positive attitude and the confidence he showed in my capabilities were for me an invaluable source of motivation. Special thanks are extended to Dan Roach, who created the computer programs used for the DLA simulations. The realization of that part of the thesis would not have been possible without his help.

I am also grateful to the following technicians, scientists, friends, and relatives for their help and encouragement: Karine Beaudette, Georges Beaudoin, Hélène De Gouffe, Sylvie Downing, Hugues Dupuy, Jonathan Findlay, Ron Hartree, Julie Hayes, Edward Hearn, Murray Jones, Ralph Kretz, Ron Labelle, André Lalonde, François Lalonde, Aline Lemieux, David Lentz, John Loop, Moira McKinnon, Suzanne Meunier, George Mrazek, Alain Plouffe, Peter Roader, Jean-François Tardif, Pierre Thériault, and Donald Watanabe.

This project was financially supported by the following organizations: Fonds pour la Formation de Chercheurs et l'Aide à la Recherche (Postgraduate Scholarship); Natural Sciences and Engineering Research Council of Canada (Grant to Dr. A.D. Fowler); Ontario Graduate Scholarship Program (Postgraduate Scholarship); University of Ottawa (Postgraduate Scholarship).

TABLE OF CONTENTS

CHAPTER 4

GEOCHEMISTRY OF THE CENTRE HILL COMPLEX

CHAPTER 5

PETROGENESIS OF THE CENTRE HILL COMPLEX

CHAPTER 6

ORIGIN OF BRANCHING OLIVINE CRYSTALS

LIST OF TABLES

LIST OF FIGURES

LIST OF PLATES

CHAPTER 1

INTRODUCTION

1.1 GENERAL STATEMENT

Conspicuous branching textures up to 50 cm in length have been observed near the upper margin of a gabbroic layer within the Centre Hill complex, Munro Township, Ontario. The branching forms are regarded as disequilibrium textured minerals, as they were likely grown at temperatures below thermodynamic equilibrium (i.e. liquidus temperature).

Although disequilibrium textured minerals are characteristic of volcanic rocks subjected to rapid cooling, they are also known to form in plutonic settings. Hence, their growth mechanism is not only dependent on the rate of cooling, but may also be governed by factors such as phase supersaturation, density of nuclei, diffusion rate, and volatile content (Donaldson, 1974, 1976). Dynamic crystallization experiments by Lofgren (1974) on plagioclase crystal morphology showed a systematic progression from faceted to dendritic and branching habits with increasing undercooling ($T_{liquidus}-T_{crystallization}$). He related the morphology differences to changes in the ratio of the crystal growth rate relative to the atomic diffusion rate in the liquid. Donaldson (1976) experimentally demonstrated that complex olivine crystal types could form at low cooling rates from melts saturated in

olivine or volatiles.

The main objective of this study is to explain the occurrence of the megascopic branching forms found in the gabbro. Research was aimed at determining the primary composition of the branching phase from the actual metamorphic assemblage. It is shown that their growth can be simulated using a variation of the diffusion limited aggregation (DLA) algorithm, and that the crystal morphologies are fractal. In addition, a model of crystallization of the entire sill based on petrological observations and geochemical data is proposed.

Although most minerals described in this thesis have been chemically altered by metamorphic processes, rock units are considered throughout as igneous rocks in light of the excellent preservation of primary textures.

1.2 LOCATION AND ACCESS

The Centre Hill complex is located in the north-central part of Munro Township (48°36'N latitude, 80°12'W longitude), approximately 80 km east of Timmins and 50 km north of Kirkland Lake in the Cochrane district of northern Ontario. The area is situated in the central portion of the Abitibi Subprovince (Figure 1).

Access is possible by highway 101 which extends west to Timmins and east to LaSarre. The road closely parallels the southern boundary of Munro Township, and the Centre Hill complex can be reached by a well maintained gravel road leading to the abandoned Potter mine. Outcrop exposures of the complex, directly

FIGURE 1. Simplified geological map of the Abitibi Subprovince in the vicinity of Kirkland Lake. Centre Hill is shown in the northwestern corner (modified after Fowler and Jensen, 1989).

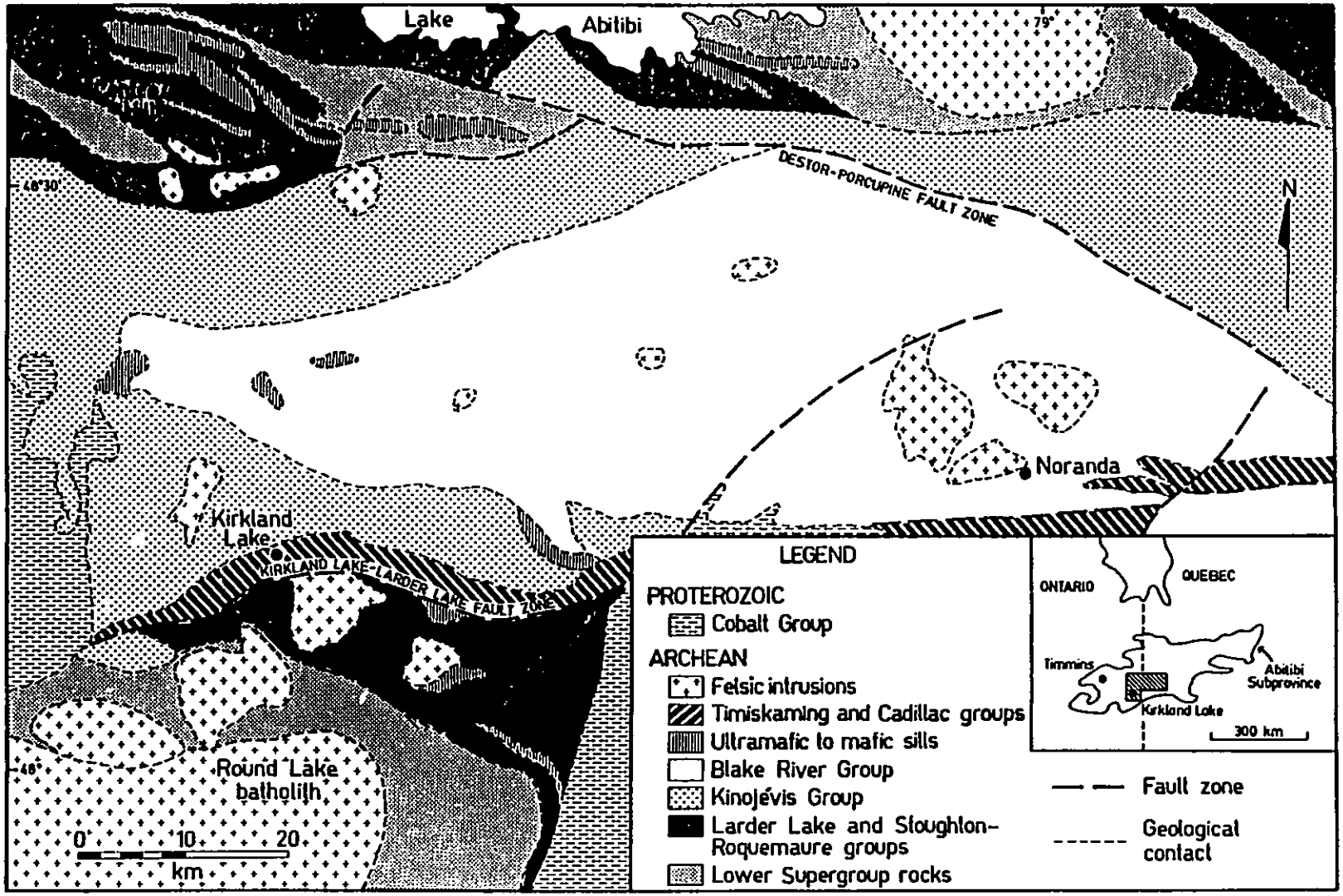
Lake
Abitibi
79°
48°30
DESTOR-PORCUPINE FAULT ZONE
N
Noranda
Kirkland Lake
KIRKLAND LAKE-LARDER LAKE FAULT ZONE
48°
Round Lake batholith
0
10
20
km
LEGEND
PROTEROZOIC
Cobalt Group
ARCHEAN
Felsic intrusions
Timiskaming and Cadillac groups
Ultramafic to mafic sills
Blake River Group
Kinojévis Group
Larder Lake and Stoughton-Roquemaure groups
Lower Supergroup rocks
ONTARIO
QUEBEC
Timmins
Abitibi Subprovince
Kirkland Lake
300 km
Fault zone
Geological contact

south of the mine, are easily accessible.

1.3 PREVIOUS WORK

Geological mapping of Munro Township and vicinity was first carried out by Satterly (1952) on a scale of 1 inch to 1000 feet (1:12 000). The map was part of a document entitled "The Geology of Munro Township", which appeared in the Sixtieth Annual Report of the Ontario Department of Mines. His work was followed by that of MacRae (1963), who completed a detailed study on the petrology of the Centre Hill complex as an M.Sc. thesis project at McMaster University. Field relations were examined, and a section across the complex was systematically mapped and sampled. MacRae (1965, 1969) later documented the petrology and geochemistry of a related belt of differentiated ultramafic-gabbroic sills located east of Matheson, emphasizing the Munro Lake sill.

Several studies conducted in Munro Township have focused on the economic potential of the area. Coad (1976) wrote an M.Sc. thesis (University of Toronto) on the geology of the Potter mine, a stratiform massive sulphide deposit overlying the northern edge of the Centre Hill complex. Research was also done on asbestos (Hendry, 1951; Freeman, 1954; and Wicks et al., 1984) and gold mineralization (Pyke, 1976; and MacRae and Crocket, 1977).

In recent years, considerable activity has centered on the renowned Munro komatiites, most notably the spinifex-textured rocks of Pyke Hill (Pyke et al., 1973; Fleet and MacRae, 1975; Arndt et al., 1977; Donaldson, 1982a; Arndt and Nesbitt, 1984;

Johnstone, 1987; and Walker et al., 1988). The layered komatiites of Pyke Hill form the base of a thick succession of peridotitic and basaltic komatiitic flows exposed approximately 200 m northeast of Centre Hill. Spectacular bladed olivine crystals over 50 cm in length are characteristic of this type locality.

Although the branching textures that are the subject of this thesis have not been documented in detail (Johnstone, 1987; and Fowler et al., 1989a), similar dendritic and branching crystals have been reported from mafic plutonic rocks elsewhere. For instance, the branching olivine crystals of the comb-layered harrisitic rocks of the Rhum pluton have been the subject of much attention over the years (Wager and Brown, 1951; Donaldson, 1974, 1977, 1982a; and Emeleus, 1987). Other occurrences include the curved, branching crystals of the Willow Lake layered intrusion (Taubeneck and Poldervaart, 1960), the "perpendicular-feldspar" and pyroxene crescumulates in the Skaergaard intrusion (McBirney and Noyes, 1979), the "christmas-tree" olivine crystals of the Rognsund gabbro (Robins, 1973), and the columnar-dendritic feldspars in the Lardalite intrusion (Petersen, 1985).

CHAPTER 2

GENERAL GEOLOGY

2.1 REGIONAL SETTING

Munro Township is located near the centre of the Archean Abitibi Subprovince, within the Superior Province of the Canadian Precambrian Shield. The Abitibi Subprovince is a northeast-trending greenstone belt approximately 800 km long by 240 km wide. It is truncated to the east by the Grenville Province, to the west by the Kapuskasing structural zone, and to the north by the Quetico Subprovince. It is unconformably overlain by the Proterozoic Cobalt Group to the south (Jensen, 1985). The belt is predominantly composed of volcanic and sedimentary rocks locally intruded by large granitic plutons.

In the Timmins-Kirkland Lake area, the volcanic stratigraphy is preserved in a large east-trending synclinorium bounded by Lake Abitibi to the north, and the Round Lake batholith to the south (Figure 1). The northern and southern limbs of the synclinorium are transected by two large east-striking fault systems: the Destor-Porcupine fault zone, and the Kirkland Lake-Larder Lake fault zone respectively. The volcanic rocks have been regionally metamorphosed to the prehnite-pumpellyite facies (Jolly, 1978). Metamorphism locally increases to the greenschist and amphibolite grades surrounding sub-volcanic intrusions and

late-stage granitic plutons (Johnstone, 1987).

The volcanic succession has been interpreted to consist of three overlapping supergroups, each of which are composed of a komatiitic group overlain by tholeiitic, calc-alkalic, and in places alkalic groups (Jensen, 1985). Each supergroup was formed during a cycle of volcanism associated with episodic events of sedimentation and plutonism (Jensen and Langford, 1983). Rocks of the first two volcanic cycles, the Lower Supergroups, are restricted to the margins of the synclinorium and have been intruded in places by large granitic plutons. The Upper Supergroup, which occupies most of the synclinorium, is composed of four distinct groups. The lower komatiitic unit, represented by the Stoughton-Roquemaure Group on the north limb of the synclinorium and the Larder Lake Group on the south limb, is dominantly composed of flows of komatiitic and tholeiitic basalt. The komatiitic sequence is overlain by magnesium-rich and iron-rich tholeiitic basalt flows of the Kinojévis Group. The rocks display a strong iron-enrichment trend towards the top of the succession (Fowler and Jensen, 1989). The calc-alkalic volcanic succession of the Blake River Group discordantly overlies the Kinojévis Group in the core of the synclinorium. The sequence comprises mainly of basalt and andesite, with lesser amounts of dacite and rhyolite. Alkalic to subalkalic trachytic rocks of the Timiskaming Group represent the final stages of volcanism which formed the Upper Supergroup. They are found on the south limb of the synclinorium unconformably overlying both the Blake River and

Kinojévis groups (Jensen and Langford, 1983).

2.2 LOCAL GEOLOGY

The Stoughton-Roquemaure Group is located north of the Destor-Porcupine fault zone near Lake Abitibi (Figure 1), where it disconformably overlies felsic volcanic rocks of the Hunter Mine Group, the uppermost unit of the Lower Supergroup II. The volcanic succession of the Stoughton-Roquemaure Group is more than 15 km thick and consists mainly of komatiitic and tholeiitic lava flows conformably intruded by sill-like bodies of ultramafic-gabbroic rocks (Figure 2). Peridotitic and basaltic komatiite flows are most abundant in the lower part of the group, with magnesium-rich tholeiitic basalt increasing in abundance towards the top. A zone of thick komatiitic lava flows that extends into Munro Township has been documented in detail by Arndt et al. (1977).

The lower 1500 m of the group is dominated by coarse-grained bodies of peridotite and gabbro interlayered with lesser amounts of massive and pillowed flows. According to Eakins (1972), many of these gabbroic layers could have been thick, massive flows. Several differentiated ultramafic-gabbroic sills are found higher up in the sequence. They are part of a long belt of mafic to ultramafic intrusions extending from north of Timmins past the south end of Lake Abitibi.

FIGURE 2. Simplified geological map showing the distribution of ultramafic-gabbroic sills within the Stoughton-Roquemaure Group. The Centre Hill complex is outlined in black (modified after MacRae, 1969).

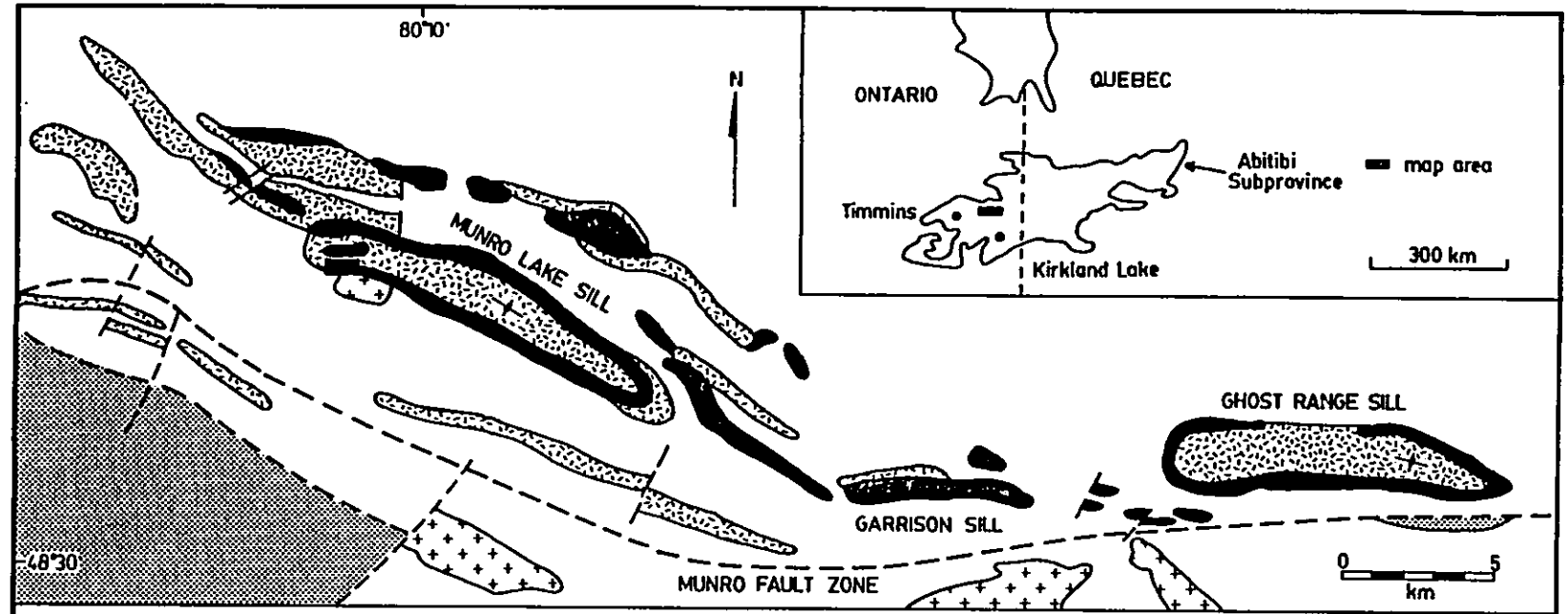

ARCHEAN

- Intermediate to felsic intrusive rocks

STOUGHTON-ROQUEMAURE GROUP

- Gabbroic rocks
- Ultramafic intrusive rocks
- Komatiitic to tholeiitic volcanic rocks

PORCUPINE GROUP

- Sedimentary rocks

- anticlinal axis
- fault
- outline of Centre Hill Complex (Figure 3).

2.2.1 Major differentiated sills

Several of the differentiated ultramafic-gabbroic sills that outcrop in the vicinity of Munro Township have been documented by MacRae (1969) and Johnstone (1987). These shallow-level sills are composed of layers of peridotite, clinopyroxenite, and gabbro, and range from 60 to about 1000 m in thickness (MacRae, 1969). The Munro Lake sill and the Painkiller Lake complex are characterized by alternating layers of peridotite and clinopyroxenite overlain by an upper gabbro layer. The cyclic repetition of ultramafic layers is explained by periodic introduction of new magma into the chamber (MacRae, 1969). Simple differentiated sills found in the area include the Ghost Range, Garrison, and Barton Creek sills.

2.2.2 Munro Lake sill

The layered Munro Lake sill is exposed in three distinct areas: (1) in north-central Munro Township and the southern border of Warden Township, where it is referred to as the Munro-Warden complex; (2) at McCool Hill in south-central McCool Township, where it is named the McCool Hill complex; (3) and at Centre Hill near the middle of Munro Township, where it is known as the Centre Hill complex. Based on aeromagnetic maps and the similarity of the layering, Satterly (1952) proposed that the three exposures were part of the same intrusive body. The sill is folded into a northwest-plunging syncline (McCool Hill syncline) having sub-vertical limbs. It is complexly disrupted by

longitudinal and cross faults. Minor folds are observed on both limbs (MacRae, 1965). The sill has a strike length of approximately 12 km between southern Warden Township and its easternmost point at McCool Hill. Its thickness varies from 400 to 600 m (Johnstone, 1987).

The upper half of the sill consists of about 250 m of gabbro underlain by a cumulate portion characterized by alternating layers of clinopyroxenite and peridotite. According to Johnstone (1987), the upper 200 m of the sill at the Munro-Warden complex is composed of a leucogabbro layer which is not observed in the other two exposed areas. He suggests that it may represent a different intrusive body since the layer is separated from the sill by up to 20 m of pyritiferous chert.

2.3 CENTRE HILL COMPLEX

The Centre Hill complex is the only outcrop area that exposes a complete stratigraphic section of the Munro Lake sill. The hill is fairly prominent, rising about 75 m above the local topography. It is elliptical in shape, being approximately 1200 m long (east-west) and 500 m wide (north-south). Rock exposure is excellent as it covers about 70% of the hill.

At Centre Hill, the sill is east-west trending and subvertical, the layers dipping between 70° northward and vertical. It has been sharply drag-folded southward against the Centre Hill fault along the southern edge of the hill (Figure 3 in back pocket). This folding has lead to the thickening and thinning of

the lower ultramafic layers. Several northwest-trending cross faults have been recognized at the crest of the drag-fold. These have very little associated displacement (Satterly, 1952).

2.3.1 Host rocks

The Munro Lake sill is in contact with mafic and ultramafic metavolcanic rocks in the Centre Hill area. The northern margin of the complex is in contact with a basaltic breccia composed of medium size, subrounded fragments of fine-grained, optically unresolvable secondary minerals. The matrix consists of quartz and minor calcite. On the west end of the complex, the breccia is in contact with a massive, serpentinized peridotitic komatiite. The southern border of the sill lies in fault contact with a basaltic komatiite flow displaying a well developed spinifex texture. A small intrusion of quartz diorite underlies the southeastern part of the complex across the Centre Hill fault (Satterly, 1952). At the east end of Centre Hill, the sill has been transected by two north-south Matachewan diabase dykes containing characteristic epidotized plagioclase phenocrysts (Johnstone, 1987).

2.3.2 Stratigraphy

An entire stratigraphic section of the Munro Lake sill at Centre Hill has been measured by Satterly (1952) and later modified by MacRae (1963, 1965). The section was measured directly east of the crest of the fold, where the sill is

approximately 455 m thick. The stratigraphy of the complex as shown in Figure 4 was simplified after MacRae (1965) and shows dominant rock textures and sampling sites. The measured width of each layer was assumed to equal its true thickness as the sill is more or less vertical in the area.

The Centre Hill complex is composed of 15 separate layers that have been grouped into seven distinct units: the bottom five units are cyclic and consist of successive layers of peridotite and clinopyroxenite; the sixth is composed of peridotite, clinopyroxenite, and gabbro; and the uppermost unit is made up of a thin melagabbro layer grading into the thick upper gabbro portion of the sill. The thickness of the peridotite-clinopyroxenite cyclic units is highly variable, ranging from 10 to 49 m. The sixth peridotite-clinopyroxenite-gabbro unit is 66 m thick, whereas the upper melagabbro-gabbro unit is 225 m in thickness.

Apart from the contact between the layer of melagabbro and the upper gabbro layer, which is gradational over several centimetres (MacRae, 1963), lithological contacts are considered sharp. Chilled margins were not observed along both intrusive contacts.

2.3.2.1 Peridotite layers

A total of six peridotite layers have been recognized in the Centre Hill complex. The rocks have black fresh surfaces and weather to a medium greyish-brown colour. The layer thickness varies from one metre to over 21 metres, becoming systematically

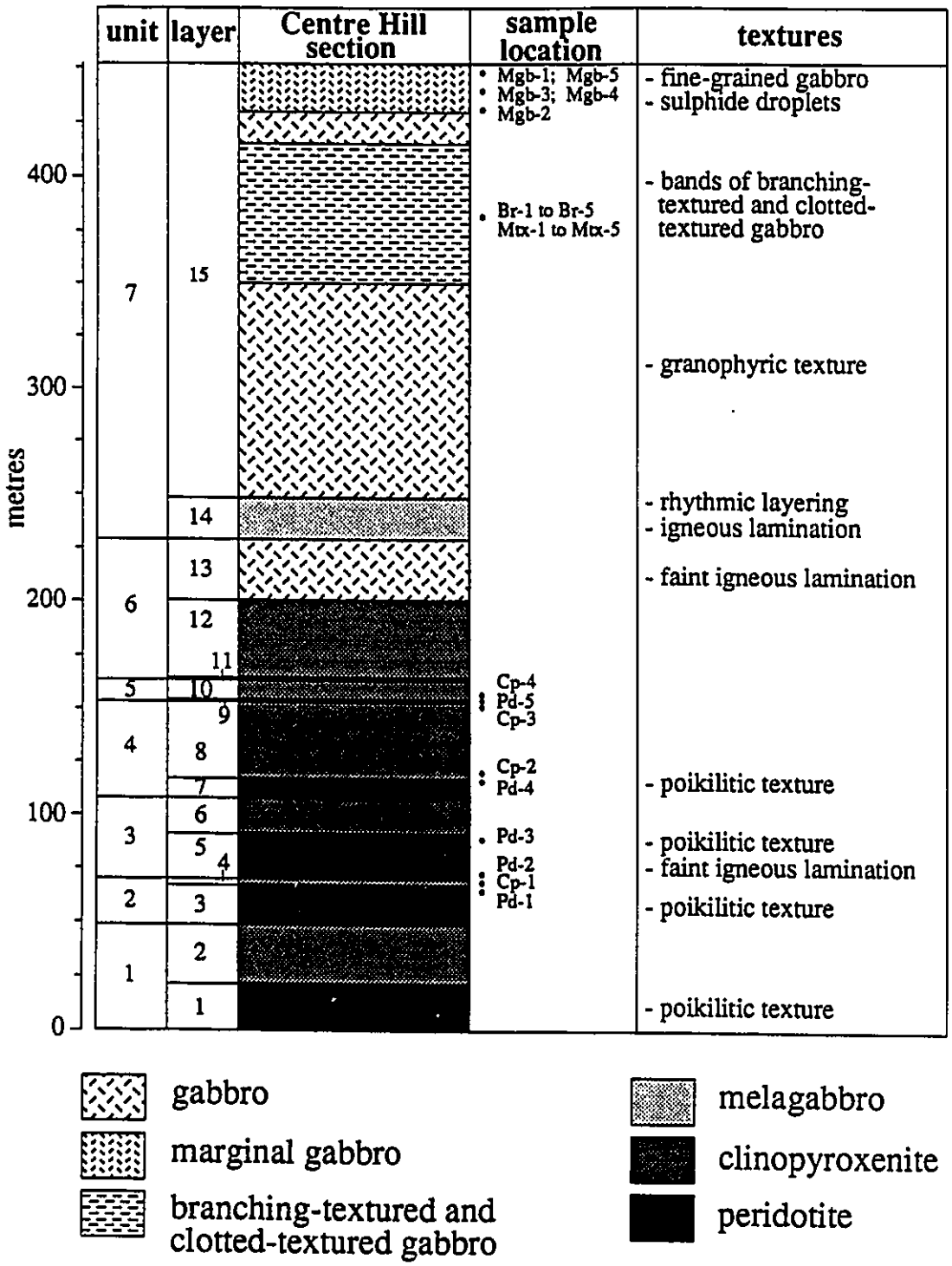

FIGURE 4. Stratigraphic section of the Centre Hill complex showing dominant rock textures and sampling sites (modified after MacRae, 1965).

thinner towards the top of the sill.

The peridotites are medium- to coarse-grained rocks composed of poikilitic crystals of clinopyroxene reaching 2 cm in diameter which stand out in high relief (Plate 1). The poikilitic crystals are commonly stretched out parallel to band contacts, defining a faint layering.

2.3.2.2 Clinopyroxenite layers

The six clinopyroxenite layers observed at Centre Hill range from 3 to 36 m in thickness, each layer representing the upper portion of an ultramafic cycle. The rock is medium greyish-green and weathers to a light brownish-grey colour. Unlike the peridotite layers, no definite trend in band width is present up-section. However, the two thickest layers are found near the gabbroic zone associated with fairly thin peridotite layers. Contacts between the top of peridotite layers and overlying clinopyroxenite are considered sharp (Plate 2).

The clinopyroxenites are typically massive, fine- to medium-grained rocks that become progressively more feldspathic towards the top of the sequence.

2.3.2.3 Gabbro layers

Gabbroic rocks make up the upper 253 m of the Centre Hill complex. They are subdivided into three distinct layers: (1) a bottom layer of gabbro which represents the upper portion of the sixth unit, (2) a middle melagabbro layer, and (3) a thick layer

PLATE 1: Outcrop surface of peridotite (layer #3) showing well developed poikilitic texture. Clinopyroxene crystals (shown by white arrows) are dark brown in colour and stand out in high relief.

PLATE 2: Outcrop surface showing the sharp contact between peridotite layer #6 (Pd) and clinopyroxenite layer #7 (Cp). Top of sill is indicated by the large black arrow. Hammer is 25 cm long.

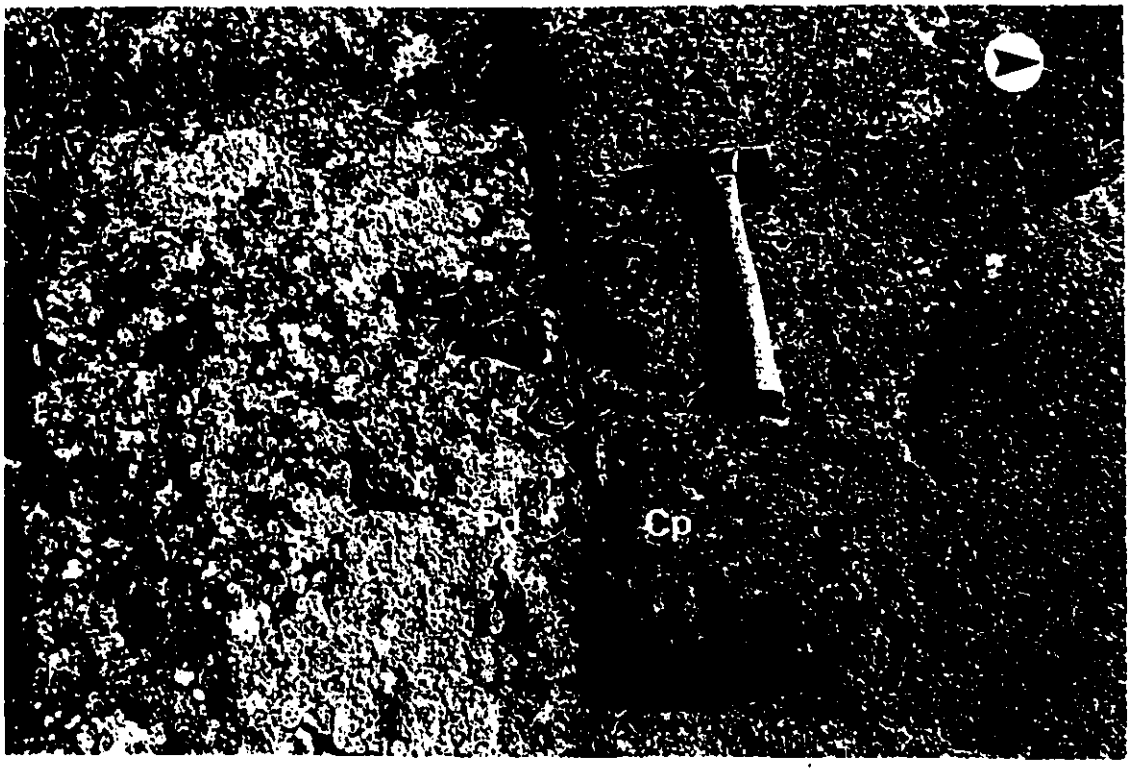
Pd
Cp

of gabbro. The last two layers make up the seventh and last differentiated unit found at Centre Hill.

The lowermost layer of gabbro is 28 m thick and marks the first occurrence of cumulus plagioclase. The rock is easily recognized by its light-grey weathering surface and typical gabbroic texture. Igneous laminations defined by parallel arrangement of plagioclase laths have been observed upward in the layer (MacRae, 1963).

The middle layer of melagabbro measures 20 m in thickness and shows prominent igneous laminations characterized by discontinuous, millimetre-sized bands of elongated plagioclase and clinopyroxene crystals. The lower 50 cm of the layer is marked by alternating bands (each approximately 3 cm in width) of gabbro and melagabbro. The rock is dark-green and weathers to a medium greyish-green colour.

The upper portion of the Centre Hill complex consists of a 205 m thick layer of gabbro, constituting approximately 45% of the entire thickness of the sill. It will be described separately hereafter since most of the work focused on the intricate textural features observed within this layer.

2.4 UPPER LAYER OF GABBRO

The uppermost layer of gabbro is very well exposed throughout the northern portion of Centre Hill. The rock is generally medium- to coarse-grained and medium grey on fresh surfaces. It weathers a light to medium brownish-grey colour. Thin epidote

veinlets as well as quartz pods up to 20 cm in width were observed locally. To the north, along the marginal border of the sill, the gabbro is very fine-grained and contains a relatively high proportion of sulphide-rich globules up to 5 mm in diameter. These possibly formed by sulphide-silicate liquid immiscibility.

The gabbro is quite homogeneous throughout, with the exception of a small area along the northwestern margin of the complex where systematic variations in texture were observed, giving the rock a definite banded appearance.

The area where banding was observed is approximately 200 m long by 70 m wide and parallels the border of the sill along the crest of the fold (Figure 3). The banded zone extends from about 30 m below the upper contact to near the middle of the gabbro layer. Unfortunately, banding in the gabbro was only evident where surface weathering was minimal, thus making it very difficult to follow individual bands along strike. Meticulous field examination nonetheless established that banding is restricted to the upper portion of the layer.

The banding is made evident by distinct changes in rock texture that are either gradational or sharp. The bands invariably parallel the cooling contact and are of 3 types. Those containing: 1) branching textures; 2) clotted textures; and 3) a combination of both textures. Band width is highly variable, although clotted-textured bands are generally around one metre in thickness and separated by up to 15 m of branching-textured gabbro of the first or third type.

2.4.1 Branching-textured gabbro (BTG)

The bands of BTG are typically composed of oriented branching structures set in a fairly homogeneous matrix of gabbroic composition. Although the exact number of bands of this type could not be determined due to intense weathering of the outcrop surface, it is estimated that 5 to 8 individual bands ranging between 5 and 15 m in thickness are present.

The amount of branching material within the bands is significant, constituting on average approximately 20 vol.% of the rock and reaching as much as 30 vol.% in areas of maximum density (Plates 3 to 6). The schematic diagrams shown in figures 5 and 6 illustrate in detail the distribution of branching textures from part of the area covered by plates 3 and 6.

Throughout this study, the bands of BTG are subdivided into two distinct entities, referred to as "branches" and "matrix". They will be treated separately in light of their contrasting petrographic attributes, geochemical signatures, and time of crystallization.

2.4.1.1 Branches

A very conspicuous feature of the branches is their characteristic brick-red colouration on the weathered surface, which contrasts with the dull brownish-grey colour of the matrix. Oxidation of Fe-rich minerals within the branching parts accounts for this reddish staining. However, the fresh surface is dark green to black (Plate 7), suggesting a high proportion of mafic

PLATE 3: Outcrop surface of BTG (35 meters below upper margin of sill) showing ramified segments of branching textures set in a medium-grained gabbroic matrix. Well developed branching form (shown by white arrows) extend away from the upper margin (see Plate 11). Top of sill is indicated by the large black arrow. Hammer is 25 cm long.

PLATE 4: Outcrop surface of BTG (40 meters below upper margin of sill) displaying irregular segments of branching textures. Note large branching form in the lower right corner (shown by white arrows) extending away from the upper contact. Top of sill is indicated by the large black arrow. Hammer is 25 cm long.

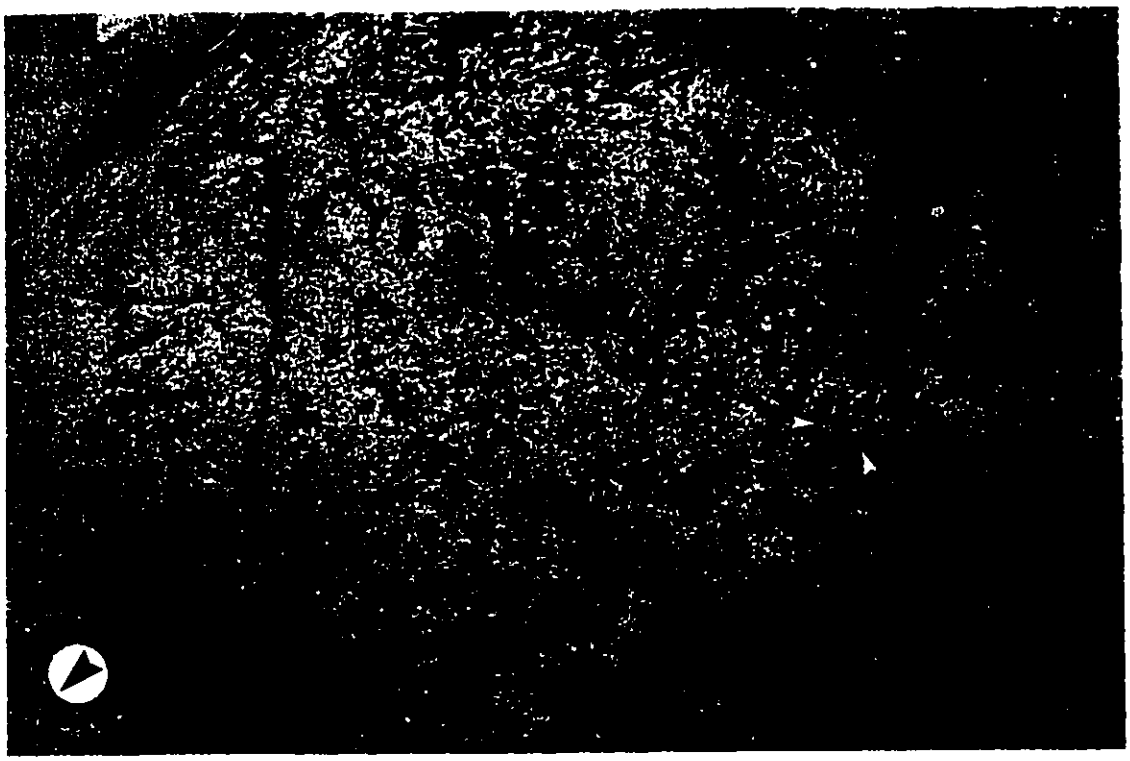

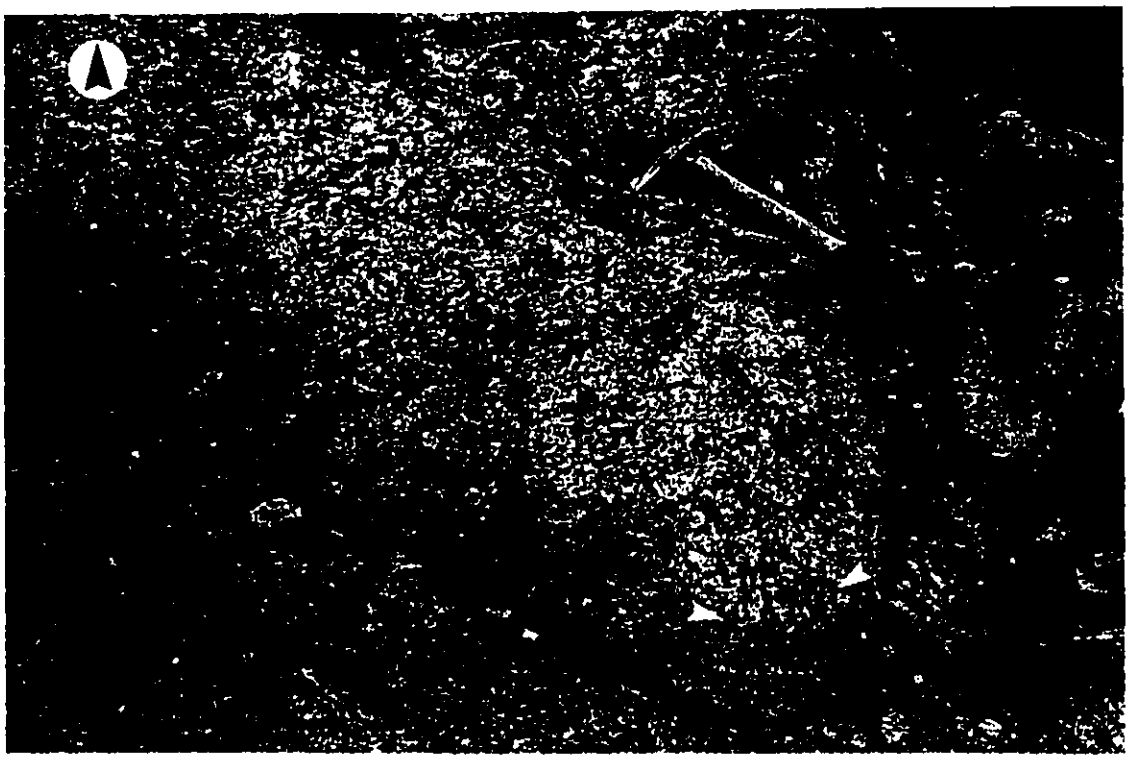

PLATE 5: Outcrop surface of BTG (50 meters below upper margin of sill) showing well developed branching structures (white arrows) grown perpendicular to the upper margin. Top of sill is indicated by the large black arrow. Pen is 14 cm long.

PLATE 6: Outcrop surface of BTG (55 meters below upper margin of sill) displaying irregular ramified segments of branching textures. Small branching forms in lower right corner (black arrows) extend away from the upper contact. Top of sill is indicated by the large black arrow. Scale card is in centimetres.

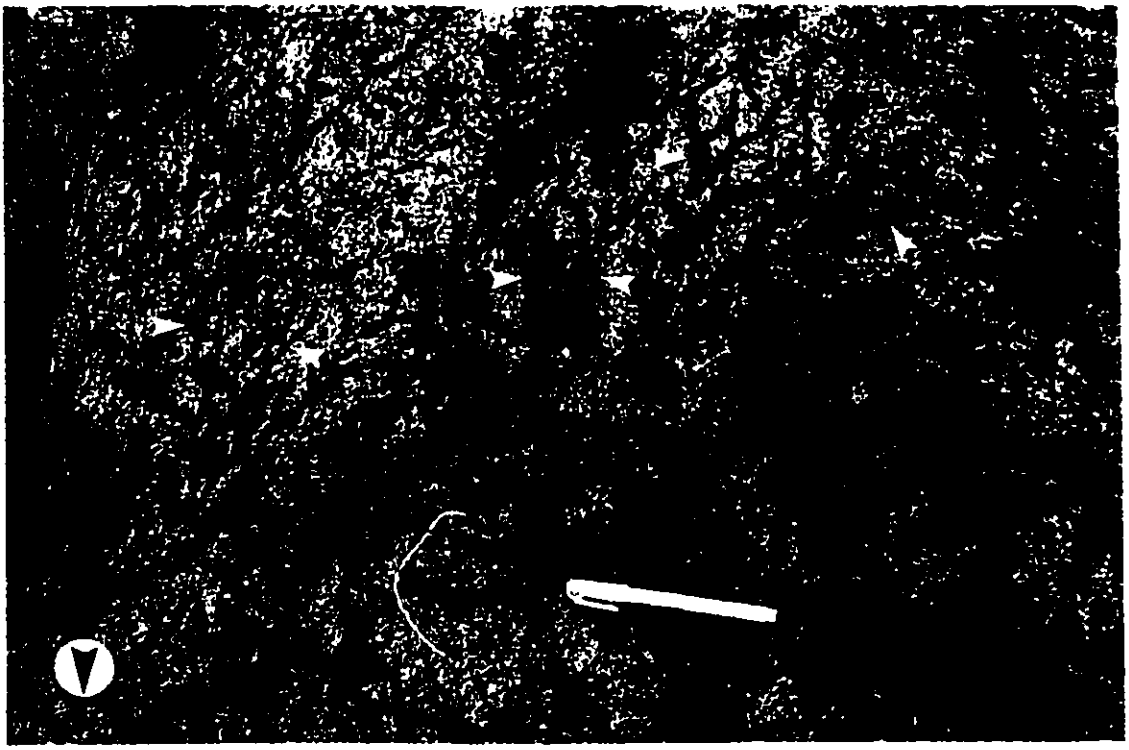

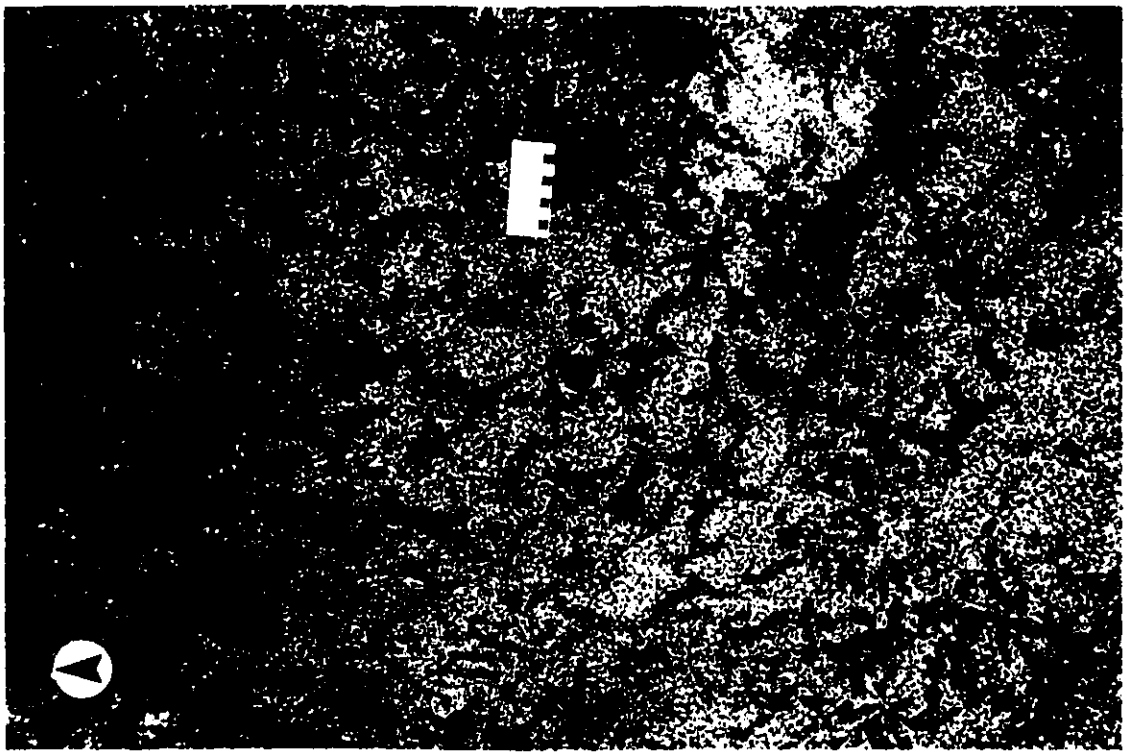

FIGURE 5. Schematic diagram illustrating the distribution of branching textures from the area shown in Plate 3. Top of sill represented by arrow in upper left corner.

FIGURE 6. Schematic diagram illustrating the distribution of branching textures from part of the area shown in Plate 6. Top of sill is represented by arrow.

minerals.

As can be seen from Plate 8, the branches are in part composed of an assemblage of plagioclase, clinopyroxene, and Fe-Ti oxide identical to the mineralogy of the matrix. The branching textures are thus interpreted as large poikilitic crystals that have enclosed smaller crystals of the matrix during their growth.

The distribution of poikilitic crystals on the surface of the outcrop is highly variable. Although well developed branching forms are commonly observed, the poikilitic crystals generally occur as irregular ramified segments of various size and shape (plates 3 to 6). In three dimensions, the poikilitic crystals are interpreted to be branching, cone-shaped structures similar in appearance to deciduous trees. Thus, the unconnected amoeboid shapes found on the outcrop surface constitute a two-dimensional section through the BTG. Some may also represent broken off segments of crystals left suspended in the partly solidified magma.

The branching crystals have grown to remarkable proportions, their size ranging between 15 and 52 cm (Plates 9 to 12). They are generally composed of several tens of side branches approximately 1 cm in width. The density of individual structures appears to be quite variable, whereas the angle of opening remains fairly constant.

A total of 45 individual branching crystals having well defined morphologies were identified, and their growth directions measured. Figure 7 illustrates the strong tendency for the

PLATE 7: Polished slab of a relatively unaltered surface of BTG. Dark green to black branching structure is in sharp contrast with the grey matrix. Thin epidote veinlet is shown by the white arrows. Top of sill is indicated by the large black arrow. Ruler is in centimetres.

PLATE 8: Weakly altered outcrop surface of BTG showing small crystals of clinopyroxene (Cpx), plagioclase (Pl) and ilmenite (Ilm) enclosed within larger poikilitic crystal (large white arrows). Scale card is in centimetres.

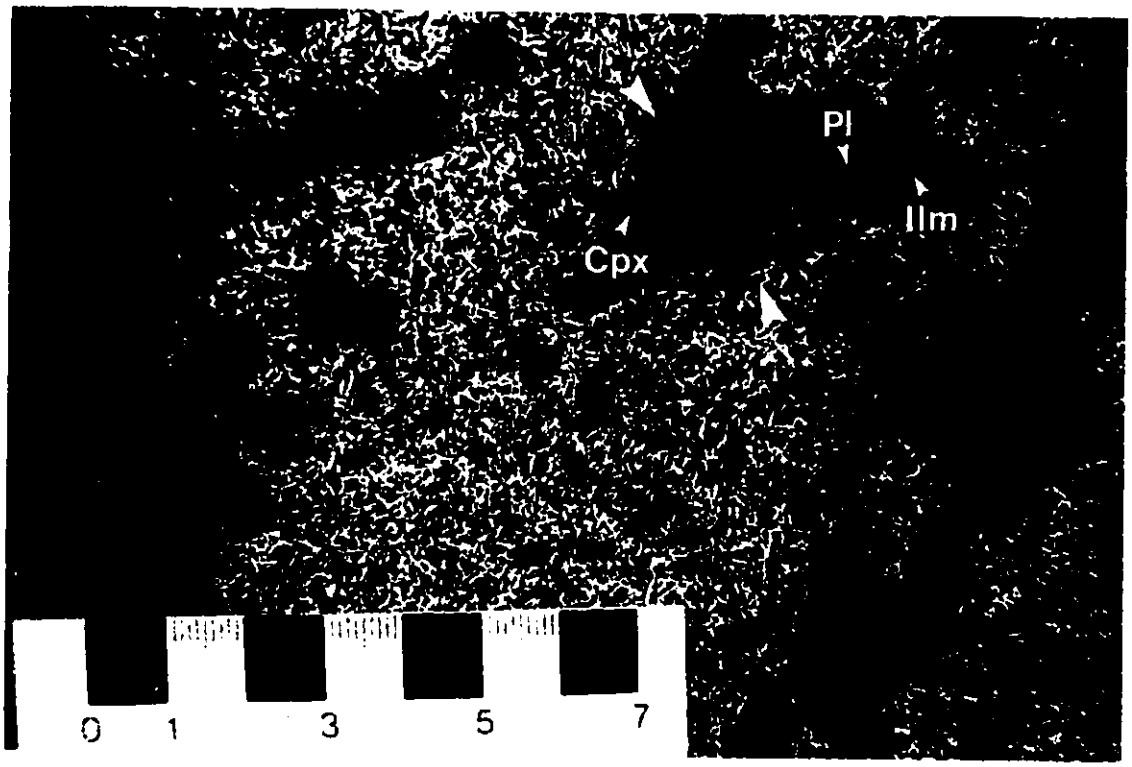
Pl
Ilm
Cpx
0
1
3
5
7

PLATE 9: Outcrop surface of BTG (65 meters below upper margin of sill) showing a spectacular branching crystal reaching 52 cm in height and extending away from the upper margin. Note the strong resemblance to a deciduous tree. Top of sill is indicated by the large black arrow. Ruler is 30 cm long.

PLATE 10: Outcrop surface of BTG (50 meters below upper margin of sill) displaying poikilitic crystals branching at right angles to the upper contact. Note the low degree of compactness of the structure relative to the branching form of the preceding photograph. Top of sill is indicated by the large black arrow.

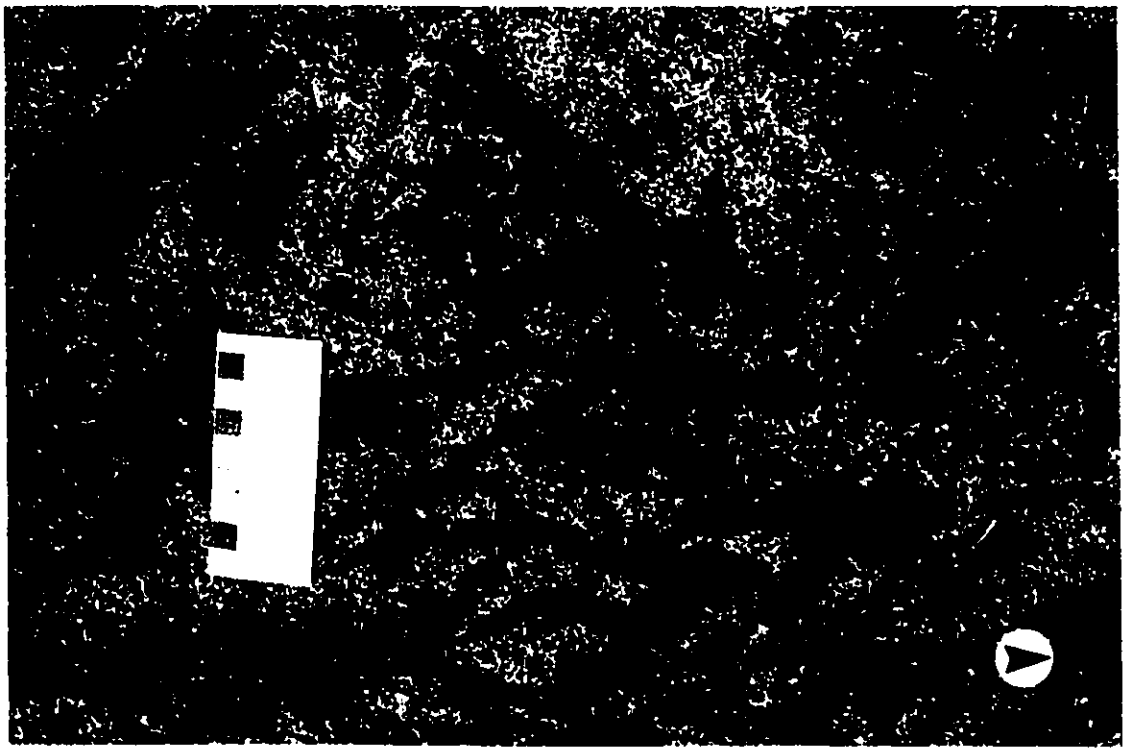

PLATE 11: Outcrop surface of BTG (35 meters below upper margin of sill) showing a well defined branching crystal extending perpendicular to the upper margin. The surrounding matrix is dominated by crystals of plagioclase (Pl), clinopyroxene (Cpx) and ilmenite (Ilm). Top of sill is indicated by the large black arrow. Loony for scale.

PLATE 12: Outcrop surface of BTG (60 meters below upper margin of sill) displaying part of a branching poikilitic crystal grown at right angles to the upper contact. Top of sill is indicated by the large black arrow.

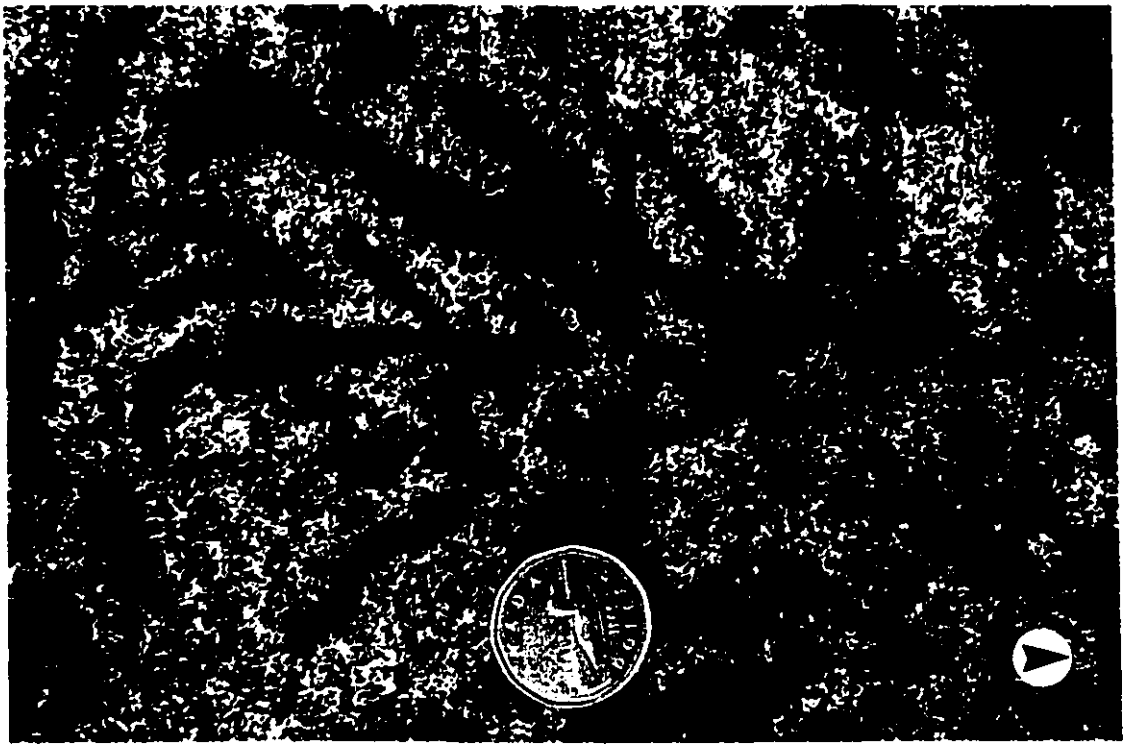


CENTIMETRES

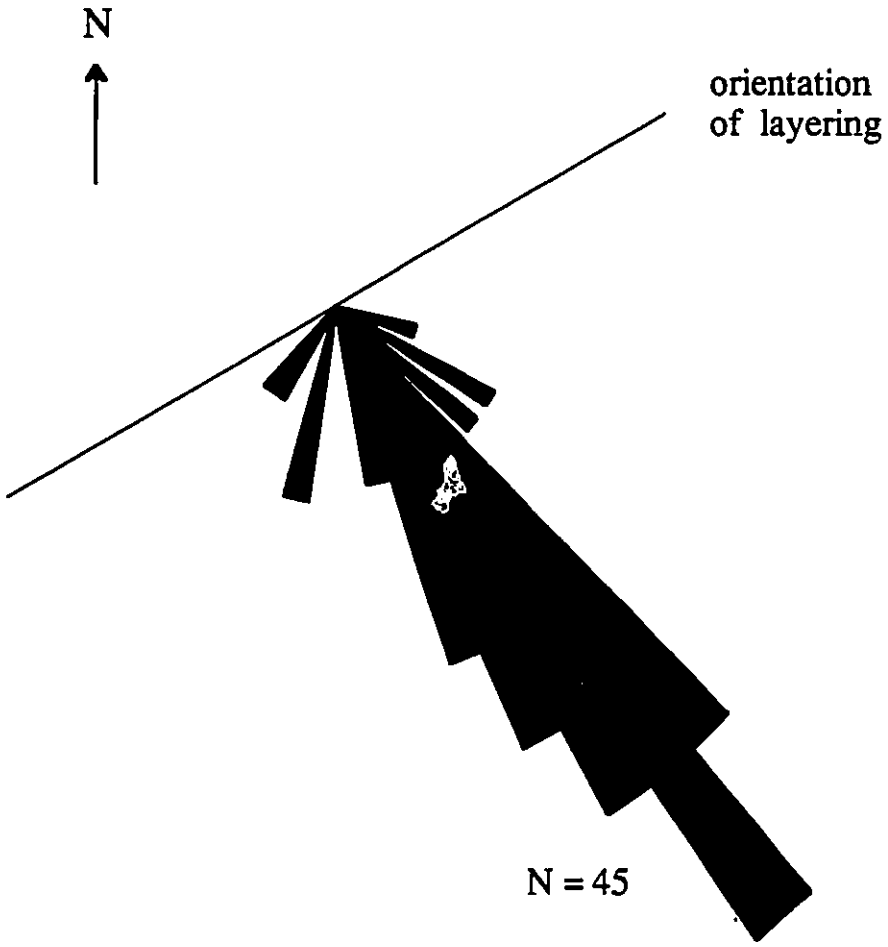

FIGURE 7. Rose diagram showing the growth direction of branching crystals relative to the layering. The orientation of layering is based on 7 measurements.

crystals to branch towards the middle of the sill, roughly at right angles to the banding. Hence it can be said that the rock exhibits a crescumulate texture. This direction of growth undoubtedly implies that the top of the upper gabbro layer crystallized from the roof downwards. Although several crystals have nucleated along the upper contact of branching-textured bands with overlying clotted-textured bands, they are generally found randomly dispersed throughout the former.

2.4.1.2 Matrix

The matrix is a relatively homogeneous, medium- to coarse-grained gabbro comparable in appearance to what is found throughout the upper layer of gabbro. It is generally composed of approximately 55 to 60 vol.% of lath-shaped plagioclase, 35 to 40 vol.% of equant to tabular crystals of clinopyroxene, and less than 5 vol.% of Fe-Ti oxide having a distinct brick-red colour on the weathered surface (Plate 11).

In certain areas, acicular and dendritic plagioclase crystals up to 15 mm in length were observed (Plate 13), suggesting that the melt may have been locally more undercooled at the time of crystallization. Such disequilibrium textured morphologies have a tendency to occur near the bottom of branching-textured bands directly overlying zones where clotted textures are found. In contrast to plagioclase, the crystal size distribution and morphology of clinopyroxene and Fe-Ti oxide appear to remain fairly constant throughout the matrix.

2.4.2 Clotted-textured gabbro (CTG)

A total of 5 distinct bands of CTG, ranging from 30 to 100 cm in thickness, have been identified within the banded zone of the upper layer of gabbro. While the upper contacts of bands are usually gradational over a few tens of centimetres, the bottom contacts are knife-sharp and commonly act as nucleation surfaces for the development of branching crystals in the underlying band of incipient BTG. Apart from the fact that they lack branching textures, bands of CTG are recognized by their light grey weathering colouration which stands out with respect to the darker, reddish-brown-coloured bands of BTG (Plate 14).

The bands consist of approximately 25 to 30 vol.% of rounded clots randomly distributed in a medium- to coarse-grained plagioclase-rich matrix, giving the rock a spotted appearance (Place 15). The clots range from 10 to 30 mm in diameter and weather to a brick-red or black colour. They are composed of clustered crystals of clinopyroxene and minor Fe-Ti oxide often disposed in a radiating manner so as to resemble a rosette (Plate 16). The clots are set in a light grey matrix typically composed of 70 to 75 vol.% of plagioclase laths, 25 to 30 vol.% of equant crystals of clinopyroxene, and less than 5 vol.% of Fe-Ti oxide minerals. Acicular plagioclase crystals up to 2 cm long similar to those found in the matrix of the BTG were also observed in the rock surrounding the clots.

PLATE 13: Outcrop surface of BTG (55 meters below upper margin of sill) showing acicular crystals of plagioclase (white arrows) reaching up to 15 mm in length. Such disequilibrium crystal forms are common near the bottom of bands. Scale card is in centimetres.

PLATE 14: Outcrop surface (50 to 60 meters below upper margin of sill) of the banded zone showing alternating bands of BTG and CTG. The bands of BTG are typically wider and darker coloured than the bands of CTG. Note that the banding is more or less parallel to the upper margin of the intrusion. Top of sill is indicated by the large black arrow. Hammer is 25 cm long.

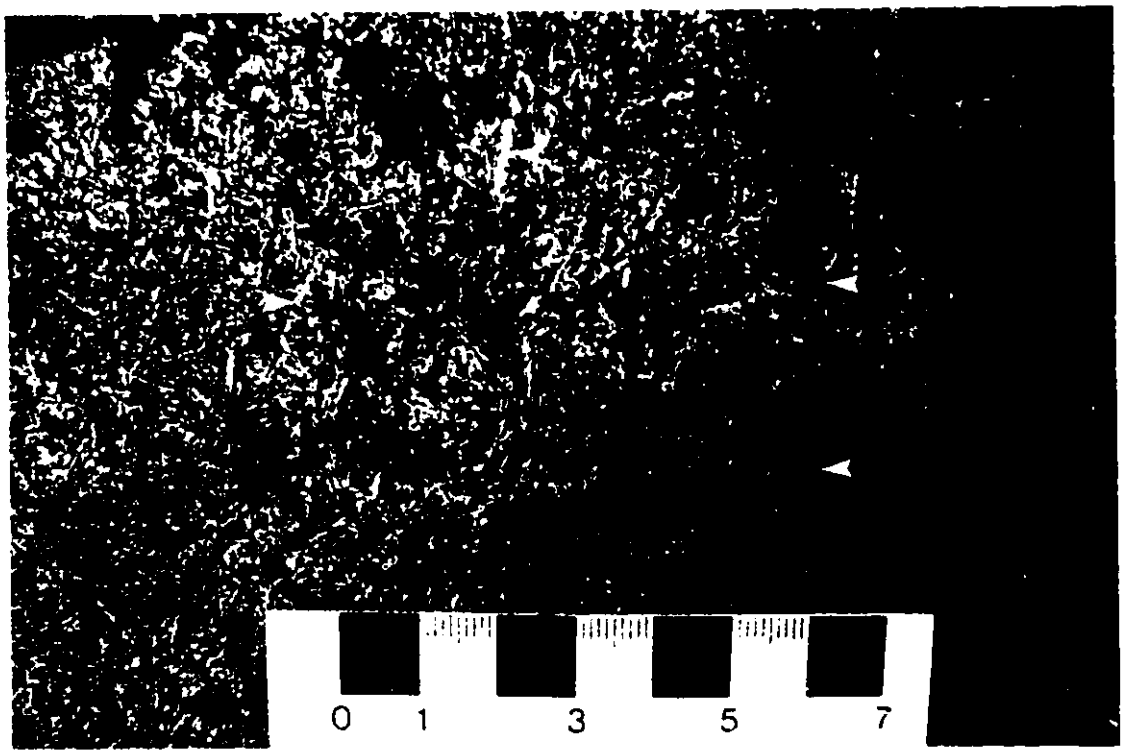
0
1
3
5
7


BTG
CTG
BLG

PLATE 15: Outcrop surface of a band of CTG (55 meters below the upper margin of sill) showing the distribution of rounded clots (white arrows) dispersed within a medium- to coarse-grained, plagioclase-rich matrix. Clots are mainly composed of clustered crystals of clinopyroxene and minor oxide, and weather to a black or brick-red colouration.

PLATE 16: Outcrop surface showing a close-up view of the preceding photograph of CTG. Crystals forming the clots are often disposed in a radiating manner so as to resemble a rosette (white arrows). Note the high proportion of plagioclase crystals within the matrix portion. Scale card is in centimetres.

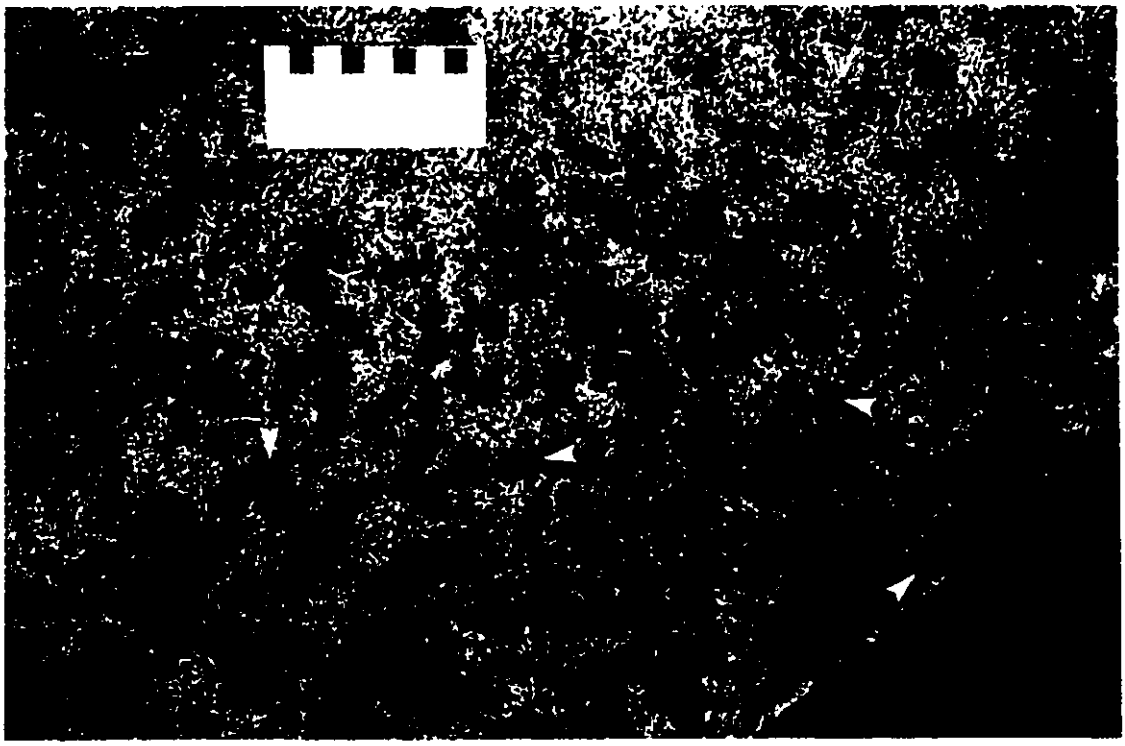

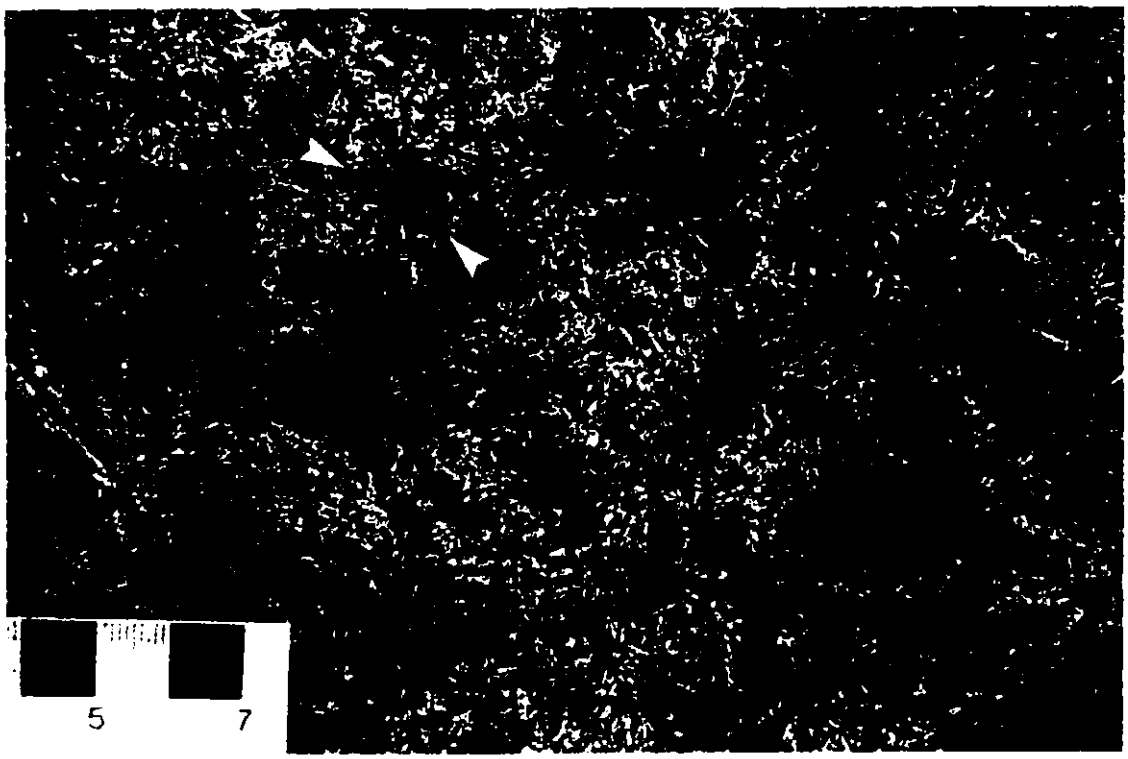
5
7

CHAPTER 3

PETROGRAPHY OF THE CENTRE HILL COMPLEX

3.1 INTRODUCTION

The mineralogical composition of the Centre Hill complex has been determined by examination of 112 thin sections from the ultramafic and gabbroic rock layers. The study by MacRae (1963) on the petrology of the complex produced a very useful database. This chapter reports on new data and interpretations.

Regional metamorphism to the greenschist facies has altered much of the primary mineralogy throughout the sill. Even though the complex truly consists of metaplutonic rocks, the prefix "meta" is not used for simplicity. Modal proportions were evaluated by combining both the primary phases and their altered products. Accurate mineral proportions were determined by point counting for the uppermost layer of gabbro. Although relatively severe in places, alteration associated with shearing did not destroy the primary textures in the rock.

Layers of peridotite and pyroxenite were not described individually, as only minor differences in their petrography were noticed. Similarly, the first layer of gabbro overlying the last pyroxenite layer was omitted due to its strong resemblance with the bottom half of the upper layer of gabbro.

Mineral names in the following photomicrograph captions have

been abbreviated according to the symbols of Table 1 proposed by Kretz (1983).

TABLE 1. Symbols for photomicrographs

actinolite	Act	leucoxene	Lcx
carbonate	Crb	magnetite	Mag
chlorite	Chl	plagioclase	Pl
clinopyroxene	Cpx	serpentine	Srp
epidote	Ep	tremolite	Tr
ilmenite	Ilm		

3.2 PERIDOTITE LAYERS

The layers of peridotite consisted originally of olivine grains and minor chromite poikilitically enclosed by larger crystals of clinopyroxene. Remarkably, a few crystals of olivine and clinopyroxene are preserved. The secondary assemblage is dominated by serpentine, tremolite and magnetite, with lesser amounts of chlorite, iddingsite and oxyhornblende. Several late-stage veinlets of fibrous chrysotile, a variety of serpentine, were observed in highly deformed areas. The modal proportions listed in Table 2 are average values determined from a total of 10 thin-sections taken from the various peridotite layers. Due to the highly variable intensity of alteration within individual layers, which is related to the degree of fracturing of the rock, a range in relative mineral content is also given in brackets.

TABLE 2. Modal proportions (vol.%) of peridotite layers.

tremolite	45	(10-70)	olivine	<1
serpentine	35	(15-60)	clinopyroxene	<1
magnetite	15	(5-20)	oxyhornblende	<1
chlorite	5	(3-10)	iddingsite	tr.
chromite	1-2			

Prior to metamorphism, cumulate olivine grains made up approximately 65 vol.% of the rock. The grains are generally subrounded and range from 1 to 2 mm in diameter, except for the two lowermost layers where they reach approximately 0.5 mm in size.

Alteration originated along grain boundaries and fractures, where olivine was replaced by a mixture of chrysotile and magnetite. Complete serpentinization of olivine yields "hour glass" chrysotile. Magnetite occurs mostly as an interstitial phase along cleavage planes of the poikilitic clinopyroxene crystals. It also crystallized within olivine grains through serpentinization, either along microfractures or as very fine disseminated particles. Abundant accumulation of magnetite amounting to over 70 vol.% of the total intercumulus material is common throughout the layers. At some localities, brick-red iddingsite was observed as a secondary product after olivine. In the most altered samples, serpentinized olivine grains are partly to totally replaced by tremolite, the grains typically having a chrysotile core rimmed by fringes of fibrous tremolite. Hence the

peridotites have undergone two distinct periods of alteration, such that tremolitization is superimposed over serpentinization.

The poikilitic crystals of altered clinopyroxene are ubiquitous in the peridotite and comprise approximately 35 vol.% of the rock. The crystals are fairly well rounded and range from 1 to 2 cm in diameter. Very little unaltered clinopyroxene remains, as the crystals are usually completely replaced by tremolite and minor chlorite. Tremolitization of serpentinized olivine and clinopyroxene apparently took place at the same time, as several clinopyroxene crystals and their poikilitically enclosed grains were found partly converted to optically continuous tremolite fibers (Plates 17 and 18).

Oxyhornblende was found partly replacing tremolitized clinopyroxene crystals within the basal peridotite layer. This observation is in contradiction with the explanation that primary hornblende may have crystallized from a water-saturated magma, and was later altered to tremolite-actinolite (MacRae, 1969). MacRae (1963) and Johnstone (1987) classified this bottom layer as a hornblende peridotite. Because it is clear that the oxyhornblende is secondary, the layer is here termed peridotite.

Iron-rich chlorite is commonly found as an interstitial phase surrounding poikilitic crystals.

PLATE 17: Photomicrograph of poikilitic texture in peridotite (under crossed nicols) showing subrounded crystals of olivine completely altered to serpentine (Srp), tremolite (Tr) and magnetite (Mag). Large poikilitic crystal of clinopyroxene (shown by large white arrows) has been replaced by tremolite. Note that tremolite is optically continuous throughout. Scale bar is 0,5 mm.

PLATE 18: Photomicrograph of poikilitic texture in peridotite (under crossed nicols) showing cumulate crystals of olivine replaced by fibrous tremolite (Tr), serpentine (Srp) and magnetite (Mag). Note that the enclosed crystals typically have a serpentine core and are fringed by tremolite. Scale bar is 0,2 mm.


Srp

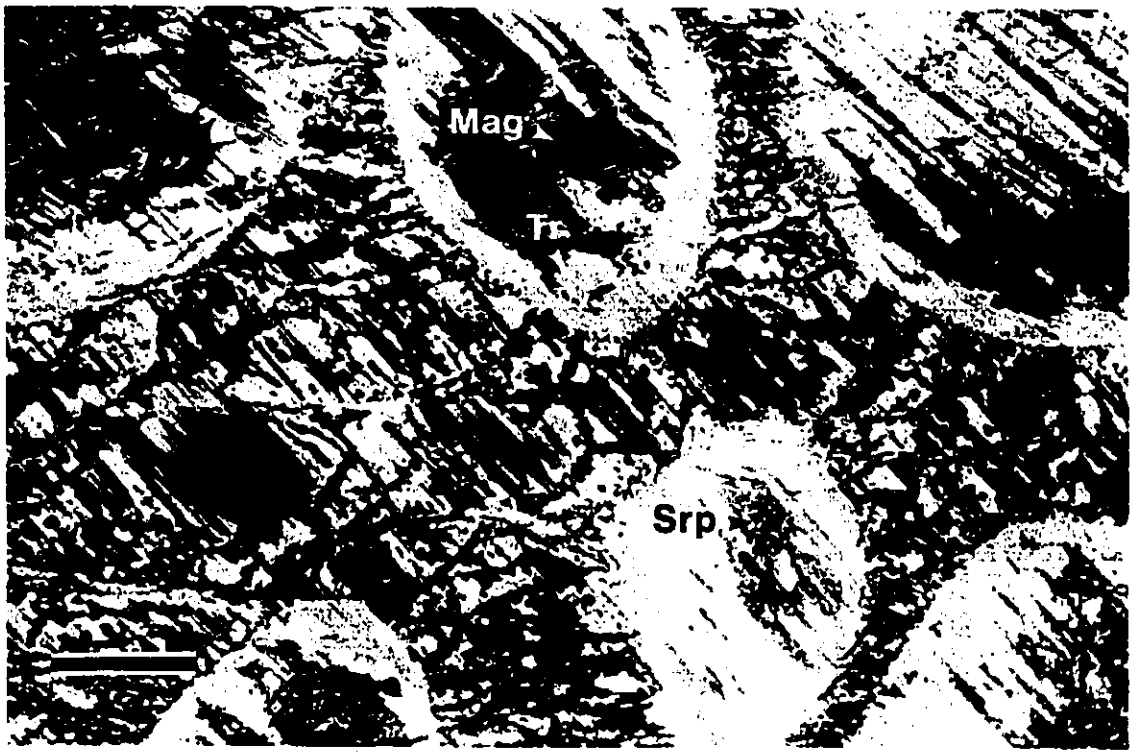
Mag
Srp

3.3 CLINOPYROXENITE LAYERS

The layers of clinopyroxenite are essentially composed of abundant clinopyroxene crystals set in a fine-grained assemblage of secondary minerals. The crystals of clinopyroxene have been slightly altered to actinolite and minor oxyhornblende. The interstitial material is dominated by fine acicular actinolite and chlorite, with minor amounts of pumpellyite, ilmenite and magnetite. Late-stage serpentine and carbonate veinlets were observed in some localities where deformation was more intense. In those areas, relatively large amounts of Fe-rich chlorite and fine-grained disseminated magnetite were found. Modal proportions were determined from the examination of 8 thin-sections and estimated average values are listed in Table 3. The data are reported in a similar manner to those of the peridotite layers. A range in mineral proportions is given, due to the variable degree of alteration as well as changes in the proportions of cumulus to intercumulus material within individual layers.

Contacts between clinopyroxenite and peridotite layers are sharp, as cumulus crystals of clinopyroxene and olivine coexist together along the contact for less than 2 mm in width.

TABLE 3. Modal proportions (vol.%) of clinopyroxenite layers.

clinopyroxene	65	(50-90)	oxyhornblende	<1
actinolite	25	(0-40)	ilmenite	<1
chlorite	8	(1-20)	magnetite	<1
pumpellyite	2	(0-7)	hornblende	tr.

Although the amount of interstitial material is highly variable from one layer to another, it generally increases upwards within individual layers. The two uppermost layers of clinopyroxenite contain significantly more interstitial material.

Clinopyroxene occurs as prismatic crystals having well developed, eight-sided cross sections (Plate 19). Jagged grain boundaries between adjacent crystals are not uncommon, suggesting that partial recrystallization took place (Plate 20). Several crystals show simple twinning along the (100) plane. A distinct bimodal size distribution was observed in all the layers. The coarser-grained crystals average 3 mm in length and account for about two thirds of the total clinopyroxene content, while the smaller ones are approximately 1 mm in size. This distribution was also noted by MacRae (1963). As expected, enlargement of the cumulus grains has taken place during crystallization of the interstitial melt. The adcumulus overgrowths are easily distinguished as they commonly alter to actinolite much earlier than the primary settled crystals. Actinolitization of clinopyroxene is usually restricted to rims, fractures, and cleavage planes of crystals. The actinolite crystals have a distinct fibrous habit. This type of alteration is termed uralitization and is frequently associated with regionally metamorphosed rocks (Deer et al., 1966). Small patches of oxyhornblende within clinopyroxene were observed in the two uppermost layers.

The intercumulus phases have been converted to an assemblage of secondary minerals as a result of regional low-grade metamor-

PLATE 19: Photomicrograph of clinopyroxenite (under crossed nicols) showing well faceted prismatic crystals of clinopyroxene (Cpx) surrounded by very fine grained intercumulus material. Fibrous chlorite (Chl) is a common interstitial phase. Scale bar is 0,2 mm.

PLATE 20: Photomicrograph of clinopyroxenite (under crossed nicols) showing recrystallized grain boundaries (large white arrows) between adjacent crystals of clinopyroxene. Note simple twinning along the (100) plane (black arrow). Scale bar is 0,2 mm.


Cpx
Chl

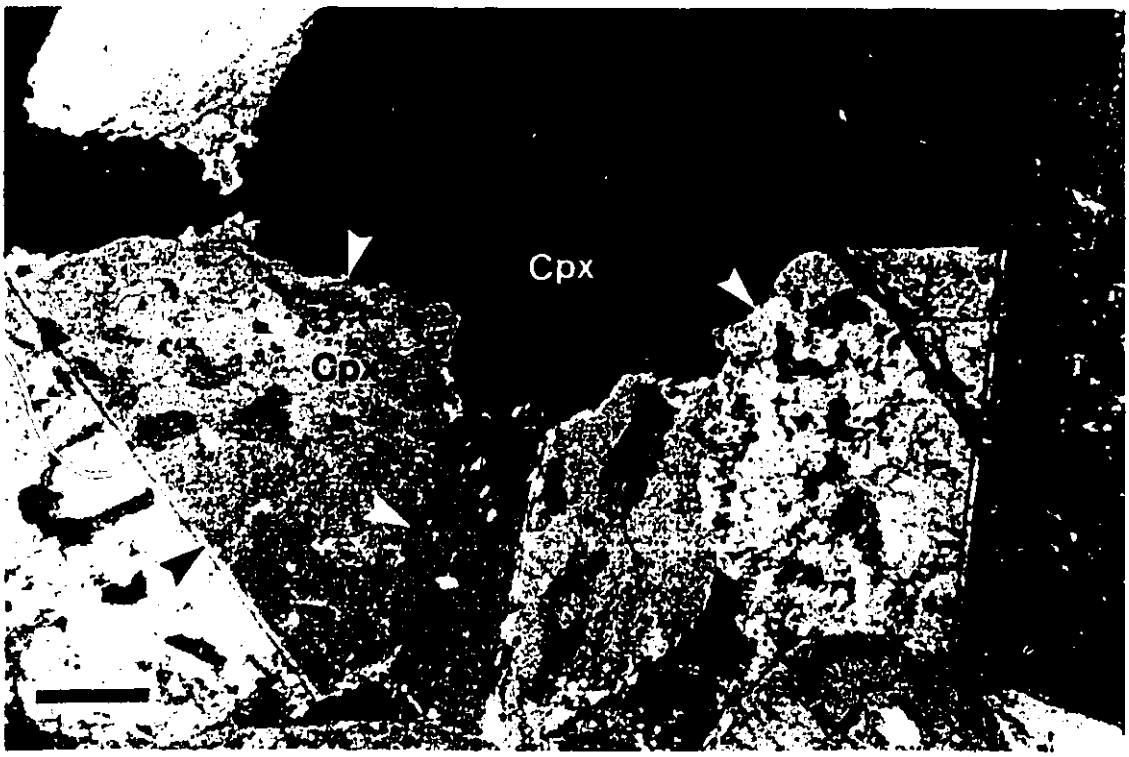
Cpx
Cpx

phism of the upper prehnite-pumpellyite to lower greenschist facies. In the least metamorphosed samples, the interstitial material is composed of a chlorite-pumpellyite assemblage. Chlorite is Mg-rich and occurs either as very fine-grained patches or as radiating fibrous aggregates. Pumpellyite is light brown in colour and occurs as aggregates of acicular crystals, within chloritic masses or fringing clinopyroxene crystals. Pumpellyite-bearing rocks are very common in the Lake Abitibi region near the Quebec-Ontario border (Jolly, 1978).

Extensive lower greenschist metamorphism has overprinted much of the subgreenschist assemblage in the area. Acicular actinolite is the dominant interstitial mineral and is associated with Mg-rich chlorite and minor amounts of Fe-rich chlorite. The top two layers are characterized by the presence of isolated patches of very fine actinolite needles and disseminated oxides, which are interpreted as the alteration products of Ca-poor pyroxene. Such an assemblage was also observed in the upper part of the underlying layers of clinopyroxenite (MacRae, 1963). The presence of oxyhornblende within those particular layers may be an indication that such a reaction has occurred.

The proportion of ilmenite gradually increases upward at the expense of magnetite, and alteration to leucoxene becomes more intense. Ilmenite crystals also become larger up-section, reaching up to 2 mm in size.

3.4 MELAGABBRO LAYER

The layer of melagabbro consists of strongly altered cumulus crystals of plagioclase and clinopyroxene set in a fine-grained interstitial matrix of secondary minerals. The cumulus crystals are preferentially oriented, giving the rock a prominent igneous lamination. The secondary intercumulus assemblage is dominated by fibrous actinolite and epidote, with minor to trace quantities of Mg-rich chlorite, ilmenite, and pyrite. Prior to metamorphism, the cumulus phases constituted approximately 70 vol.% of the rock, and clinopyroxene was slightly more abundant than plagioclase. Secondary minerals were again taken into account in evaluating modal proportions, based on the examination of 2 thin-sections (Table 4). The name uralite has been given to the fibrous, actinolitic mineral partly replacing clinopyroxene crystals, in order to set it apart from the finer-grained, acicular aggregates of actinolite which occur interstitially. Plagioclase, although highly altered, was considered as being part of the modal mineralogy of the rock.

TABLE 4. Modal proportions (vol.%) of melagabbro layer.

plagioclase	30	epidote	5
actinolite	25	ilmenite	1
clinopyroxene	20	chlorite	<1
uralite	20	pyrite	tr.

Clinopyroxene is the dominant primary settled mineral, occurring as elongate prismatic crystals ranging from 2 to 6 mm in length. The crystals are frequently twinned and considerably altered to fibrous actinolite.

Plagioclase occurs as highly elongate, narrow laths measuring approximately 1 mm long by 0.1 mm wide. They are aggregated parallel to each other into small clusters. Plagioclase crystals are altered to a fine-grained, phyllosilicate mineral of undetermined composition (i.e. paragonite, sericite). The extent of alteration is such that grain boundaries are obscured.

The intercumulus material is composed almost entirely of very fine, acicular actinolite and anhedral masses of epidote. The needle-like actinolite crystals are strongly pleochroic and frequently arranged in a radiating pattern. Clusters of Mg-rich chlorite are a minor secondary product in the matrix.

Ilmenite is the dominant opaque mineral, occurring as interstitial, skeletal crystals which are strongly altered to leucoxene. Pyrite is a trace mineral in the matrix and occurs as very fine, disseminated grains.

3.5 UPPER LAYER OF GABBRO

The thick (205 m), uppermost layer of gabbro is a medium- to coarse-grained, subophitic-textured rock composed of moderately to strongly altered crystals of plagioclase and clinopyroxene, with lesser amounts of ilmenite, quartz, magnetite, apatite, pyrite, chalcopyrite, hornblende, carbonate, stilpnomelane, and

zircon. Albitization of plagioclase is complete, with subsequent alteration to sericite and epidote. Clinopyroxene crystals have been partly uralitized to fibrous actinolite, and later replaced by hornblende at some localities. Secondary interstitial phases include fine, radiating aggregates of acicular actinolite, anhedral masses of epidote, and minor chlorite. Micrographic intergrowths of quartz and alkali feldspar were found in variable abundance throughout the layer as an interstitial component. Thin veinlets of epidote and carbonate were also locally observed.

The bottom half of the layer is typically coarse-grained and has a distinct granophyric texture. It is mainly composed of albitized plagioclase, uralitized clinopyroxene, and fine actinolite needles, with lesser proportions of quartz, ilmenite, carbonate, apatite, epidote, and stilpnomelane. Although only 3 thin-sections were examined from this part of the gabbro, modal proportions were nevertheless determined (Table 5), as here the rock is rather homogeneous.

TABLE 5. Modal proportions (vol.%) of the bottom half of the upper layer of gabbro.

plagioclase	50	quartz	3
clinopyroxene	17	apatite	<1
uralite	15	carbonate	<1
actinolite	10	epidote	<1
ilmenite	5	stilpnomelane	tr.

Plagioclase is found as broad laths up to 1 cm in length that are subophitically enclosed within clinopyroxene. The crystals have been weakly sericitized and epidotized, and usually have both simple and polysynthetic twinning.

Clinopyroxene occurs as large, tabular crystals ranging from 1.0 to 1.5 cm in length. The crystals are extensively replaced along their margins by fibrous actinolite (uralite) that exhibits distinct, yellow to blue-green pleochroism. Significant carbonate also occurs along fractures of grains.

Interstitial grains composed of acicular, radiating crystals of pleochroic actinolite are ubiquitous throughout the entire upper layer of gabbro. They are slightly altered to reddish-brown stilpnomelane. The composition of the grains prior to metamorphism is unknown, but is assumed to have been Ca-poor pyroxene, as it is known to alter more readily than clinopyroxene (MacRae, 1965).

Subhedral to euhedral crystals of ilmenite, with typical mesh-like structure, reach up to 2 mm in size. They are partly replaced by stilpnomelane along their rims.

Quartz was found as discrete grains of varying size, or more commonly, forming micrographic intergrowths with alkali feldspar. The latter texture comprises up to 15 vol.% of the rock.

The upper half of the layer has been subdivided into 3 main zones, which will be referred as: 1) marginal gabbro; 2) branching-textured gabbro (BTG); and 3) clotted-textured gabbro (CTG). The petrography of each zone is described separately in

light of their distinct mineralogical and textural character.

3.5.1 Marginal gabbro

The zone of marginal gabbro parallels the upper border of the sill and is approximately 20 m in thickness. The rock is fine-grained and characterized by progressive changes in mineralogy and texture observed away from the intrusive contact. Chilled margins were not observed, possibly due to a lack of exposure. Nevertheless, very fine-grained rock samples were collected within 5 m of the north contact basaltic flow breccia.

Apart from a typical reduction in grain size, other variations observed towards the upper contact include: 1) the appearance of pyrite and rutile; 2) the decrease in ilmenite content; and 3) the increased proportion of clinopyroxene at the expense of plagioclase. In addition, changes in the morphology of plagioclase and clinopyroxene to disequilibrium crystal forms were observed. Due to the highly variable mineralogical composition of the gabbro along the upper margin, evaluation of modal proportions was not attempted.

The following petrographic description is based on a series of samples collected between approximately 5 and 20 m below the contact.

About 20 m from the margin, clinopyroxene crystals change from a tabular to a more prismatic habit, have distinct adcumulus rims, and are very commonly twinned. They average 1 to 2 mm in length and are usually uralitized along the edges. Plagioclase crystals tend

to become smaller and more acicular, their length ranging from 0.5 to 1.0 mm. A few slender, skeletal crystals with hollow cores were also observed.

The interstitial material is dominated by acicular aggregates of actinolite and Fe-rich chlorite. Ilmenite is less common and more intensely altered to leucoxene. Pyrite is the dominant metallic mineral, and it occurs as fine disseminated crystals, or as irregular masses intergrown with minor chalcopyrite. Quartz grains of varying size and fine-grained epidote are minor interstitial phases.

Approximately 5 m away from the border of the intrusion, clinopyroxene becomes more abundant relative to plagioclase, and occurs as narrow, prismatic crystals averaging 0,5 mm in length and having characteristic hollow cores (Plates 21 and 22). Such crystal forms are very similar to the hopper olivines grown experimentally by Donaldson (1976), which also show a combination of planar external faces and skeletal re-entrants. Clinopyroxene crystals show clear evidence of adcumulus growth, the rims being replaced early by fibrous actinolite.

The morphology of plagioclase crystals along the margin is very similar to that of clinopyroxene. The 0.2 to 0.5 mm long crystals occur as slender hieroglyphic-like skeletons having well developed re-entrants and slightly skeletal exterior outlines (Plates 23 and 24). They are frequently found as fan-like aggregates, in which case they may be termed crystallographic branching, or dendritic crystals. Crystallization experiments by Lofgren

PLATE 21: Photomicrograph of marginal gabbro (under crossed nicols) showing prismatic crystals of clinopyroxene (Cpx) having hollow cores. Note the planar external faces and skeletal re-entrants of crystals. Interstitial assemblage is dominated by fine-grained actinolite, chlorite, carbonate and pyrite. Scale bar is 0,3 mm.

PLATE 22: Photomicrograph of marginal gabbro (under crossed nicols) showing a close-up view of the previous plate. Evidence of adcumulus growth is shown by secondary actinolite (Act) fringing crystals of clinopyroxene (Cpx). Scale bar is 0,1 mm.

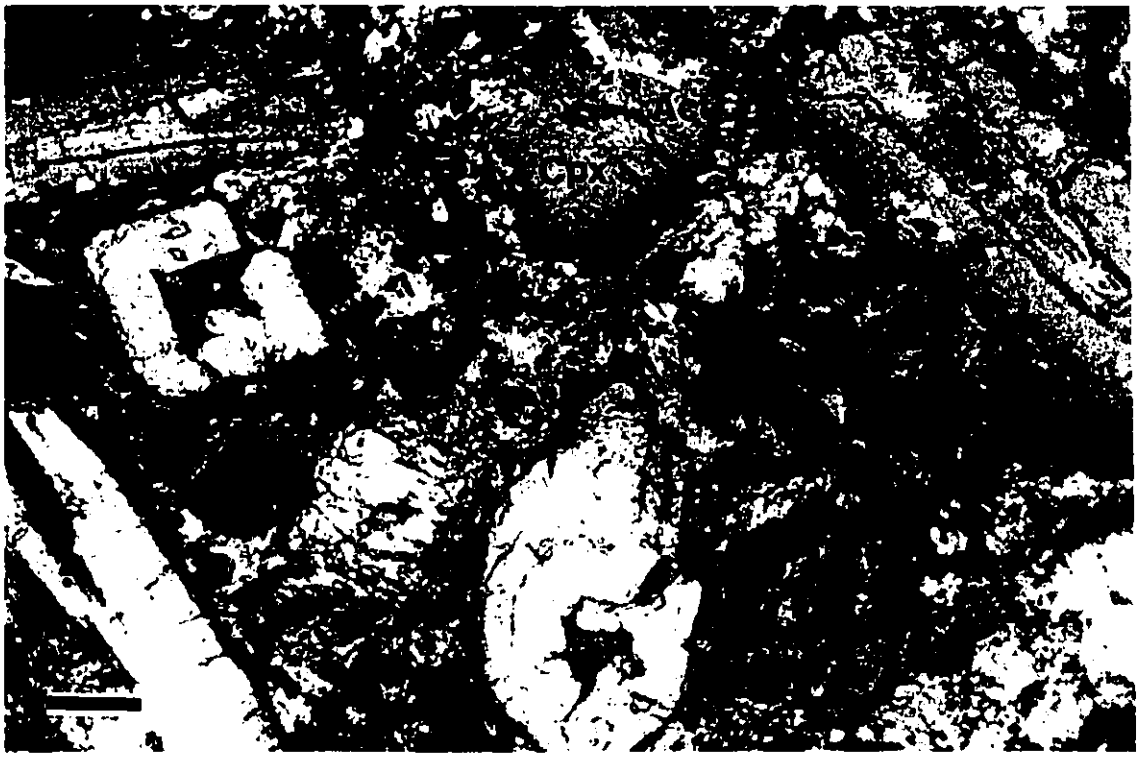

PLATE 23: Photomicrograph of marginal gabbro (under crossed nicols) showing well developed skeletal crystals of plagioclase (Pl). Interstitial minerals include carbonate (Crb) and pyrite (Py), as well as actinolite, chlorite and epidote. Scale bar is 0,3 mm.

PLATE 24: Photomicrograph of marginal gabbro (under crossed nicols) showing a close-up view of the preceding picture. Skeletal crystals of plagioclase (Pl) are mostly surrounded by epidote (Ep) and chlorite (Chl). Scale bar is 0,1 mm.

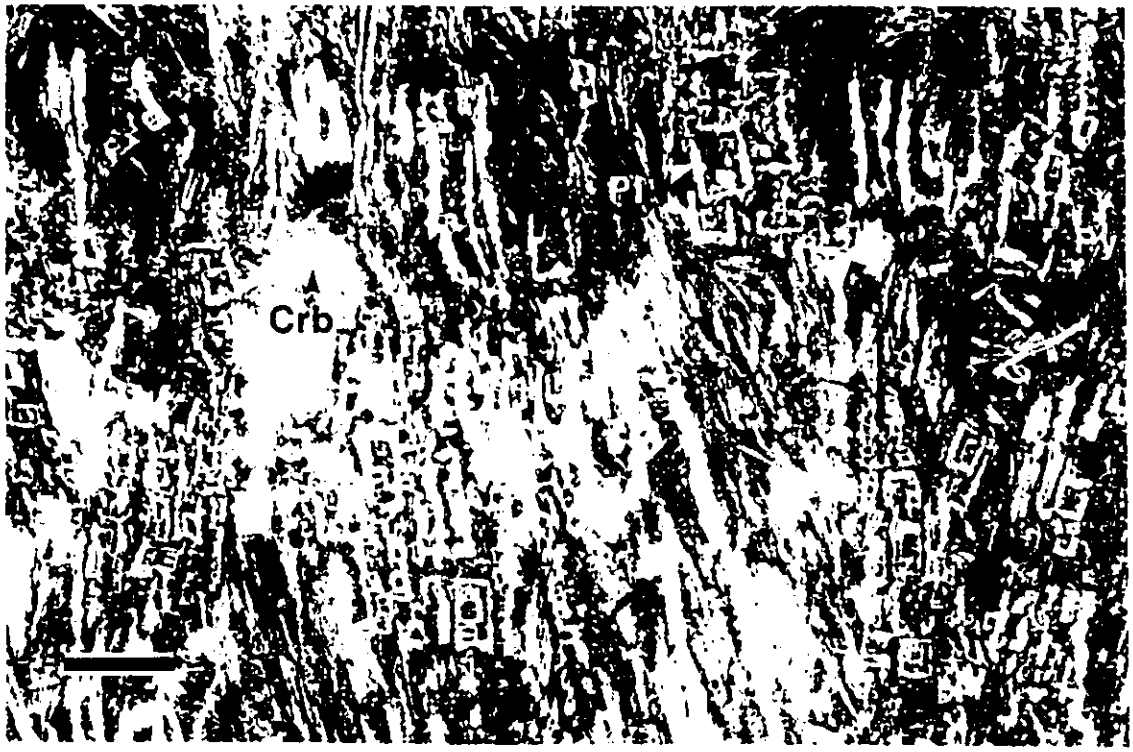
Pl
Crb


Ep
Pl
Ch

(1974) using plagioclase gels yielded comparable morphologies, termed tree-like dendrites, from melts which were undercooled between 150 and 200°C below liquidus temperatures. Fine-grained actinolite and Fe-rich chlorite are still the main interstitial constituents, associated with minor amounts of epidote, and pore-filling carbonate and quartz. A few isolated angular fragments of chlorite, most likely derived from the basaltic breccia to the north, were found adjacent to the contact.

Pyrite constitutes nearly 5 vol.% of the rock, occurring either as rounded globules reaching 2 mm in width, or as fine disseminated crystals. The spherical masses, which also contain chalcopyrite, are interpreted as being primary immiscible sulphide droplets (Wager and Brown, 1967). Very fine, acicular crystals of rutile were observed disseminated throughout the rock.

3.5.2 Branching-textured gabbro (BTG)

A thorough petrographic study was carried out on 3 distinct bands of BTG. A total of 41 thin-sections were examined. Due to major differences in their mineralogy, the branches and the surrounding rock (i.e. matrix) will be described separately. Modal proportions were determined by point counting for both members of the bands.

3.5.2.1 Matrix

Apart from being finer-grained, the matrix portion of the BTG is petrographically very similar to the bottom half of the upper

layer of gabbro. The rock has a characteristic subophitic texture formed of intergrown crystals of moderately altered plagioclase and clinopyroxene (Plate 25). The interstitial mineralogy is dominated by actinolite and ilmenite, with lesser quantities of quartz, epidote, pyrite, magnetite, apatite, carbonate, stilpnomelane, hornblende, and zircon. Granophyric intergrowths of quartz and alkali feldspar are common but less abundant than in the lower portions of the layer. Rare occurrences of epidote and carbonate veinlets were observed.

Estimates of modal proportions were achieved by point counting. The procedure was carried out on 3 thin-sections taken from the same band of BTG. Each sample was collected no more than 10 cm away from a branching texture. Mineralogical proportions of the matrix in other bands, although not accurately determined, approximate the values given in Table 6. Due to the highly variable intensity of alteration throughout the matrix, thin-sections containing the least amount of secondary minerals were selected for point counting.

Plagioclase is by far the most abundant mineral of the matrix, amounting to over 70 vol.% of the rock in certain areas. The crystals are usually lath-shaped and subophitically enclosed within crystals of clinopyroxene, or agglomerated in an interlocking texture. The laths average 1 to 3 mm in length, and usually show both simple and polysynthetic twinning. A few acicular crystals up to 2.5 cm long have been observed at some localities. Partial recrystallization of plagioclase has occurred, as evidenced by the

jagged nature of several grain boundaries, and by the presence of clear rims surrounding the turbid centres of grains. The crystals

TABLE 6. Modal proportions (vol.%) of the matrix determined by point counting.

	7A-52	7A-53	7B-2	MEAN
plagioclase	52.9	48.1	53.8	51.2
clinopyroxene	13.3	20.1	16.9	17.2
uralite	14.2	16.3	11.6	14.2
actinolite	9.7	5.9	9.1	7.9
ilmenite	5.1	7.5	5.6	6.2
quartz	3.0	1.2	1.3	1.7
epidote	1.7	0.9	1.8	1.4
TOTAL	99.9	100.0	100.1	99.8
# of points	700	1050	800	2550

that are enclosed by clinopyroxene have characteristic, wedge-shaped outlines, which results from the faster growth rate of clinopyroxene relative to plagioclase (Kretz et al., 1985). Primary plagioclase crystals have been completely albitized due to regional greenschist metamorphism, and subsequently partly altered to sericite and minor epidote. This is manifested by their clouded appearance in thin-section.

Clinopyroxene occurs as irregular to broad prismatic crystals, partly to totally enclosing laths of plagioclase. They generally range from 2 to 4 mm in size, and are frequently twinned along the (100) plane. The crystals are typically replaced by fibrous

actinolite. In the least altered samples, uralitization is restricted to the rims and along fractures and cleavage planes of crystals. Alteration is however quite intense throughout, such that usually only small patches of clinopyroxene in the core of the grains were observed. Several uralitized crystals were slightly altered to hornblende, probably as a result of local fluctuations in pressure-temperature conditions.

The most common interstitial mineral is secondary actinolite, which occurs as irregular patches up to 1 cm in size. These are composed of crystals of two different habits, namely cryptocrystalline needles and fibrous flakes (Plate 26). The latter often has a fan-like texture, and is optically very similar to the larger uralite crystals replacing clinopyroxene. The actinolitic patches are commonly replaced along their margins by stilpnomelane, which occurs as reddish aggregates of fine, fibrous crystals. This is also found rimming crystals of ilmenite. Brownish-green ferrostilpnomelane is a minor constituent of the matrix, where it similarly replaces actinolite and ilmenite.

Quartz is commonly found in close association with alkali feldspar, either as irregular aggregates in interstices, or as granophyric intergrowths along the margins of plagioclase laths (Plate 27). Subrounded grains up to 1 mm in size are randomly dispersed throughout, and amount to over 5 vol.% of the rock at some localities.

Epidote is a minor secondary phase, occurring as small, radiating aggregates of anhedral crystals interstitial to laths of

PLATE 25: Photomicrograph of the matrix portion of BTG (under crossed nicols) showing typical subophitic texture of intergrown crystals of plagioclase (Pl) and clinopyroxene (Cpx). Note the characteristic wedge-shaped outlines of plagioclase within clinopyroxene (black arrows). Interstitial phases include patchy actinolite (Act) and skeletal to dendritic ilmenite (Ilm). Scale bar is 0,5 mm.

PLATE 26: Photomicrograph of the matrix portion of BTG (under crossed nicols) showing interstitial actinolite occurring as irregular patches of cryptocrystalline needles (Act-1) and fibrous flakes (Act-2). Weakly altered clinopyroxene (Cpx) subophitically enclosing laths of plagioclase (Pl). Scale bar is 0,5 mm.


Act
Pl
Cpx
Ilm


Cpx
Pl
Act-2
Act-1

PLATE 27: Photomicrograph of the matrix portion of BTG (under crossed nicols) showing granophyric intergrowth of alkali feldspar and quartz (large black arrows) surrounding a lath-shaped crystal of plagioclase (Pl). Scale bar is 0,2 mm.

PLATE 28: Photomicrograph of the matrix portion of BTG (under plane polarized light) showing spectacular dendritic crystals of ilmenite (Ilm) weakly altered to leucoxene (Lcx). Scale bar is 0,5 mm.


PI


IIm
LCX

plagioclase. Small amounts of fine-grained epidote within plagioclase were also observed. Other interstitial minerals observed in the matrix include trace quantities of apatite and zircon, which occur as very fine, prismatic crystals.

Ilmenite is by far the most abundant opaque mineral, as it usually constitutes between 5 and 10 vol.% of the matrix. It typically occurs as spectacular skeletal to dendritic crystals reaching up to 5 mm in width (Plates 25 and 28). The crystals have been weakly altered to leucoxene and stilpnomelane. Pyrite and magnetite are rare constituents, the former occurring as small irregular masses filling voids, while magnetite was found as fine disseminated crystals, or intergrown with ilmenite.

3.5.2.2 Branches

Although initially thought to be pyroxene crystals (Fowler et al., 1989a; Johnstone, 1987), it is clear that the branches are a secondary assemblage of minerals. They are interpreted to be composed of altered crystals of olivine that poikilitically host smaller crystals of the matrix. The postulated branching crystals of olivine have been entirely replaced by patches of fine-grained actinolite and epidote, which make up approximately 60 vol.% of the textures. The remaining enclosed material comprises strongly altered crystals of plagioclase, clinopyroxene, and ilmenite, with minor amounts of interstitial quartz, pyrite, magnetite, apatite, and zircon. Only minor granophyric intergrowths of quartz and alkali feldspar were observed.

Modal proportions were evaluated by point counting, which was performed on 4 different thin-sections taken from two separate bands of BTG (Table 7). The relative abundance of minerals in the branches remained fairly constant from one band to the next. Alteration of the primary phases is much more intense in the branches than in the matrix, as most of the original material has been metamorphosed to the lower greenschist facies. Contacts between the branching and matrix portions of the rock are sharp. The transition usually occurs over less than one millimetre.

TABLE 7. Modal proportions (vol.%) of the branches determined by point counting.

	T7-5-82	T7-7B-5A	7A-52	T7-7B-2	MEAN
actinolite	41.3	34.5	29.8	27.9	35.0
epidote	21.0	20.5	32.7	22.9	23.3
plagioclase	15.0	28.5	24.3	22.1	21.9
uralite	12.2	10.3	10.1	17.6	12.1
ilmenite	7.8	3.3	2.3	7.8	5.4
clinopyroxene	2.6	0.9	0.6	1.8	1.6
quartz	0.1	2.0	0.2	---	0.7
TOTAL	100.0	100.0	100.0	100.1	100.0
# of points	1000	860	515	450	2825

The large branching crystals have been completely altered to fine-grained aggregates of actinolite and epidote, which occur as large patches surrounding poikilitically enclosed crystals of uralitized clinopyroxene, albitized plagioclase, and ilmenite

PLATE 29: Photomicrograph of the branch portion of BTG (under crossed nicols) showing aggregates of fibrous actinolite (Act) and epidote (Ep) replacing a poikilitic crystal. Uralitized clinopyroxene (Cpx) and albitized plagioclase (Pl) are the dominant enclosed minerals. Note the radiating form of actinolite (white arrow). Scale bar is 0,3 mm.

PLATE 30: Photomicrograph showing the previous picture under plane polarized light. Note that fractures in plagioclase (Pl) have been infilled by fine-grained actinolite (Act). Scale bar is 0,3 mm.


Ep
Act
Cpx
Pl


Ep
Cl
Pl

PLATE 31: Photomicrograph of the branch portion of BTG (under crossed nicols) showing abundant fine-grained epidote (Ep) and actinolite (Act) enclosing recrystallized laths of plagioclase (Pl). Note that aggregates of epidote and actinolite are distinct and essentially monomineralic. Scale bar is 0,3 mm.

PLATE 32: Photomicrograph of the branch portion of BTG (under crossed nicols) showing large aggregates of needle-like actinolite (Act) and minor epidote (Ep) enclosing crystals of clinopyroxene (Cpx), ilmenite (Ilm) and plagioclase. Scale bar is 0,3 mm.


Ep
Pl
Act


Ep
Ilm
Cpx

(Plates 29 to 32). Actinolite is the dominant alteration product of the poikilitic olivine crystals, forming aggregates of very fine to cryptocrystalline needles, or small fibrous flakes often having a radiating form (Plate 29). Both crystal habits are found in approximately equal proportions throughout the rock. Epidote generally forms as aggregated, fine-grained prismatic crystals which are occasionally arranged in a rosette-like structure. Patches are essentially monomineralic, as only in rare instances do significant amounts of epidote occur within an actinolitic aggregate, or vice versa (Plate 31 and 32). Part of the actinolite may have originated from the alteration of interstitial minerals which crystallized prior to the formation of the olivine crystals.

The poikilitically enclosed minerals, which in fact represent the mineralogy of the matrix at the time of crystallization of the branching olivine crystals, constitute less than half of the total material forming the branches. As expected, the physical properties and relative proportions of the enclosed crystals, namely plagioclase, clinopyroxene, ilmenite and quartz, are basically identical to those found in the matrix described above.

Poikilitically enclosed plagioclase crystals are highly fractured and have been entirely recrystallized. The crystals are clear and not altered to sericite (Plate 31). Isolated grains of epidote have partly replaced plagioclase, whereas fractures have been infilled with fine-grained actinolite (Plate 30). Only a few examples of granophyric intergrowths between alkali feldspar and quartz were observed.

Clinopyroxene crystals are almost completely uralitized to fine fibrous actinolite, with subsequent alteration to hornblende being quite common. Unaltered clinopyroxene is generally found as fractured patches in crystal cores.

Quartz grains up to 4 mm in width are occasionally found, the smaller ones being frequently associated with plagioclase. They are often surrounded by fibrous stilpnomelane, which also fringes ilmenite crystals and patches of actinolite.

Skeletal ilmenite crystals are distinctly finer-grained within the branches, as they range from 0.5 to 2.0 mm wide (Plate 32). Intense alteration to leucoxene has taken place, and ribs of skeletal ilmenite are often seen within diffuse grains of leucoxene. Intergrowths of ilmenite and magnetite were infrequently observed.

Minor apatite crystals and a few scattered grains of zircon were also found.

3.5.3 Clotted-textured gabbro (CTG)

The bands of CTG consist of rounded clots of clinopyroxene crystals set in a coarse-grained matrix of plagioclase and ilmenite, with interstitial clinopyroxene, actinolite, epidote, quartz, apatite, pyrite, and zircon. As opposed to the other portions of the upper gabbro layer, granophyric intergrowths were not observed. Rare occurrences of carbonate and epidote veinlets were locally found.

A petrographic study was carried out on a total of 8 thin-

sections, from which approximate modal proportions were determined (Table 8). Both the spherical clots and the surrounding matrix were taken into account while evaluating the relative mineral abundances. Samples were collected from two separate bands that were texturally and mineralogically very similar.

TABLE 8. Modal proportions (vol.%) of the clotted-textured gabbro.

plagioclase	55	quartz	<1
uralite	20	stilpnomelane	<1
actinolite	15	apatite	tr.
epidote	5	pyrite	tr.
ilmenite	3	zircon	tr.
clinopyroxene	2		

The clots are approximately 2 cm in diameter and are made up of large, radiating crystals of clinopyroxene that show a distinct rosette-like arrangement. The crystals are grossly tabular in shape and average 7 mm in length. They partly to totally enclose smaller crystals of plagioclase, and are almost entirely uralitized to fibrous actinolite. The interstitial material within individual clots is dominated by patches of fine-grained epidote and actinolite. The latter occurs as radiating fibrous flakes and as very fine to cryptocrystalline needles. Minor plagioclase laths are highly fractured and have been recrystallized, as they are very clear and contain no inclusions.

The rock surrounding the clots is a coarse-grained leucogabbro composed of 60 to 75 vol.% of albitized plagioclase crystals, which occur as broad laths averaging 5 mm in length. The crystals mostly show simple twinning, and have been weakly sericitized and epidotized. Minor recrystallization along their margins is made evident by the jagged nature of several grain boundaries. Clinopyroxene is found almost entirely as an interstitial phase to plagioclase, as just a few well developed crystal faces were observed. The anhedral grains generally range from 2 to 4 mm in diameter, and are almost completely altered to uralite, with minor hornblende and stilpnomelane. Aggregates of very fine-grained actinolite fibers (often radiating) occur either as irregular interstitial patches, or forming discrete grains that may likely represent an alteration product of Ca-poor pyroxene. Other interstitial phases include minor to trace quantities of epidote, quartz, apatite, pyrite, and zircon. Ilmenite dendrites reaching 5 mm in width are common. These are replaced by leucoxene and minor stilpnomelane.

CHAPTER 4

GEOCHEMISTRY OF THE CENTRE HILL COMPLEX

4.1 INTRODUCTION

Whole rock samples from layers of peridotite and pyroxenite, the marginal part of the upper layer of gabbro, and a representative collection of the branching and matrix portions of the BTG were analysed for major element oxides and trace elements. In addition, the composition of various minerals from the ultramafic and gabbroic portions of the sill was determined with the electron microprobe.

Samples showing minimal fracturing and surface weathering were carefully selected for analysis. Their locations within the stratigraphic column are shown in Figure 4.

Major elements as well as Ba, Cr, Zr, Sr, Rb, Y, Nb, Zn, Ni, and V were analysed at the University of Ottawa by X-ray fluorescence spectrometry. Ferrous iron was determined by titration, whereas loss on ignition (LOI) was determined by heating samples to 1000°C for 2 hours. A few samples from the marginal gabbro were also analysed for Au, Pt, and Pd, at Bondar-Clegg and Company Ltd. in Ottawa. Analytical procedures and results are presented in Appendix 1.

Figure 8, which depicts the stratigraphic variation of the major element oxides SiO_2, Fe_2O_3, FeO, MgO and CaO, and the Mg

FIGURE 8. Stratigraphic variation diagram of major oxides and Mg number (X) from rocks of the Centre Hill complex. Open circles represent analyses from MacRae (1965). Rock type patterns are the same as in the stratigraphic column of Figure 4 (p.15).

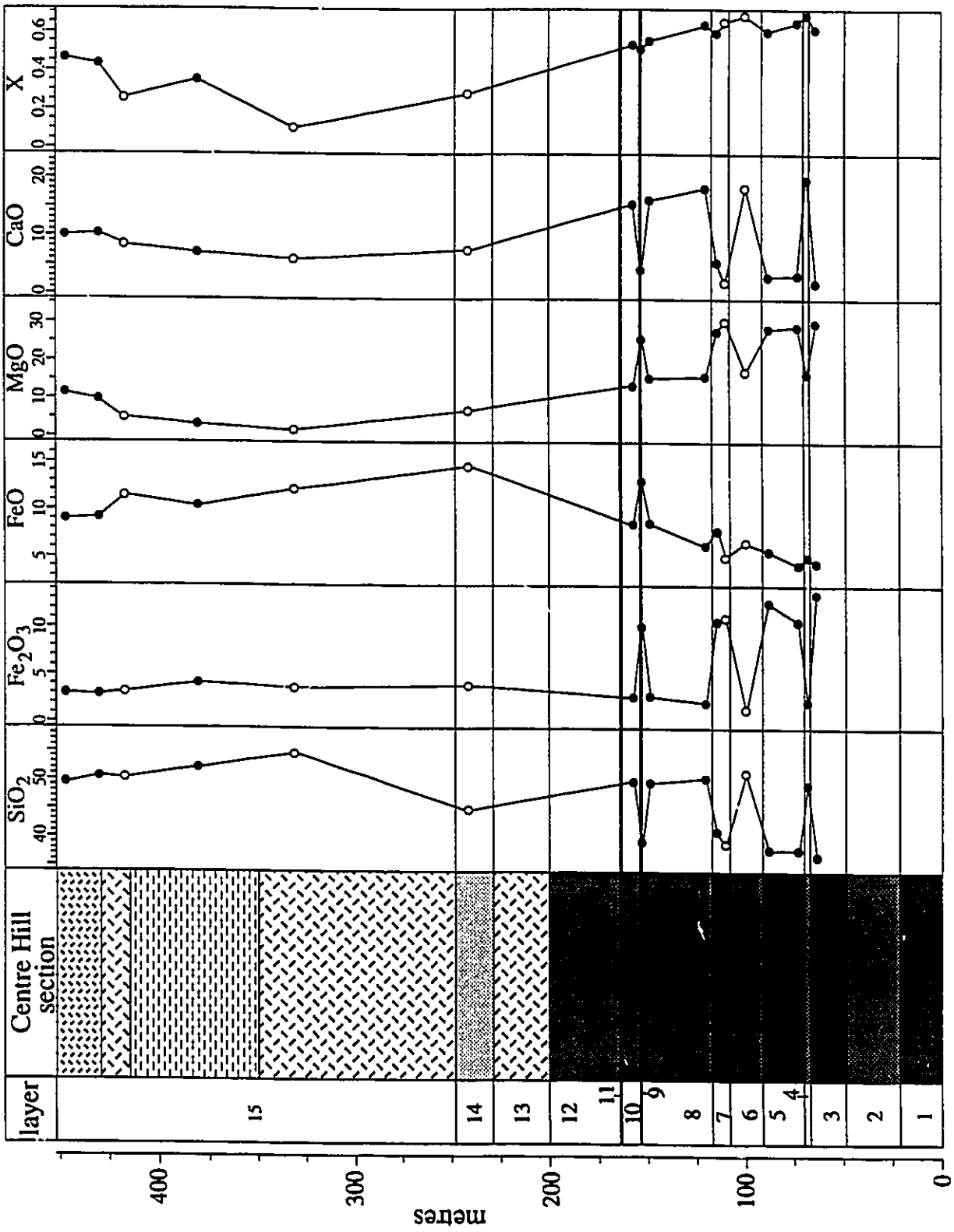
layer
Centre Hill section
SiO2
Fe2O3
FeO
MgO
CaO
X
metres
0
100
200
300
400
1
2
3
4
5
6
7
8
9
10
11
12
13
14
15

number (X), will be referred to frequently in this chapter.

The chemical compositions of clinopyroxene, actinolite, plagioclase, Fe-Ti oxides (i.e. ilmenite and magnetite), tremolite, olivine, and epidote were determined at McGill University by electron microprobe analyses. Analytical procedures and results are presented in Appendix 2.

Before any interpretation based on geochemical results can be attempted, it is essential to study the effects of alteration on the metamorphosed, mafic to ultramafic rocks of the Centre Hill complex.

Mafic rocks of greenschist facies are commonly affected by alkali metasomatism. The "igneous spectrum" diagram of Hughes (1973) has been used to compare the intrusive suite to unaltered rocks in terms of the mobility of Na and K. Although this diagram is typically used to recognize spilitic and keratophyric volcanic rocks, it can also be applied to intrusive rocks. As shown in Figure 9, the composition of rocks from the upper layer of gabbro are plotted in terms of the total combined soda and potash content ($Na_2O + K_2O$) and the potash/soda proportion [$(K_2O/K_2O + Na_2O) \times 100$]. Results indicate that rocks of the matrix portion of the BTG lie outside the "igneous spectrum" in the field of spilites, suggesting substantial additions of Na_2O at the expense of K_2O. The low abundance of alkalis in the branches compared to the matrix can be explained by a concomitant decrease in modal plagioclase, amounting to 51.2 vol.% in the matrix and only 21.9 vol.% in the branches (see Tables 6 and 7). Although rocks from the marginal gabbro do

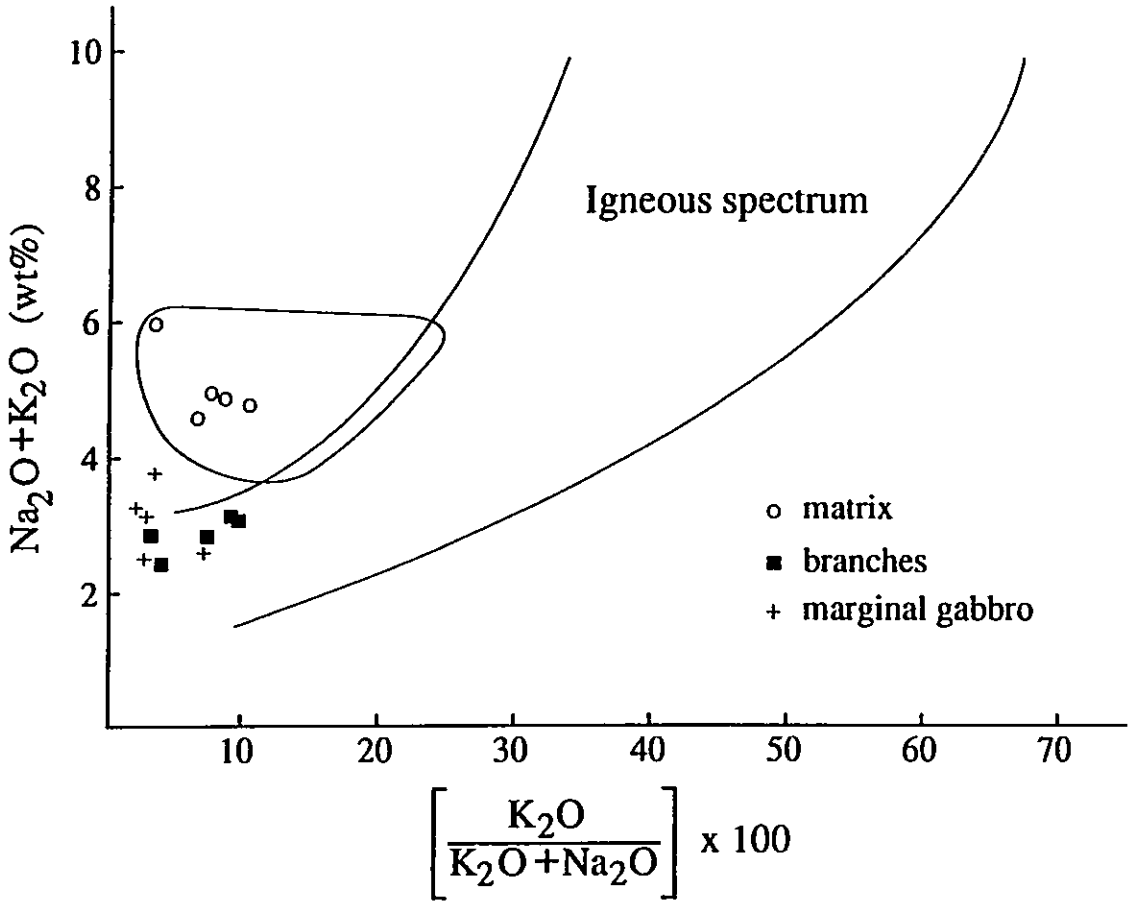

FIGURE 9. "Igneous spectrum" diagram showing rock compositions from the upper layer of gabbro plotted in terms of the total combined potash and soda content, and the potash/soda ratio. The "igneous spectrum" outlines the compositional field of fresh igneous rocks, while the circled area represents the field of spilites (after Hughes, 1973).

not plot in the spilite field, they are nevertheless significantly depleted in K_2O relative to Na_2O.

These results and the low An content of plagioclase demonstrate a significant introduction of Na. Peridotite and pyroxenite samples were not plotted on the diagram in light of their very low abundance in alkalis, explained by the scarcity of plagioclase in ultramafic rocks.

Work by Swinden (1987) on associated mafic volcanic and intrusive rocks of the Wild Bight Group in Newfoundland showed that alkali element mobility was much less evident in mafic sills and dykes. He inferred that alkali metasomatism took place on the seafloor soon after eruption and not from later burial metamorphism. If such a process is responsible for the sodic alteration at Centre Hill, it may imply that the Munro Lake sill crystallized at very shallow levels and could in fact be subvolcanic in origin. A related pyroxenite/gabbro sill found 5 km to the southwest of Centre Hill was described by Johnstone (1987) as extruding westward into a tholeiitic layered flow, further supporting this idea.

4.2 PERIDOTITE LAYERS

4.2.1 Rock chemistry

A total of 5 samples taken from 4 successive layers of peridotite (Figure 4) were analysed for their whole rock chemical composition. Results are tabulated in Appendix 1, Table A.

Whole rock analyses clearly show that the layers become progressively more evolved towards the top of the ultramafic zone.

Geochemical evolution is manifested by an increase in the proportions of SiO_2, Fe_2O_3 + FeO, CaO, Na_2O, Zr and Y, accompanied by a general decrease in MgO, Mg number (X), Cr and Ni (Figure 8; Appendix 1, Table A). A similar trend was also observed within an individual layer (samples Pd-2 and Pd-3). The systematic variation in major and minor elements is interpreted to be related to changes in proportions of mineral phases through fractional crystallization. A gradual decrease in modal olivine and chromite with concomitant increase in clinopyroxene upwards within the peridotite layers of the ultramafic zone has been observed by MacRae (1965).

4.2.2 Mineral chemistry

Chemical compositions of olivine, clinopyroxene, and tremolite were determined by microprobe analyses. The results are listed in Appendix 2, Table A.

Fresh olivine grains were found in a single specimen (Pd-5), which was sampled from the next to last peridotite layer near the top of the ultramafic zone (Figure 4). A total of two analyses were performed from a single polished thin section, giving an olivine composition equivalent to Fo_{71}. Compositions of Fo_{64} were obtained from the same layer by MacRae (1963). However, analytical procedures were then rather primitive, as X-ray determinations were done on olivine samples which were flaked out directly from an uncovered thin section.

The chemical composition of unaltered poikilitic crystals of clinopyroxene was determined from 3 different layers of peridotite,

identified as layers 3, 5, and 9 (Figure 4). Each sample was taken within 3 m of the upper contact, thus making it possible to study the variation in clinopyroxene compositions within different cyclic units. Results indicate that all analysed clinopyroxene crystals are Fe-rich augite in composition, with a slight decrease in the Mg/Mg+FeT ratio (X) being observed with stratigraphic height. As shown in Figure 10, compositions plot in the field of augite directly below the field of diopside in the pyroxene quadrilateral of Morimoto (1989).

Amphibole was typically found replacing both olivine and clinopyroxene in the peridotites. Chemical compositions were determined from 3 successive peridotite layers (3, 5, and 7), and show very little variation between different cyclic units. The amphibole is almost pure tremolite, as the Mg/Mg+FeT ratio averages 0.94.

4.3 CLINOPYROXENITE LAYERS

4.3.1 Rock chemistry

Whole rock analyses were obtained for 4 samples collected from 3 different pyroxenite layers, their location being shown in Figure 4. Results are tabulated in Appendix 1, Table B.

As with the peridotites, layers of pyroxenite also manifest a progressive iron enrichment trend upwards in the section, both within individual layers, and among different cyclic units. A gradual increase in Fe_2O_3, FeO, Na_2O, K_2O, TiO_2, Zr and Y is characteristic of the layers, accompanied by a reduction in the

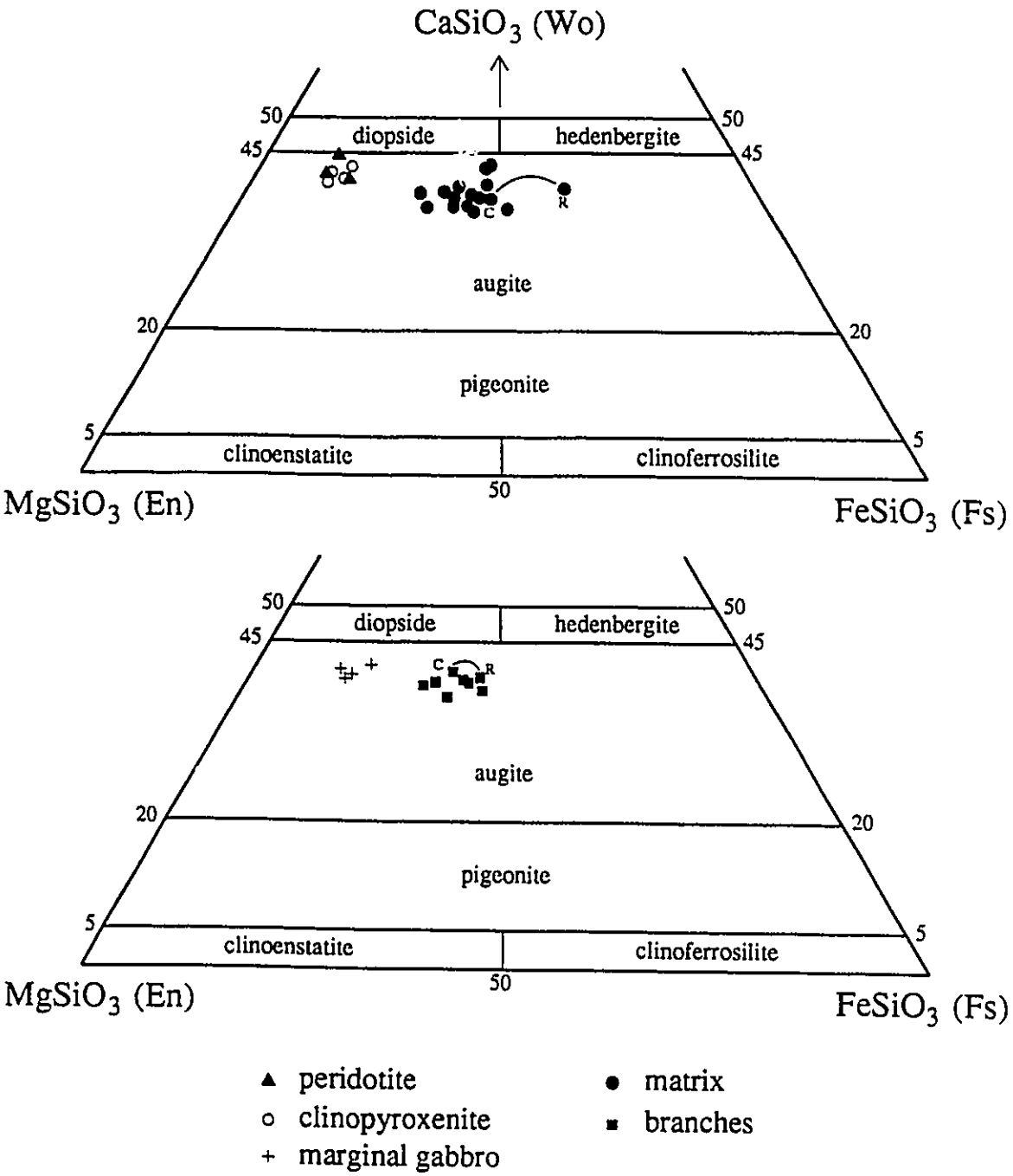

FIGURE 10. Pyroxene quadrilateral diagram showing the composition of clinopyroxene from different rock types of the Centre Hill complex. Analyses of the core (C) and rim (R) of single crystals show evidence of zoning.

proportions of MgO, CaO, Cr, Ni, and Mg number (Figure 8; Appendix 1, Table 2). Such changes may partly be explained by an evolution in the composition of clinopyroxene as well as the gradual increase in modal abundance of intercumulus plagioclase towards the top of the ultramafic zone and individual layers. Early partitioning of the compatible trace elements Cr and Ni into clinopyroxene explains their gradual decrease in relative abundance with fractional crystallization. Incompatible elements such as Zr and Y become more abundant as they preferentially partition into the residual liquid.

4.3.2 Mineral chemistry

The chemical composition of clinopyroxene crystals was determined from 4 consecutive layers of clinopyroxenite (layers 4, 6, 8, and 10 of Figure 4). Results of the analyses are listed in Appendix 2, Table B. Other minerals were not analysed because of their relatively low abundance in the rocks.

The clinopyroxene crystals are augitic in composition, and a slight decrease in the Mg number is observed upwards in the stratigraphy (Figure 10). Compositions range from $Wo_{41}En_{50}Fs_{09}$ in layer 4 to $Wo_{42}En_{47}Fs_{11}$ in the tenth layer. Note that the clinopyroxene compositions are very similar to those determined from the peridotite layers, and that the chemical trends are nearly identical.

4.4 UPPER LAYER OF GABBRO

4.4.1 Marginal gabbro

4.4.1.1 Rock chemistry

Whole rock chemical compositions were determined for 5 samples collected within 20 m of the upper contact with the host basaltic breccia. Two of these samples were also analysed for Pt, Pd, and Au. Analyses are recorded in Appendix 1, Table C.

A decrease in the proportions of SiO_2 and CaO, with concomitant increase in MgO and Mg number, is observed towards the margin of the sill, as shown by the compositions of samples Mgb-1 and Mgb-2 from the stratigraphic variation diagram of Figure 8.

The amount of Au in both analysed samples is quite significant, whereas Pt and Pd are slightly anomalous. Platinum Group elements (PGE) and Au typically partition early into sulphide-bearing minerals at the margins of mafic layered intrusions. Unfortunately, samples from the bottom peridotite layers were not analysed for these elements.

4.4.1.2 Mineral chemistry

The chemical composition of 4 clinopyroxene crystals was obtained from the northern margin of the upper layer of gabbro, and results are given in Appendix 2, Table C. As shown from Figure 10, the analysed crystals are Mg-rich augite, being similar in composition to the clinopyroxene grains analysed from the layers of peridotite and clinopyroxenite.

4.4.2 Branching-textured gabbro: Matrix

4.4.2.1 Rock chemistry

A total of 5 matrix samples collected from 2 different bands of BTG were analysed for major oxides and minor elements. The matrix and branch portions were separated from the same rock specimen in order to adequately compare their chemical compositions. Analytical results are listed in Appendix 1, Table D.

The rock making up the matrix is relatively enriched in SiO_2, Na_2O, Ba, Zr, Sr, Y and Nb, and contains reduced amounts of MgO and CaO. A significant enrichment in iron at the expense of magnesium is observed, as shown by the reduced Mg number. Remobilization of potassium during Na-metasomatism could explain the very low K_2O content.

Major element analyses of MacRae (1963) on the middle part of the upper layer of gabbro are very similar to those of the matrix, further supporting their strong petrographic resemblance (Tables 5 and 6). However, the central portion of the gabbro is slightly more felsic when compared to the BTG as a whole. The latter analysis, which is depicted in the middle part of the banded zone in Figure 8, was calculated by taking the mean composition of the matrix and branches, and estimating the proportion of branches to equal 20 vol.% of the BTG.

4.4.2.2 Mineral chemistry

The chemical compositions of clinopyroxene, plagioclase, actinolite, and Fe-Ti oxide were determined, and results are shown

in Appendix 2, Table D.

A total of 15 analyses were obtained from relatively unaltered clinopyroxene crystals within 4 different thin sections. Chemical compositions are quite variable because of zoning. The analysed crystals lie in the field of augite on the pyroxene quadrilateral (Figure 10). The chemistry of clinopyroxene ranges from $Wo_{39}En_{40}Fs_{21}$ to $Wo_{40}En_{23}Fs_{37}$, with an average value of $Wo_{39}En_{27}Fs_{34}$. A traverse from the core to the rim was done on a single crystal to study the degree of compositional zoning (cpx-33 and cpx-34). As expected, a decrease in the Mg number is observed towards the margin of the grain, as the composition varies from $Wo_{39}En_{32}Fs_{29}$ to $Wo_{40}En_{23}Fs_{37}$.

The composition of 10 plagioclase crystals from 4 different thin sections shows that crystals have all been strongly albitized. Plagioclase crystals average $An_{3.7}$, and reach a maximum of $An_{5.9}$, which is within the range of compositions given by Turner (1981) for low-grade metamorphic rocks (An_{0-7}). A set of analyses taken from the centre and margin of a crystal showed no evidence of zoning.

Seven crystals of secondary amphibole (i.e. actinolite) have been chemically analysed from 4 separate samples of the matrix. Two different types of actinolite were probed, namely the fibrous crystals replacing clinopyroxene (uralite), and the interstitial aggregates of very fine grained, acicular crystals. Both varieties yielded the same composition, and were thus most likely formed by the same alteration process. The actinolite has a relatively high iron content, expressed by a reduced Mg number that averages 0.33

(Appendix 2, Table D). The low abundance of Na_2O, Al_2O_3, and Fe_2O_3 clearly sets this mineral apart from common hornblende.

The composition of skeletal and dendritic crystals of Fe-Ti oxide were determined from two adjacent samples. The crystals contain highly variable proportions of TiO_2, Fe_2O_3, and FeO. The amount of TiO_2 varies from 5.4 to 44.0 wt.%, representing a range in composition from magnetite to ilmenite. Titaniferous magnetite with 28.4 wt.% TiO_2 was also probed from a morphologically similar crystal, suggesting an exsolution reaction between the coexisting solid solutions of magnetite-ulvöspinel and hematite-ilmenite (Buddington and Lindsley, 1964).

4.4.3 Branching-textured gabbro: Branches

4.4.3.1 Rock chemistry

Whole rock chemical analyses were obtained from 5 samples of the branches collected from the same two bands as the analysed matrix samples. Parts of the branches were carefully separated from the gabbroic rock by cutting out small chips no more than 2 cm^3 in size in order to obtain homogeneous samples. Results are presented in Appendix 1, Table E.

Geochemical analyses show that the branches are strongly enriched in iron, the average Mg number being only 0.16. The reduced proportions of SiO_2 and MgO likely reflect the original composition of the branching crystals, now represented by secondary actinolite and epidote, which comprise approximately 60 vol.% of the textures. As shown from Table 9, there are significant diffe-

Table 9. Average chemical composition of branches and matrix.

	BRANCHES	MATRIX		BRANCHES	MATRIX
SiO_2	43.21	54.53	Ba	33	107
Al_2O_3	14.14	13.44	Cr	32	32
Fe_2O_3	7.26	3.41	Zr	95	146
FeO	14.43	9.58	Sr	234	275
MgO	4.25	3.45	Rb	----	4
CaO	7.92	6.94	Y	30	41
Na_2O	2.57	4.72	Zn	106	66
K_2O	0.19	0.36	Ni	27	28
TiO_2	1.73	1.67	V	240	168
P_2O_5	0.11	0.11			
MnO	0.31	0.21			

rences in the chemical composition of the average branches and matrix sample, which correlate with the respective proportions of mineral phases (see Tables 6 and 7). The presence of poikilitically enclosed crystals of clinopyroxene, plagioclase and Fe-Ti oxide within the branches explains the high amounts of Al_2O_3, Na_2O, TiO_2, P_2O_5, Zr, Sr, and Y, and reduced contents of Cr and Ni, relative to other silica-depleted rocks (i.e. peridotites).

4.4.3.2 Mineral chemistry

Chemical compositions were determined for actinolite, plagioclase, clinopyroxene, epidote, and Fe-Ti oxide. Analytical results are presented in Appendix 2, Table E.

A total of 13 crystals of actinolite were selected for

analysis from 5 different thin sections. Similar to the matrix, both types of actinolite have comparable chemical compositions. Notable variations in the proportions of SiO_2, Al_2O_3, FeO, MgO, and Na_2O are observed, which contrasts with the relatively uniform composition of actinolite in the matrix. Compared with the matrix, actinolite crystals within the branches contain on average more Al_2O_3 and less total FeO, which is a typical progression observed with increasing metamorphic grade (Kretz, 1986).

The composition of 6 plagioclase crystals was determined from 3 separate samples. Results show a significant range from $An_{3.4}$ to as much as $An_{13.7}$. Plagioclase crystals are on average notably more calcic in the branches than in the matrix ($An_{6.9}$ vs. $An_{4.2}$). This may be explained by slow diffusion of Ca and Na through the branching crystal enclosing the plagioclase.

A total of 9 analyses of clinopyroxene were obtained. Results show very little variation, as all compositions are within the field of augite (Figure 10), ranging from $Wo_{39}En_{40}Fs_{21}$ to $Wo_{38}En_{34}Fs_{28}$. Analyses cpx-38 and cpx-39, which represent respectively the core and rim of a crystal, indicate very subtle zoning, with increases in FeO towards the margin at the expense of MgO. Clinopyroxene crystals are on average slightly more magnesian within the branches than in the matrix, as shown by their respective Mg number of 0.59 and 0.56.

The chemical composition of 2 crystals of the epidote group was determined, and analytical results indicate that they are nearly pure epidote due to the abundance of Fe^{+3} in their chemical

formula (Appendix 2, Table D). The replacement of Al by Fe^{-3} is almost complete, given the high concentration of $Ca_2Fe_3^{+3}Si_3O_{12}(OH)$ in the average analysis, which is equal to 27.8 molecular per cent.

A total of 4 skeletal crystals of Fe-Ti oxide were analysed from the branches. Their composition is very close to pure ilmenite, as the analyses contain between 49.0 and 49.5 wt.% TiO_2. Significant proportions of Cr_2O_3, amounting to over 3.0 wt.% in one particular crystal, are characteristic of ilmenite in both the branches and the matrix.

4.5 STRATIGRAPHIC GEOCHEMICAL VARIATIONS

The geochemical evolution of the Centre Hill complex, from the bottom ultramafic layers to the upper marginal gabbro, is clearly illustrated in the stratigraphic variation diagram of Figure 8. Based on the systematic variations in the proportions of SiO_2 and CaO, and on the Mg number (X), it is strongly suggested that the sill solidified from both margins simultaneously, and that the last portion of melt to crystallize was "sandwiched" somewhere within the bottom half of the upper layer of gabbro.

The analysis of the bottom portion of the upper layer of gabbro, obtained from MacRae (1965) and located approximately 325 metres from the base of the sill, reaches a maximum in terms of silica enrichment and has the lowest Mg number (X) relative to all other analyses. Furthermore, it is where the proportion of CaO reaches a minimum value in the upper layer of gabbro, suggesting a reduction in modal clinopyroxene and an increase in late-

crystallizing phases like calcium-poor pyroxene and quartz. The extremely low abundance of CaO in the layers of peridotite is simply associated with the limited amount of clinopyroxene in these rocks.

The general upward decrease in Mg number observed from one peridotite/clinopyroxenite cyclic unit to the next strongly supports an origin whereby the parent magma gradually evolved through fractionation. A model explaining the origin of these cyclic units is proposed in the following chapter.

4.6 METAMORPHISM

According to Jolly (1978), greenschist grade metamorphic rocks in the Abitibi Subprovince have originated from low pressure metamorphism, partly overprinting pumpellyite-prehnite-bearing rocks related with depth of burial.

4.6.1 General metamorphic reactions

Four main reactions have played a major role in the metamorphic history of the rocks at Centre Hill:

(1) serpentinization of olivine in the layers of peridotite
(2) tremolitization of serpentine and clinopyroxene superimposed over serpentinization in the layers of peridotite.
(3) replacement of clinopyroxene by actinolite in the layers of clinopyroxenite and gabbro.
(4) albitization, sericitization, and epidotization of plagioclase in the layers of clinopyroxenite and gabbro.

The serpentinization of olivine in peridotite took place at temperatures below 400°C and at very low values of X_{CO2}, as serpentine typically alters to magnesite when the amount of CO_2 exceeds 10 mole percent in the fluid phase (Winkler, 1979). The simplified hydration reaction is as follow:

3 forsterite + 4 H_2O + SiO_2 = 2 serpentine

(after Deer et al., 1966)

Antigorite is the serpentine mineral phase, as it forms from the inversion of chrysotile at the onset of metamorphism (Turner, 1981).

With increasing metamorphic grade, serpentine reacted with clinopyroxene to give tremolite by the following reaction:

1 serpentine + 2 diopside + 2 SiO_2 = 1 tremolite + 1 H_2O

(modified after Skippen, 1974)

Superposition of tremolite over serpentine is clearly observed in the rocks, where tremolite partly replaces serpentine along the margins of altered olivine grains (Plate 14).

In the clinopyroxenitic and gabbroic layers, clinopyroxene crystals are partly to totally replaced by large, oriented grains of actinolite having a fibrous habit (uralite). Replacement is restricted to cleavage planes and grain boundaries in the least altered samples. Actinolite replacement of clinopyroxene, which first occurs in the uppermost prehnite-pumpellyite facies (Dimroth and Dressler, 1978), is frequently accompanied by the formation of very fine needles of actinolite as an interstitial constituent. The

latter type of actinolite is by far the dominant interstitial phase to occur in the gabbroic layers. The following unbalanced reaction for the formation of actinolite is proposed:

clinopyroxene + plagioclase + H_2O = actinolite

Rare occurrences of hornblende partly replacing actinolite crystals along their rims were observed in the layers of gabbro, indicating fluctuations in metamorphic conditions.

Although magmatic clinopyroxene in mafic igneous rocks is usually replaced by an assemblage of actinolite and chlorite under hydrous conditions, the later phase is commonly absent in rocks which are highly actinolitized (Jolly, 1978). The presence of chlorite in the Centre Hill complex is mostly restricted to the upper margin of the intrusion, where interactions with the adjacent volcanic rocks has occurred.

Plagioclase crystals within the layers of clinopyroxenite and gabbro have been entirely replaced by nearly pure albite, and variable amounts of fine grained sericite and epidote. Patches of aggregated epidote grains are found interstitially throughout the layers of gabbro, being most likely formed in conjunction with both the albitization and actinolitization reactions.

Based on such petrographic and field evidence, it was determined that rocks of the Centre Hill complex have been metamorphosed from the upper prehnite-pumpellyite to middle greenschist facies.

4.5.2 Metamorphism of branches

As previously mentioned, the branching olivine crystals have been entirely replaced by an assemblage of secondary minerals. The reacting phases include both the large poikilitic crystals of olivine and the hosted, smaller crystals of clinopyroxene, plagioclase, and ilmenite. Data from evaluated modal proportions and mineral analyses have been used in balancing the following reaction equation:

$$2.7\underset{\text{clinopyroxene}}{Ca_{0.8}(Mg_{0.7}Fe_{0.5})Si_{1.9}Al_{0.1}O_6} + 2.5\underset{\text{olivine}}{(Fe_{1.75}Mg_{0.1}Mn_{0.1})SiO_4}$$
$$+ 1.22\underset{\text{anorthite}}{CaAl_2Si_2O_8} + 0.81\underset{\text{albite}}{NaAlSi_3O_8} + 0.02\underset{\text{orthoclase}}{KAlSi_3O_8}$$
$$+ 0.5\underset{\text{ilmenite}}{FeTiO_3} + 1.1\underset{\text{quartz}}{SiO_2} + 1.5H_2O$$

$$\rightarrow\ 1.2\underset{\text{actinolite}}{Ca_{1.7}Fe_{3.0}Mg_{1.7}Al_{0.9}Si_{7.5}O_{22}(OH)_2}$$
$$+ 1.0\underset{\text{albite}}{Na_{0.9}Ca_{0.1}K_{0.02}Al_{1.1}Si_{2.9}O_8}$$
$$+ 0.6\underset{\text{epidote}}{Ca_{1.9}Fe_{0.8}Al_{2.2}Si_3O_{12}(OH)} + 0.8\underset{\text{magnetite}}{Fe_3O_4} + [(0.5)Ti + (0.25)Mn]$$

volume change of reaction:

$$\underset{116}{\text{olivine}} + \underset{186}{\text{clinopyroxene}} + \underset{123}{\text{anorthite}} + \underset{81}{\text{albite}} + \underset{2}{\text{orthoclase}}$$
$$+ \underset{16}{\text{ilmenite}} + \underset{25}{\text{quartz}} = 549$$

$$\rightarrow\ \underset{325}{\text{actinolite}} + \underset{100}{\text{albite}} + \underset{83}{\text{epidote}} + \underset{35}{\text{magnetite}} = 543$$

The original composition of plagioclase was estimated at An_{60}, while that of olivine was fixed at Fa_{95}. The nearly pure fayalitic composition of the olivine is supported by the high proportion of

Fe_2O_3 in the whole rock analyses, and by the brick red colouration of the branches on the weathered outcrop surface. Similar olivine compositions have also been reported from ferrodiorites of the Skaergaard and Bushveld intrusions (Wager and Brown, 1967). All elements were balanced except for Ca and Na, which were possibly mobilized by metasomatic processes.

The volume change for the reaction was calculated in arbitrary units of volume, and is approximately equal to zero. The combined volume of olivine and clinopyroxene is less than that of actinolite, implying that some plagioclase was also involved in the formation of actinolite. Most of the components used to produce epidote were taken from plagioclase, whereas the iron was apparently supplied by fayalite. The remainder of Fe in olivine was used to produce magnetite. It is interesting to note that the combined volume of olivine, clinopyroxene and plagioclase is exactly the same as that of actinolite, albite and epidote.

The cumulative chemical composition determined from the 5 reactants of the above reaction equation is given in Table 10, where it is compared to the mean whole rock composition evaluated by X-ray fluorescence spectrometry. The relative abundance in weight per cent of each reacting phases was calculated from the molar values given by the reaction. The major oxide composition of each mineral was then multiplied by its relative abundance, and individual components were added together, giving an estimate of the chemical composition of the branches prior to alteration. For comparative purposes, mineral and whole rock analyses have been

recalculated to a total of 100 weight per cent.

The primary chemical composition of the branches determined using the hydration reaction is relatively similar to the composition obtained by XRF analysis, the latter being representative of the secondary mineral assemblage. Significant differences however exist in the proportions of Al_2O_3, CaO, Na_2O, and TiO_2. A decrease in CaO with concomitant increase in Na_2O with alteration is not surprising, as the rocks have been altered by the introduction of Na. The abundance of TiO_2 in the original composition may be due to an overestimate of the amount of ilmenite, while the low total of Al_2O_3 is apparently the result of excessive clinopyroxene at the expense of plagioclase.

The cumulative chemical composition given in Table 11 was calculated from the modal mineralogy of the branches as determined by point counting. Results show that the major oxide chemistry of the metamorphosed branches given by XRF analysis and using modal proportions are also quite comparable. Differences in the amount of SiO_2, Al_2O_3, FeO_T, and CaO could be due to an insufficient number of analysed samples, considering the highly variable compositions obtained by XRF, and to the wide range in modal proportions between samples. It is to be noted that epidote was analysed by microprobe only from the matrix portion of the BTG, and that its composition was assumed to be identical within the branches.

Table 10. Cumulative major oxide composition of reactant phases.

wt.%	oliv (27.2)	cpx (33.6)	plag (30.4)	ilm (5.0)	qtz (3.8)	TOTAL	XRF
SiO_2	31.6	50.5	53.0	0.02	100	45.6	45.0
Al_2O_3	0.5	1.7	29.8	0.03	---	9.7	14.7
FeO_T	61.4	15.3	0.5	48.1	---	24.4	22.6
MgO	3.0	12.4	0.1	0.02	---	5.0	4.5
CaO	1.5	18.8	12.3	0.06	---	10.5	8.2
Na_2O	---	0.4	4.2	---	---	1.4	2.7
TiO_2	0.7	0.5	---	49.4	---	2.8	1.8
K_2O	---	0.02	0.1	---	---	0.05	0.2
MnO	1.3	0.4	---	2.4	---	0.5	0.3
TOTAL	100.0	100.0	100.0	100.0	100	100.0	100.0

Table 11. Cumulative major oxide composition of modal phases.

vol%	act (49.3)	epid (26.5)	alb (16.5)	ilm (3.4)	mgt (2.0)	cpx (1.6)	qtz (0.7)	TOTAL
SiO_2	50.7	38.9	66.2	0.02	0.1	50.5	100	47.7
Al_2O_3	4.9	23.9	21.0	0.03	3.1	1.7	---	12.3
FeO_T	24.0	14.4	0.4	48.2	90.1	15.3	---	19.4
MgO	7.8	---	0.04	0.02	0.03	12.4	---	4.1
CaO	11.0	22.2	1.4	0.06	0.03	18.8	---	11.7
Na_2O	0.7	0.4	10.6	---	---	0.4	---	2.3
TiO_2	0.2	---	0.01	49.3	6.3	0.5	---	2.0
K_2O	0.2	---	0.3	---	---	0.02	---	0.1
MnO	0.5	0.2	0.02	2.4	0.3	0.4	---	0.4
TOTAL	100.0	100.0	100.0	100.0	100.0	100.0	100	100.0

CHAPTER 5

PETROGENESIS OF THE CENTRE HILL COMPLEX

5.1 INTRODUCTION

The Centre Hill complex is a cyclically layered mafic intrusion similar in characteristics to the well documented Muskox Intrusion (Irvine, 1980; Irvine and Smith, 1967), the Rhum Layered complex (Emeleus, 1987), and the Stillwater complex (Jackson, 1961; McCallum et al., 1980; Raedeke and McCallum, 1984). Although much smaller in size than the above, the Centre Hill complex is considered as a stratiform-type intrusive complex, based on conspicuous rhythmic layering, and a gradual upward evolution in chemical composition. Satterly (1952) and MacRae (1965) both described the Centre Hill body as a stratiform differentiated sill. However, Taylor (1955) and Grubb (1962) hypothesized an alpine-type classification, in that the sill would have been emplaced in a tectonically active belt. The origin postulated by Taylor was primarily based on the apparent lack of cryptic layering, which is wrong and likely due to inaccurate chemical data. Grubb proposed that the layering originated from multiple injection of magma following differential fusion of the peridotite substratum, and that a very limited degree of gravitational differentiation actually took place.

The purpose of this chapter is to postulate a petrogenetic

sequence explaining the occurrence of: 1) cyclic units within both the ultramafic succession and the upper layer of gabbro of the Centre Hill complex; and 2) branching olivine crystals within the bands of BTG.

The origin of the branching olivine crystals, although briefly considered henceforth, will be discussed in detail in the following chapter once the petrogenetic framework has been established.

5.2 ORIGIN OF MAGMA

The Centre Hill primary magma was calculated as having an olivine tholeiite composition (MacRae, 1965) based on the basalt classification of Yoder and Tilley (1962). The primary liquid composition was determined by multiplying the average composition of the three dominant rock types, namely peridotite, clinopyroxenite, and gabbro, by their respective condensed thickness, and calculating a mean value. It was assumed that each batch of magma had essentially the same composition. Abundant associated tholeiitic basalt throughout the whole area further supports such a primary liquid composition.

It is now universally accepted that the upper mantle is the source region for most basaltic magma, and that it has a lherzolite composition (Morse, 1980). Assuming that the primary liquid had an olivine tholeiite composition, it can be presumed that the Centre Hill magma was derived from the fusion of plagioclase lherzolite at relatively shallow depths (P ~ 5 kb).

Further evidence supporting an olivine tholeiite liquid comes from the AFM variation diagram (Figure 11). The general trend shows an iron enrichment during initial crystallization, followed by an increase in alkalis in the latest stages. The dry and reduced nature of the tholeiitic magma, which tends to concentrate Mg in olivine and pyroxene early during fractionation, results in increasingly greater proportions of Fe^{+2} in the residual liquid along with the alkali-rich fraction.

The average composition of the BTG on an AFM diagram was determined using the ratio of matrix to branch material in the rock (evaluated at approximately 8 to 2). Data points representative of the branches, while clearly illustrating the strong enrichment in Fe relative to the matrix, should not be considered as being part of the intrusive suite, as the branches were originally composed of an assemblage of minerals that crystallized at different stages (i.e. poikilitic crystals and enclosed crystals). The general depletion of alkali elements in the marginal gabbro relative to the underlying BTG strongly suggest that crystallization took place from the roof inwards.

5.3 ORIGIN OF CYCLIC LAYERING

5.3.1 Introduction

It is commonly accepted that the cyclic repetition of cumulate strata in layered intrusions originates from the periodic replenishment of magma to the chamber. Such interpretation is strongly favoured in explaining the origin of cyclic

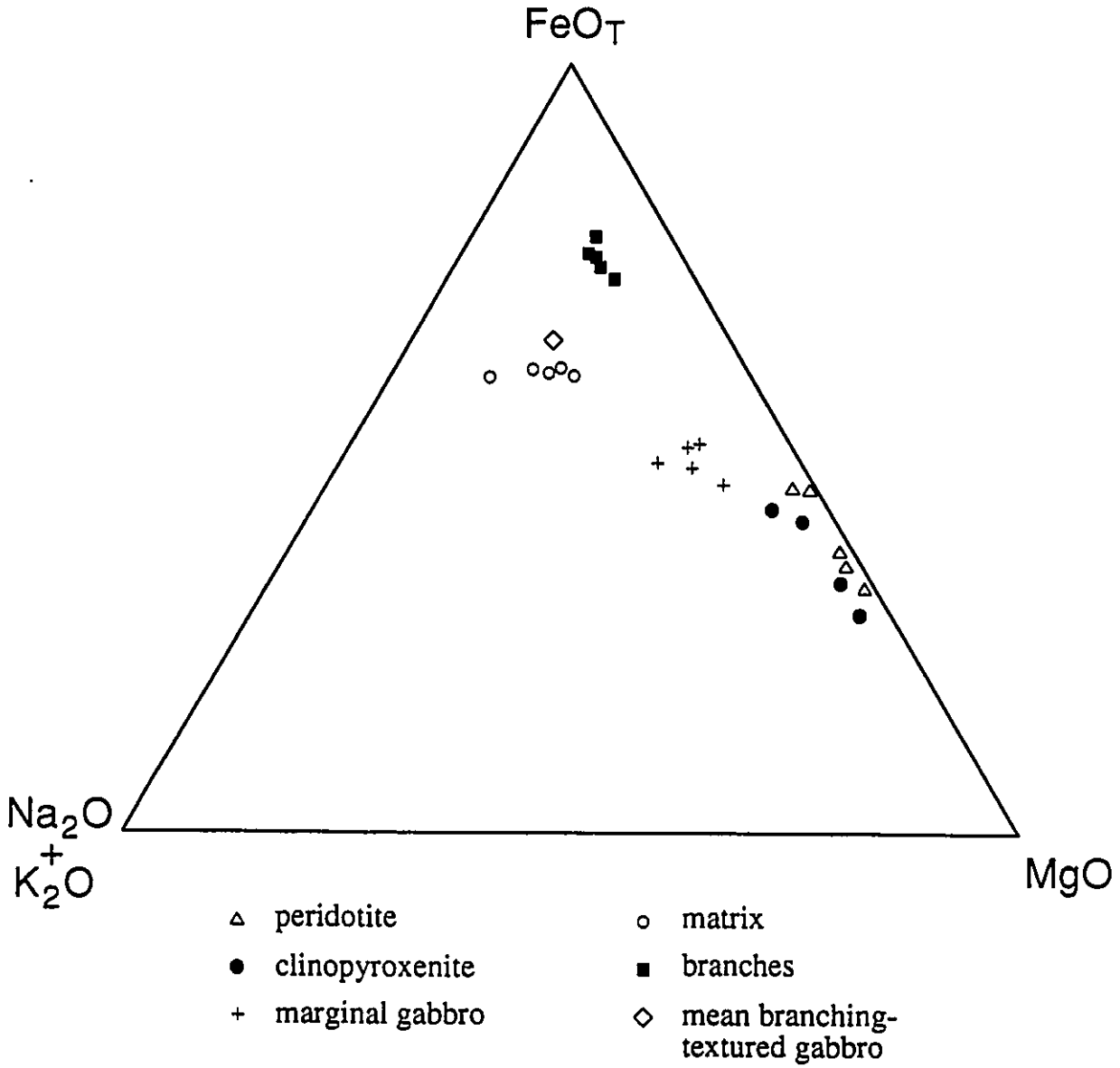

FIGURE 11. AFM diagram showing pattern of variation in rocks of the Centre Hill complex. Mean composition of branching-textured gabbro determined using a matrix/branch ratio of 8/2.
$FeO_T = FeO + 0.8998\ Fe_2O_3$

units in the Muskox intrusion (Irvine, 1980), the Stillwater complex (Raedeke and McCallum, 1984), the Rhum layered intrusion (Emeleus, 1987, Dunham and Wadsworth, 1978), and the Bushveld complex (Irvine, 1982). Several other interpretations which reject the magma replenishment hypothesis have nonetheless been proposed, such as the magma mixing model of Jackson (1961), and the nucleation-diffusion model of McBirney and Noyes (1979). A summary of well-known models which have been advanced to explain the occurrence of cumulate cycles in layered intrusions is presented below.

The Layered Series of the Muskox intrusion has been subdivided into 25 cyclic units interpreted to have formed from separate batches of injected magma (Irvine and Smith, 1967). The displaced residual liquid apparently erupted at the surface to be later eroded away. The modally graded layers found within each cyclic unit are suggested to have formed by a process of double-diffusive fractional crystallization (Irvine, 1980). This process operates directly above the cumulate pile, where the liquid has become stratified into small convective layers which transfer heat and mass by a mechanism of coupled diffusion and convection. Temperature and composition gradients required to initiate convection were established through the injection of high-temperature primitive magma underlying lower-temperature fractionated residual liquid. A similar model was also proposed by Robins (1987) in explaining the origin of repeated layer sequences from the Honningsvag intrusive suite in Norway.

The Eastern Layered Series of the Rhum complex is composed of 16 major units of alternating peridotite and allivalite (i.e. troctolite) interpreted to have crystallized from repeated replenishments of picritic magma (Emeleus, 1987). As suggested for the Muskox intrusion, the injected magma ponded at the base of the chamber under cooler and more evolved residual magma. However, subsequent convection is interpreted to have operated throughout the chamber as a large single cell (Huppert and Sparks, 1980). In this model, strong convection was caused by a reduction in density of the picritic magma due to abundant olivine crystallization. Once the two magmas had mixed, feldspar joined olivine on the liquidus, leading to the formation of allivalite until a new batch of primitive magma was injected. The light residual liquid was then displaced towards the top and a new cycle was started.

Jackson (1961) proposed a very different model for the origin of stratigraphic cycles in the Peridotite Member of the Stillwater complex, suggesting that the system was closed to any influx of magma. His interpretation was based on the gradual progression in chemical composition observed from cycle to cycle, as the magma evolved towards more felsic compositions. Jackson suggested that normal fractional crystallization within a stagnant bottom layer was periodically interrupted by episodes of convective overturn of the entire magma. Thorough mixing of the bottom fractionated magma with the overlying primitive liquid would have caused reinstatement of olivine crystallization.

Cyclic layering in the Skaergaard intrusion has been proposed by McBirney and Noyes (1979) to result from oscillatory nucleation events governed by the relative diffusion rates of heat and matter during cooling. The coupled nucleation/diffusion process operated within a slightly undercooled bottom boundary layer, leading to in situ crystallization. The model is based on the concept that crystallization of phase A creates a zone around the crystal which is enriched in components of phase B, causing saturation and promoting its nucleation. Investigation of cyclic layering in the Skaergaard and Rhum intrusions has led Maaloe (1978) to envisage a similar in situ fractionation process.

Cyclic layering in the Centre Hill complex has been interpreted in terms of periodic injection of basaltic magma to the chamber, with concomitant evacuation of the differentiated residual liquid (MacRae, 1965). In the following model, it is proposed that the contrasting cyclic units found within the ultramafic zone and the upper gabbro layer are genetically related, originating from episodes of magma replenishment associated with periodic convection in the chamber.

5.3.2 Cyclic layering in the Centre Hill complex

Layers of the Centre Hill complex have been subdivided into seven units: five basal units composed of cyclic successions of peridotite and clinopyroxenite; a sixth unit of peridotite, clinopyroxenite, and gabbro; and an upper unit consisting of melagabbro grading upward into gabbro. This uppermost layer of

gabbro is characterized by alternating bands of BTG and CTG found near the top of the layer (banded zone). Thus there are two distinct occurrences of cyclic layering in the Centre Hill complex: 1) cyclic units of peridotite and clinopyroxenite; and 2) cyclic units of BTG and CTG.

Two different models are postulated for the petrogenesis of the Centre Hill complex (model 1, Figure 12; model 2, Figure 13). As both models differ only by the appearance of the branching olivine crystals in the paragenetic sequence, reference to model 1 alone will be made in explaining the occurrence of cyclic layering (Figure 12a to 12d). The second model will be discussed separately later in the chapter. For simplicity, only two cyclic events of crystallization are illustrated in the schematic diagrams. The stratigraphic thickness of layers is also greatly exaggerated.

5.3.2.1 Peridotite-clinopyroxenite cycles

The peridotite-clinopyroxenite cycles in the lower half of the intrusion are interpreted to have formed by normal fractional crystallization of the magma, which was periodically interrupted by episodes of magma replenishment. The cumulus mineral successions seemingly formed by accumulation of gravitationally settled crystals that presumably grew near the roof of the chamber, where heat loss was maximized.

Each cycle initiated with the crystallization of olivine upon cooling to the liquidus temperature. The primocrysts settled

FIGURE 12. Schematic diagram of model 1 illustrating the formation of paired cyclic units and the appearance of branching olivine crystals in the Centre Hill complex. Filled circles represent olivine, open circles represent clinopyroxene, hachured circles represent Ca-poor pyroxene, and straight lines represent plagioclase.

A. Olivine and clinopyroxene crystallize under the roof of the chamber, and sink towards the bottom at different settling velocities. Fine-grained gabbro (MGB) crystallizes along the upper margin of the sill.

B. With further cooling, olivine is replaced by Ca-poor pyroxene (not observed) as a cumulus phase. Clinopyroxene crystals accumulate at the bottom to form a layer of clinopyroxenite (CP), directly overlying the layer of peridotite (PD). Clinopyroxene and plagioclase crystallize in situ along the roof, forming a band of incipient branching-textured gabbro (BTG).

C. Abundant crystallization of plagioclase occurs near the top of the magma chamber, and crystals migrate upwards by flotation to form a band of clotted-textured gabbro (CTG). Clinopyroxene and Ca-poor pyroxene continue to form under the roof and settle towards the bottom. In situ crystallization of clinopyroxene and Ca-poor pyroxene also occurs within the band of CTG.

D. A new batch of magma is injected into the chamber, mixing with the residual differentiated liquid. The hybrid melt is then largely displaced out of the chamber. The band of CTG is partly eroded due to the convecting magma.

E. Periodic replenishment of magma to the chamber leads to the formation of other paired cyclic units, which develop as illustrated in diagrams A to D. Only two cyclic events are shown for simplicity. The lower portion of the upper layer of gabbro (GB) is the last part of the complex to crystallize. It dominantly consists of clinopyroxene, Ca-poor pyroxene, and plagioclase. The fractionated residual liquid forms a sandwich horizon, occurring where the roof and floor of the sill converge.

F. The final portion of differentiated liquid migrates upward through the roof rocks (i.e. the banded zone). It crystallizes branching olivine crystals within the bands of BTG. The branching crystals grow directly away from the upper contact.

MODEL 1

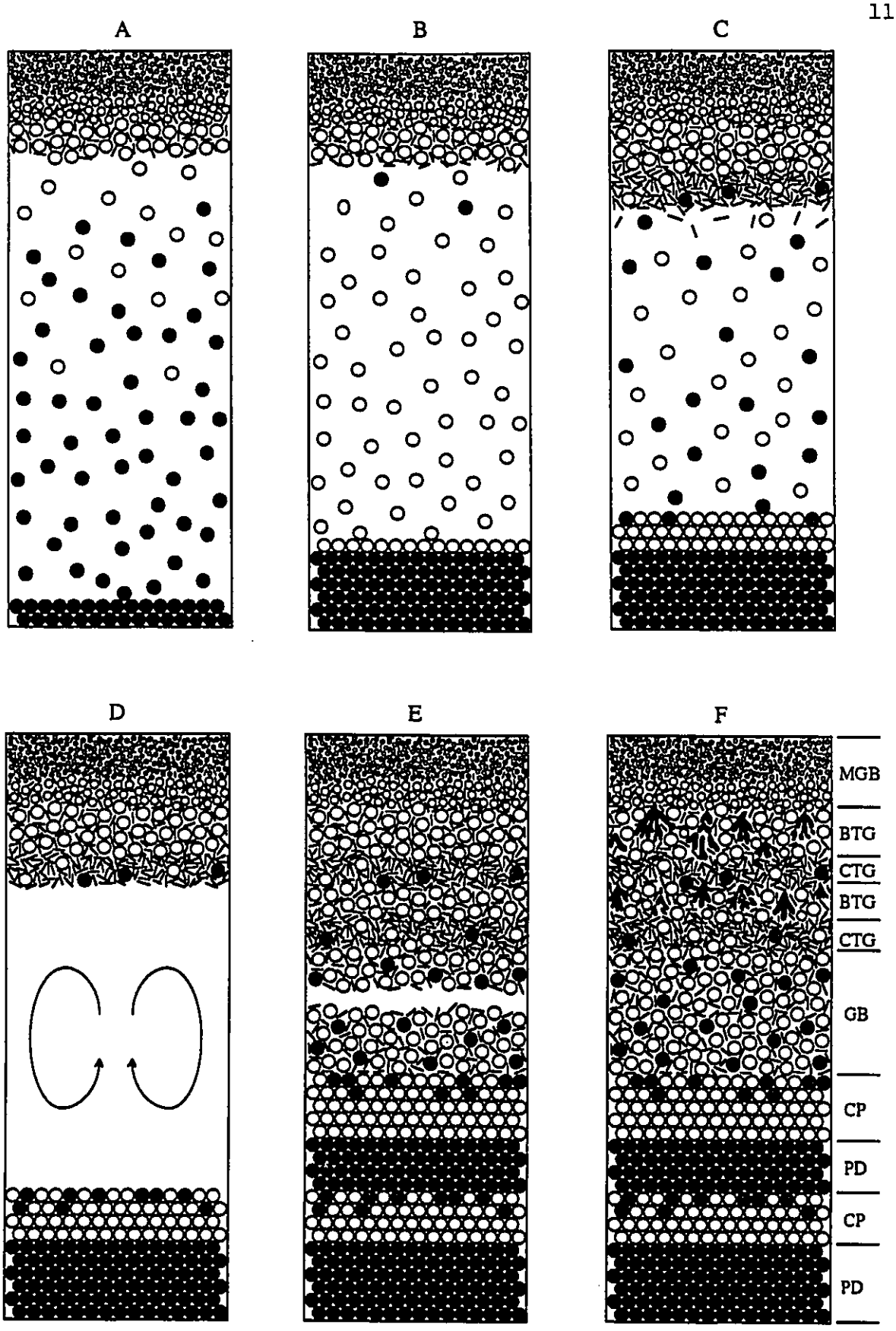

FIGURE 13. Schematic diagram of model 2 illustrating the formation of paired cyclic units and the appearance of branching olivine crystals in the Centre Hill complex. Symbols are the same as in Figure 9.

A. As in model 1, olivine and clinopyroxene crystallize under the roof of the chamber, and sink towards the bottom at different settling velocities. Fine-grained gabbro (MGB) crystallizes along the upper margin of the sill.

B. As in model 1, olivine is replaced by Ca-poor pyroxene (not observed) with further cooling. Clinopyroxene crystals accumulate at the bottom to form a layer of clinopyroxenite (CP), directly overlying the layer of peridotite (PD). Clinopyroxene and plagioclase crystallize in situ along the roof, forming a band of incipient branching-textured gabbro (BTG).

C. As in model 1, abundant crystallization of plagioclase occurs near the top of the magma chamber, and crystals migrate upwards by flotation to form a band of clotted-textured gabbro (CTG). Clinopyroxene and Ca-poor pyroxene continue to form under the roof and settle towards the bottom. In situ crystallization of clinopyroxene and Ca-poor pyroxene also occurs within the band of CTG.

D. A new batch of magma is injected into the chamber, mixing with the residual differentiated liquid. The hybrid melt is then largely displaced out of the chamber. The band of CTG is partly eroded due to the convecting magma. Large branching olivine crystals grow from the stagnant interstitial liquid within the band of BTG, extending directly away from the upper contact.

E. Periodic replenishment of magma to the chamber leads to the formation of other paired cyclic units, which develop as illustrated in diagrams A to D. The branching olivine crystals form at the end of each cyclic event from the interstitial melt present in bands of BTG.

F. The lower portion of the upper layer of gabbro (GB) is the last part of the complex to crystallize. The final portion of differentiated liquid crystallizes where the roof and floor of the sill converge (i.e. sandwich horizon).

MODEL 2

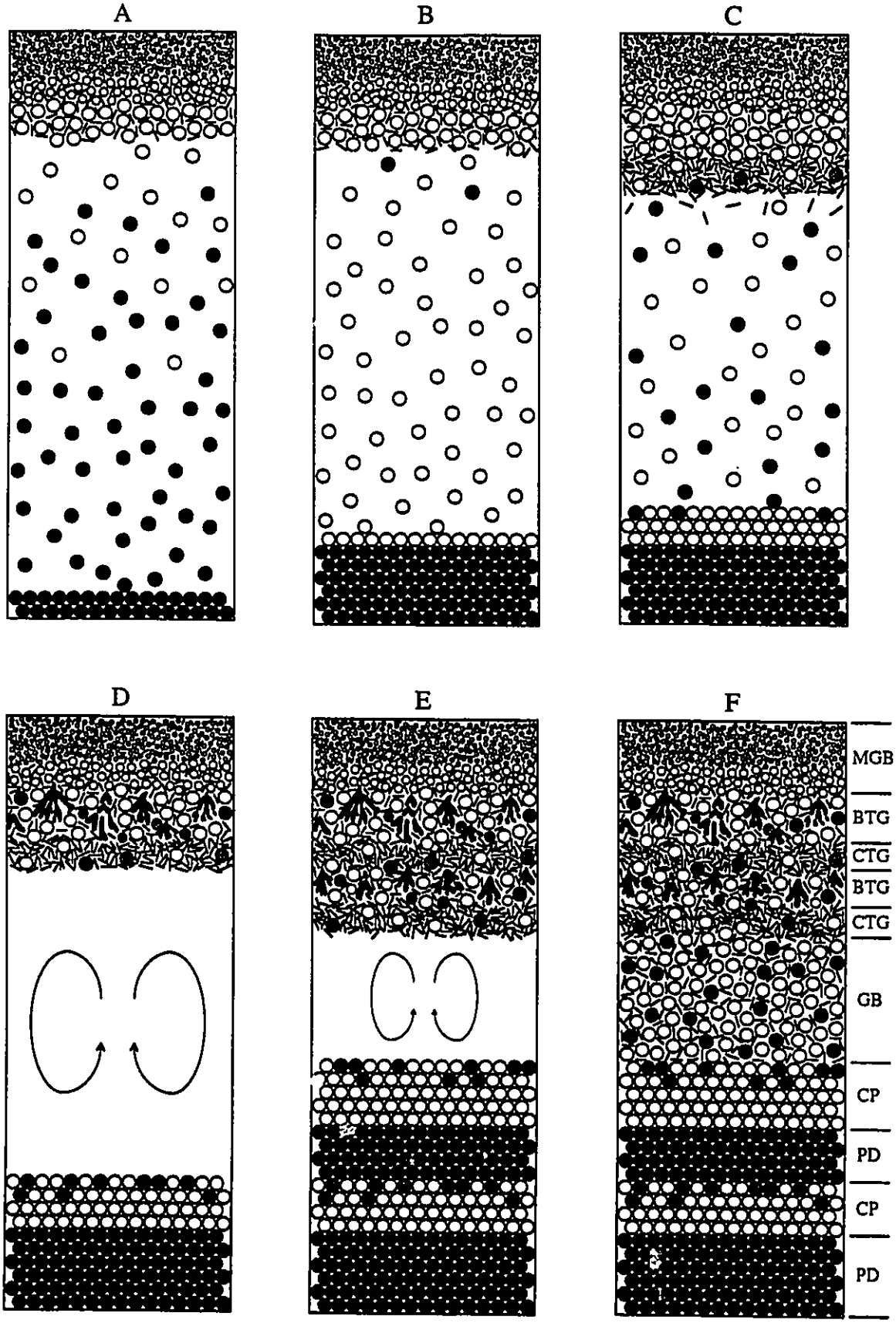

at the bottom to form an homogeneous layer of olivine cumulates. With further cooling, clinopyroxene joined olivine on the liquidus, leading to the simultaneous precipitation and sinking of both phases (Figure 12a). The notable absence of plagioclase cumulates within the layers of peridotite and clinopyroxenite is discussed below.

With further fractionation, Ca-poor pyroxene likely replaced olivine as a liquidus phase with clinopyroxene (Figure 12b). This olivine/Ca-poor pyroxene relationship, which is typical of layered mafic intrusions, is dependent on the a_{SiO2} of the melt (Campbell and Nolan, 1974). It will be referred to later in explaining the appearance of the branching olivine crystals.

As illustrated in Figure 12b, there is an abrupt change in cumulus mineralogy from a clinopyroxene-free peridotite to an olivine-depleted clinopyroxenite, which is likely related to differences in the settling velocity of the accumulating phases. The settling rate of crystals, which is a function of specific gravity and grain size, was determined from cumulus grains of olivine and clinopyroxene using Stoke's Law.

The density of an olivine grain analyzed from the top of layer #9 (sample Pd-5) was evaluated at 3.50 g/cm^3, while a clinopyroxene crystal from the base of the overlying clinopyroxenite layer (sample Cp-5) yielded a density of 3.28 g/cm^3. The difference in density is explained by the lower Mg number of olivine (0.71) relative to clinopyroxene (0.82), as the former preferentially incorporates iron in its crystal lattice. The

average grain size of olivine and clinopyroxene was approximated at 1.8 mm^3 and 1.5 mm^3 respectively. Based on density and grain size, it is evident that crystals of olivine settled at a faster rate than crystals of clinopyroxene. The density of the basaltic liquid at 1200°C was evaluated at 2.68 g/cm^3 using data of Bottinga and Weill (1970). The melt viscosity was set at 170 poises based on data by Kushiro et al.(1976). The Centre Hill primary magma composition used in the calculations was determined by MacRae (1965).

From the above figures, it is estimated that crystals of olivine and clinopyroxene settled at rates of 51.1 cm/day and 33.5 cm/day respectively. Based on this simple analysis, it would have taken 26 and 39 months for crystals of olivine and clinopyroxene respectively to sink from the top of the chamber to the bottom in the earliest stages of crystal accumulation. Such sinking velocities are similar to those determined by Maaloe (1978) on settled olivine primocrysts of the Skaergaard intrusion. It is therefore conceivable that the abrupt change in cumulus mineralogy originates from a process of gravitational separation, considering that the settling velocity of olivine crystals is 50% greater than it is for clinopyroxene. It has been shown experimentally by Campbell et al. (1978) that excellent gravitational crystal sorting can be achieved through a stagnant layer of magma.

Although cumulus plagioclase is absent from layers of peridotite and clinopyroxenite, it nonetheless did crystallize

during fractionation. Estimation of plagioclase density at magmatic temperatures reveals that plagioclase was likely buoyant in the coexisting liquid. Using extrapolated data of Kozu and Ueda (1933), the density of plagioclase (An_{60}) at 1200°C has been evaluated at 2.64 g/cm^3 (Campbell et al., 1978). These calculations show that plagioclase crystals were 0.04 g/cm^3 less dense than the coexisting liquid, which clearly demonstrates their tendency not to sink and perhaps to float (Figure 12c).

Crystals of olivine and clinopyroxene that accumulated at the bottom of the magma chamber were evidently surrounded by intercumulus liquid. Upon further cooling, this interstitial melt solidified, accounting for the formation of large poikilitic crystals of clinopyroxene within the layers of peridotite. Similarly, clinopyroxene and plagioclase crystallized from the residual melt within the layers of clinopyroxenite. These intercumulus crystals were later intensely altered to an assemblage of actinolite and chlorite.

Gravitational settling of olivine and clinopyroxene crystals on the floor of the chamber was likely associated with concomitant crystallization of fine-grained gabbro along the upper margin of the intrusion (Figure 12a). As shown by the petrographic study (Plates 21 to 24), the skeletal to acicular crystal morphologies of plagioclase and clinopyroxene within the marginal gabbro suggest crystallization from the margin inwards under relatively high rates of cooling. Approximately 20 m of fine-grained gabbro (i.e. marginal gabbro) formed during this

first episode of crystallization. The associated peridotite-clinopyroxenite unit present at the base of the sill measures 49 m in thickness.

Based on variations in the thickness of peridotite and clinopyroxenite layers, it is interpreted that each of the seven units of the Centre Hill complex formed from separate batches of tholeiitic magma periodically injected to the chamber (Figure 12d). As illustrated in Figure 4, the thickness of peridotite layers gradually decreases up-section from 70 m to 1 m, whereas the thickness of clinopyroxenite layers is highly variable. The decreasing thickness of peridotite layers implies that each pulse of magma, upon mixing with the residual melt, became gradually more felsic in composition. The crystallization of cumulus olivine was thus generally less abundant with each new pulse of magma, as the liquidus temperature of clinopyroxene was reached at an earlier stage. The fact that the third layer of peridotite (layer #5) is slightly thicker than the underlying peridotite remains enigmatic. However, this anomaly may be due to lateral changes in layer thickness, which were not investigated in this study. The random variation in the thickness of clinopyroxenite layers is explained by the random timing of magma injection, with thicker layers corresponding to longer time intervals between pulses.

Whole rock data gathered from several peridotite and clinopyroxenite layers reveal a gradual evolution in layer composition from the second peridotite-clinopyroxenite cyclic unit (cycle #2)

to the uppermost cyclic unit (cycle #5). Peridotite samples collected near the top of layers 3, 5, 7 and 9 (Figure 4) show a gradual decrease in Mg number from 0.62 to 0.51, whereas clinopyroxenite samples from layers 4, 8 and 10 have a ratio that decreases from 0.68 to 0.53 (Figure 8). Such systematic variations in chemical composition supports the assumption that each new batch of injected magma partly mixed with the more evolved residual melt, yielding an hybrid magma having a more felsic bulk composition than the primitive liquid. Alternative hypotheses that may account for the upward chemical evolution between cycles are: 1) the injected batches of magma were derived from a larger reservoir that was itself undergoing fractional crystallization (Morse, 1980); and 2) the underlying reservoir of magma was being contaminated by partial melting of the sialic crust.

It is interpreted that the injection of each new batch of magma to the chamber largely displaced the residual differentiated liquid out of the chamber. The expulsion of resident magma at the surface is supported by the field observations of Johnstone (1987), who reported the presence of a tholeiitic layered flow that possibly extruded from the westernmost end of the Munro Sill, approximately 5 km to the south-west of Centre Hill. According to Robins (1987), the injection of new magma may alternatively result in an increase in the volume of the chamber. Displacement and inflation may also occur in combination.

In summary, each cyclic unit of peridotite and clinopyroxenite crystallized from periodically injected batches of magma

to the chamber. Each new pulse of magma likely mixed with the resident melt, explaining the gradual upward evolution towards more felsic compositions. The well developed segregation between fractionated crystals of olivine and clinopyroxene is explained by differences in their settling rates, which is a function of the specific gravity and size of the crystals.

5.3.2.2 Branching- and clotted-textured gabbro cycles

Despite intense weathering of the outcrop surface which partly obscures band contacts, it is nonetheless considered that between five and seven cyclic units of branching- and clotted-textured gabbro occur within the upper gabbro layer of the Centre Hill complex. The entire succession, referred as the banded zone, is approximately 70 m in thickness and directly underlies the marginal gabbro along the western portion of the hill (Figure 3).

It is suggested that each cyclic unit of BTG and CTG formed concurrently with a cyclic unit of peridotite and clinopyroxenite (Figure 12a to 12d). According to the model, each pair of cyclic units is genetically related, having crystallized from the same pulse of magma. Based on field observations, each episode of magma replenishment was associated with magma mixing and convection, leading to the partial erosion of newly formed bands of CTG (Figure 12d).

Each cyclic unit of the banded zone initiated with the crystallization of significant proportions of clinopyroxene and plagioclase to form a band of incipient BTG. Crystallization

proceeded from the roof towards the centre of the intrusion along a temperature gradient (Figure 12a and 12b). The growth of branching olivine crystals took place afterwards, their appearance being discussed hereafter.

The transition from a band of BTG to an underlying band of CTG is gradational over a few tens of centimetres. While bands of BTG are on average approximately 10 m thick, those containing clots reach a maximum of only one metre. The difference in band thickness may be explained by the injection of new batches of magma to the chamber, which promoted convection and subsequent erosion of the bottom of bands of CTG. Such interpretation is supported by the sharp nature of the contact between both types of bands at the start of a new cycle. It is also possible that certain bands of CTG have been entirely eroded away, as they were less frequently encountered than bands of BTG.

Further evidence supporting the presence of current action within the Centre Hill complex is given by prominent igneous lamination found in the layer of melagabbro. The lamination is defined by the preferred orientation of plagioclase laths parallel to the layering. Moreover, cross-laminations within the upper gabbro layer of the Munro-Warden complex have been reported by MacRae (1965), while Johnstone (1987) pointed out from the same locality the presence of interfingered layers of peridotite and clinopyroxenite, as well as scoured and fragmented cumulate layers.

Bands of branching- and clotted-textured gabbro are also

distinct in terms of the modal composition of their matrices. Plagioclase averages about 50 vol.% in the matrix of BTG, while reaching between 60 and 75 vol.% in the matrix of CTG (Plate 16). Hence the rock surrounding the clots is considered to have a leucogabbro composition.

A significant proportion of plagioclase crystals found within the bands of CTG likely crystallized slightly under the roof of the chamber, migrating upwards by flotation and accumulating beneath bands of BTG (Figure 12c). Assuming that plagioclase crystals were effectively 0.04 g/cm^3 less dense than the surrounding liquid, the crystals would have migrated upwards at a rate of approximately 2.5 cm/day, thus taking over 6 months to float over a distance of 5 m. This interpretation is further supported by the contrasting petrographic features of plagioclase crystals observed within both types of bands, namely in terms of: 1) modal abundance; 2) crystal size; and 3) mineral texture.

As previously stated, the modal abundance of plagioclase is significantly greater within the bands of CTG. While plagioclase crystals grew in situ in the bands of BTG, they rose through the magma and agglomerated together to form the bands of CTG, explaining their higher concentration.

The size of plagioclase crystals is also quite different between bands of BTG and CTG. They range from 1 to 3 mm in length in the former, and average as much as 5 mm in the bands of CTG. It is assumed that significant growth took place during the ascension of the crystals through the magma, explaining the

contrast in grain size. No evidence of zoning was detected, which rejects the hypothesis of in-situ orthocumulus growth from the trapped liquid.

Significant disparities were noted in the mineral texture of both rock types. In the bands of BTG, crystals of plagioclase and clinopyroxene are intergrown and display a typical sub-ophitic texture. Both minerals grew simultaneously, partly enclosing each other. In contrast, clinopyroxene occurs almost entirely as an interstitial phase to plagioclase in the bands of CTG, suggesting late crystallization from the intercumulus liquid. Plagioclase laths have been partly recrystallized along their margins, as evidenced by their jagged grain boundaries. Such a feature also supports an origin whereby the crystals would have been transported in the magma following their formation. The significant amount of secondary interstitial minerals such as fine-grained actinolite and epidote suggests that plagioclase may also have crystallized from the intercumulus liquid and be later completely altered.

Aggregates of fine-grained actinolite, occurring as irregular interstitial patches and discrete grains, are likely secondary after Ca-poor pyroxene, the latter seemingly fractionating as bands of CTG were being formed (Figure 12c).

In summary, contrasting textural and mineralogical features found within the matrices of BTG and CTG reveal that the former bands apparently developed by in-situ crystallization, whereas the bands of CTG possibly formed by accumulation of buoyant

crystals of plagioclase along the roof of the chamber. Each cyclic unit of BTG and CTG may be genetically related to a cyclic unit of peridotite and clinopyroxenite, implying that both cycles crystallized from the same pulse of magma.

5.4 APPEARANCE OF BRANCHING OLIVINE CRYSTALS

Based on petrographic and geochemical evidence, it is undeniable that the reddish-coloured branching forms exposed within the BTG were originally large individual crystals of olivine that have been replaced by an assemblage of secondary minerals. Preserved textures indicate that the branching olivine crystals grew within a crystal-liquid mush during the later stages of fractionation. This interpretation is supported by: 1) the presence of abundant crystals of plagioclase and clinopyroxene enclosed within the branches; 2) the strong textural and compositional similarities between the enclosed minerals and those of the surrounding matrix; and 3) the common reappearance of Fe-rich olivine as a liquidus phase in many layered mafic intrusions.

As made evident by field and petrographic work, crystals of plagioclase, clinopyroxene and ilmenite that are found enclosed within the branching olivine crystals are texturally and compositionally very much alike those from the matrix portion of the gabbro (Plate 8). Such a similarity undoubtedly implies that the growth of olivine took place within a crystal-liquid mush.

The reappearance of olivine as a liquidus phase towards the

end of fractionation is a feature common to many layered mafic intrusions (Wager and Brown, 1967). The olivine crystals are typically fayalitic in composition as the reduced magma becomes enriched in iron through fractionation. The onset of late stage olivine crystallization is usually associated with a cessation in the formation of Ca-poor pyroxene (Campbell and Nolan, 1974).

Figure 14 shows the relationship between the olivine/Ca-poor pyroxene stability curve (Ol/Opx) and the a_{SiO2} for the Skaergaard liquid. The position of the Ol/Opx curve has been calculated by determining the level of a_{SiO2} at which both phases can coexist, while the quartz line is the level of a_{SiO2} at which quartz becomes a liquidus phase. The other curves represent the a_{SiO2} of the Skaergaard and Jimberlana liquids at different stages of fractionation as estimated by Campbell and Nolan (1974), and an estimate of the fractionation path for the Centre Hill liquid.

In the Skaergaard magma, olivine ceased to crystallize due to the increasing a_{SiO2} of the melt, was then replaced by Ca-poor pyroxene, and later reappeared as a cumulus phase when the rising Ol/Opx stability curve intersected the a_{SiO2} at approximately En_{48}. Note that the a_{SiO2} curve of the Skaergaard liquid never intersects the quartz line, which explains the absence of cumulus quartz in the intrusion. Both the Skaergaard and Bushveld intrusions crystallize cumulus magnetite and fayalite but not cumulus quartz in the later stages of fractionation, as the fractionation trend is towards iron enrichment and silica depletion (Wager and Brown, 1967).

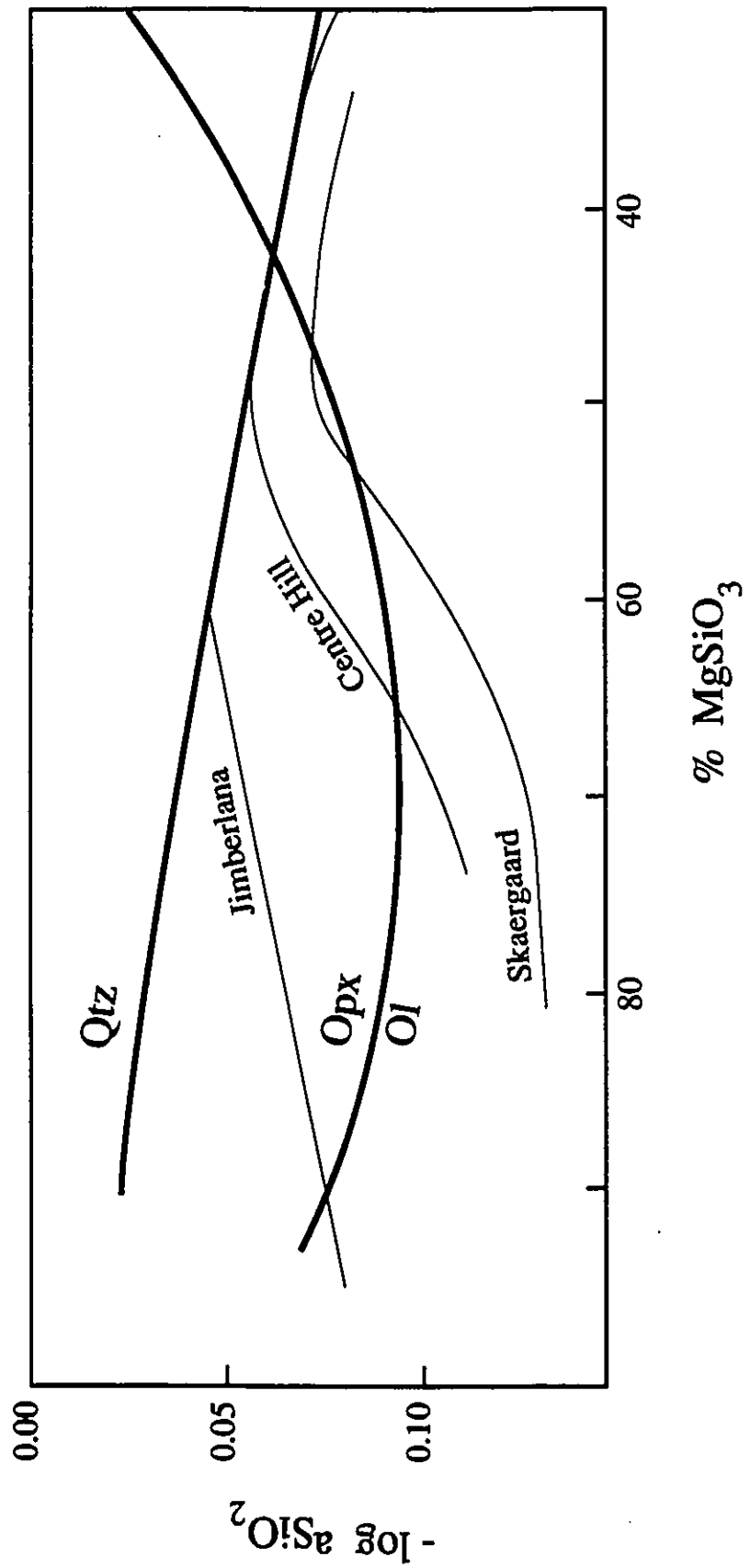

FIGURE 14. Stability of olivine (Ol), Ca-poor pyroxene (Opx), and quartz (Qtz) relative to the a_{SiO_2} in the Skaergaard liquid. An estimate of the a_{SiO_2} of the Skaergaard, Jimberlana, and Centre Hill liquids is given at different stages of fractionation (modified after Campbell and Nolan, 1974).

In contrast, the fractionation of the Jimberlana intrusion follows a silica enrichment/iron depletion trend typical of oxidized magmas, crystallizing cumulus quartz but little or no magnetite towards the end of fractionation. Furthermore, Ca-poor pyroxene is not replaced by Fe-rich olivine as the melt never reaches a high enough level of a_{FeO} (Campbell, 1977). A similar process has been invoked for the Sudbury complex (Campbell and Nolan, 1974).

The Centre Hill magma is interpreted to have fractionated following a silica enrichment/iron enrichment trend, as both cumulus quartz and magnetite crystallized during the final stages of fractionation. The silica enrichment trend was sufficiently strong to saturate the magma in SiO_2 before Fe-rich olivine reappeared as a cumulus phase. According to Figure 14, the initial magma had a low a_{SiO2} and magnesium-rich olivine crystallized. Olivine was eventually replaced by Ca-poor pyroxene as the a_{SiO2} liquid curve rose to intersect the Ol/Opx stability curve. Continued crystallization of Ca-poor pyroxene was accompanied by a gradual increase in the a_{SiO2} of the melt. The a_{SiO2} liquid curve remained above the Ol/Opx curve until it intersected the quartz line. Cumulus quartz then started to crystallize along with Ca-poor pyroxene, and the a_{SiO2} liquid curve migrated along the quartz line until it intersected with the Ol/Opx curve. At that particular point, Ca-poor pyroxene became unstable and was replaced by Fe-rich olivine. Quartz and Fe-rich olivine coexisted as the a_{SiO2} liquid curve migrated along the quartz line until the

final portion of liquid was consumed. This would explain the extreme fayalitic composition of the Fe-rich olivine (~Fa_{95}). Other layered mafic bodies such as the Palisades sill (Walker, 1969) and the Muskox intrusion (Irvine, 1980) follow the same fractionation trend, crystallizing quartz before the reappearance of Fe-rich olivine as a cumulus phase.

The order of appearance of the cumulus minerals separating from the Centre Hill liquid appear to have been as follow: olivine/clinopyroxene/plagioclase/Ca-poor pyroxene/magnetite/-quartz/fayalite. In order to explain the sharpness of contacts between adjacent layers of peridotite (free of cumulus clino-pyroxene) and clinopyroxenite (free of cumulus olivine) in the bottom ultramafic zone, it is suggested that Mg-rich olivine ceased to crystallize in the later stages of each cyclic episode, hence that Ca-poor pyroxene joined clinopyroxene and plagioclase as a liquidus phase. Fractionation of Ca-poor pyroxene is interpreted to have occurred in both the upper portion of clinopyroxenite layers, and in the bands of CTG (Figure 12c). Even though Ca-poor pyroxene was not observed in these two rock types, it is suggested that the high proportion of fibrous patches of actinolite in the bands of CTG, and locally of interstitial chlorite-actinolite aggregates in layers of clinopyroxenite, may represent its alteration products.

As described previously in chapter 3, the lower to middle part of the upper layer of gabbro contains abundant granophyric intergrowths of quartz and feldspar. This zone is interpreted as

a region in which the fractionated residual liquid crystallized, and is represented in Figure 12e by the remaining liquid fraction. The granophyric zone of layered intrusions is often referred as the sandwich horizon, as it occurs where the roof and floor of the sill converge (Wager and Brown, 1967, Shirley, 1987). The fact that Fe-rich olivine crystallized in the overlying banded zone (i.e in bands of BTG) rather than in the granophyre-rich zone is of significant importance. As shown in Figure 14, quartz and Fe-rich olivine are expected to coexist during crystallization of the final melt fraction at Centre Hill. Based on such evidence, it is postulated in model 1 (Figure 12e and 12f) that the branching olivine crystals crystallized from the upward migration of the last differentiated liquid through the roof area. Irvine (1980) proposed that intercumulus liquid filtered upward in the Muskox intrusion for distances of at least 100 m and perhaps as much as 300 m, which is well within the range postulated for the migration of the Centre Hill residual liquid. The presence of cumulus quartz and granophyric intergrowths in the banded zone, although much less abundant than in the lower part of the upper gabbro, suggest that quartz and Fe-rich olivine both crystallized from the migrated residual liquid, at an Fe/Mg ratio where Ca-poor pyroxene had already ceased to precipitate. According to the mineral stability curves of figure 14, the appearance of cumulus quartz in the lower part of the upper layer of gabbro must have coexisted with Ca-poor pyroxene, since crystallization of Fe-rich olivine apparently did not take

place. Hence according to model 1 (Figure 12f), Ca-poor pyroxene crystallized throughout the lower portion of the upper layer of gabbro, but did not form in the bands of BTG, owing to the presence of Fe-rich olivine. The very low proportion of Fe-rich olivine in bands of CTG is discussed in the following chapter.

An alternative hypothesis explaining the appearance of branching olivine crystals in bands of BTG is illustrated in model 2 (Figure 13). As shown by Figure 13d and 13e, the crystallization of Fe-rich olivine would have taken place at the end of each cyclic episode, hence not only from the residual liquid of the last injected batch of magma. Furthermore, Ca-poor pyroxene would have precipitated within the bands of BTG, which also contradicts model 1. This second hypothesis is based on the assumption that interstitial liquid trapped within bands of BTG underwent in situ fractional crystallization in the later stages of each cycle. According to Figure 14, such a scenario could have led to the precipitation of Ca-poor pyroxene, quartz, and ultimately Fe-rich olivine through increasing fractionation. In addition, it is possible that the branching olivine crystals crystallized from the trapped Fe-rich liquid only following the magma replenishment event, hence in the early stage of each new cycle. The injection of fresh magma potentially could have sent a rapid pulse of heat to the incipient BTG, momentarily halting crystallization of the trapped liquid. Rapid diffusion of heat through the band of BTG would then lead to conditions of higher undercooling, hence relatively rapid growth in a stagnant liquid.

This model would explain the very low proportion of Fe-rich olivine and quartz in the bands of CTG. However, that Ca-poor pyroxene crystallized in bands of BTG remains doubtful. Although interstitial patches of fine-grained actinolite are present, they are less common than elsewhere in the upper layer of gabbro. Furthermore, the reaction equation determined in Chapter 3 for the alteration of Fe-rich olivine was balanced without the use of Ca-poor pyroxene as a reactant. A reaction equation that included Ca-poor pyroxene could not be balanced.

CHAPTER 6

ORIGIN OF BRANCHING OLIVINE CRYSTALS

6.1 INTRODUCTION

Branching morphologies such as those observed within the upper gabbro layer of the Centre Hill Complex are normally restricted to rocks that have been subjected to very fast cooling regimes (i.e. volcanic rocks). Although similar disequilibrium textures have been reported from other mafic intrusions (Wager and Brown, 1951, Taubeneck and Poldervaart, 1960, Robins, 1973, and Donaldson, 1974), their occurrence as very large, "tree-like" crystals within an otherwise fine- to medium-grained rock is clearly remarkable. The purpose of this chapter is thus to interpret the origin of the branching olivine crystals, by considering particular melt properties that may have controlled nucleation and crystal growth kinetics.

The branching morphologies observed on the outcrop surface have been duplicated on the computer using a modified version of the diffusion limited aggregation (DLA) algorithm of Witten and Sander (1981). The DLA algorithm allowed the growth of the branching crystals to be experimentally simulated, showing that diffusion was likely the main growth-controlling factor in the formation of these textures. Prior to carrying out the DLA experiments, the fractal dimensions of several branching crystals

were measured to ensure that the simulated textures were morphologically and statistically similar to those observed in the rock. Hence a review on the concept of fractal geometry along with results are presented below.

6.2 FRACTAL GEOMETRY

6.2.1 Introduction

The concept of fractal geometry was pioneered by Benoit Mandelbrot during the 1960's, after he discovered certain laws governing the formation of "random" and irregular mathematical constructs and patterns found in nature. Mandelbrot is the true inventor of the word "fractal", which comes from the latin words "fractus" (irregular) and "frangere" (to break into irregular fragments) (Mandelbrot, 1982).

Fractals are defined as shapes that are self-similar across scale, implying that the degree of irregularity or fragmentation is roughly identical at all scales. They can also be referred as being composed of parts similar to the object itself. Alternatively, a fractal is also defined as a set for which the Hausdorff-Besicovitch dimension, or fractal dimension (D_F), strictly exceeds the topological dimension (D_T) (Mandelbrot, 1982). The topological dimension applies to Euclidean objects and is always an integer: a point has a D_T equal to zero, a line is equal to one, a square or circle, to two, and a cube or sphere is a three-dimensional object. A fractal dimension can be represented by a fraction, and is therefore not restricted to be an

integer value.

There are several ways of calculating the fractal dimension of an object. A good method to help understand the concept is to consider Euclidean structures, for which D_F and D_T are the same. In Figure 15a, a straight line of length 1 is divided into N= b subintervals of length r= 1/b. Setting b equal to 4, the fractal dimension is given by:

$$D_F = \frac{\text{LOG N}}{\text{LOG 1/r}} = \frac{\text{LOG 4}}{\text{LOG 4}} = 1$$

The same procedure is applied in calculating the fractal dimension of a square having sides of length 1 (Figure 15b). Here, the surface is divided into N= b^2 squares of side r=1/b. Given b=4, the fractal dimension is:

$$D_F = \frac{\text{LOG N}}{\text{LOG 1/r}} = \frac{\text{LOG 16}}{\text{LOG 4}} = 2$$

The Triadic Koch Curve has become the paradigm of a compact object having a fractal perimeter with a D_F between one and two (Figure 16) (Mandelbrot, 1982). It is constructed from an equilateral triangle with sides of length 1, where each of the three straight intervals is referred as an initiator. The middle third portion of each initiator is replaced by a smaller equilateral triangle with sides of length 1/3. The structure now consists of three broken lines, termed generators, of shape _/_ and each composed of four segments of length 1/3. Triangles with

A.

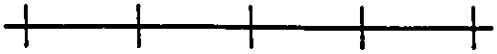

N = b parts of length $r = 1/b$

$$D_F = \frac{\log N}{\log 1/r} = \frac{\log 4}{\log 4} = 1$$

B.

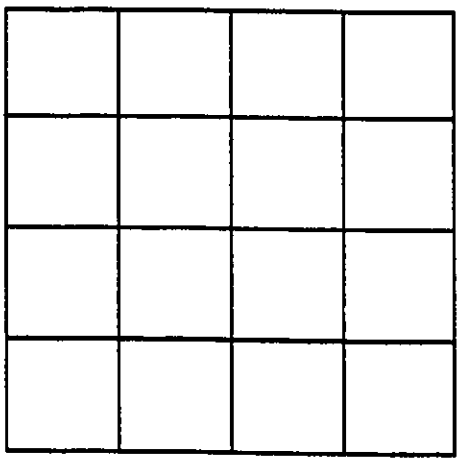

$N = b^2$ parts of side $r = 1/b$

$$D_F = \frac{\log N}{\log 1/r} = \frac{\log 16}{\log 4} = 2$$

FIGURE 15. a) Straight line divided into 4 subintervals of equal length. $D_F = D_T = 1$.
b) Square area divided into 16 squares of equal size. $D_F = D_T = 2$.

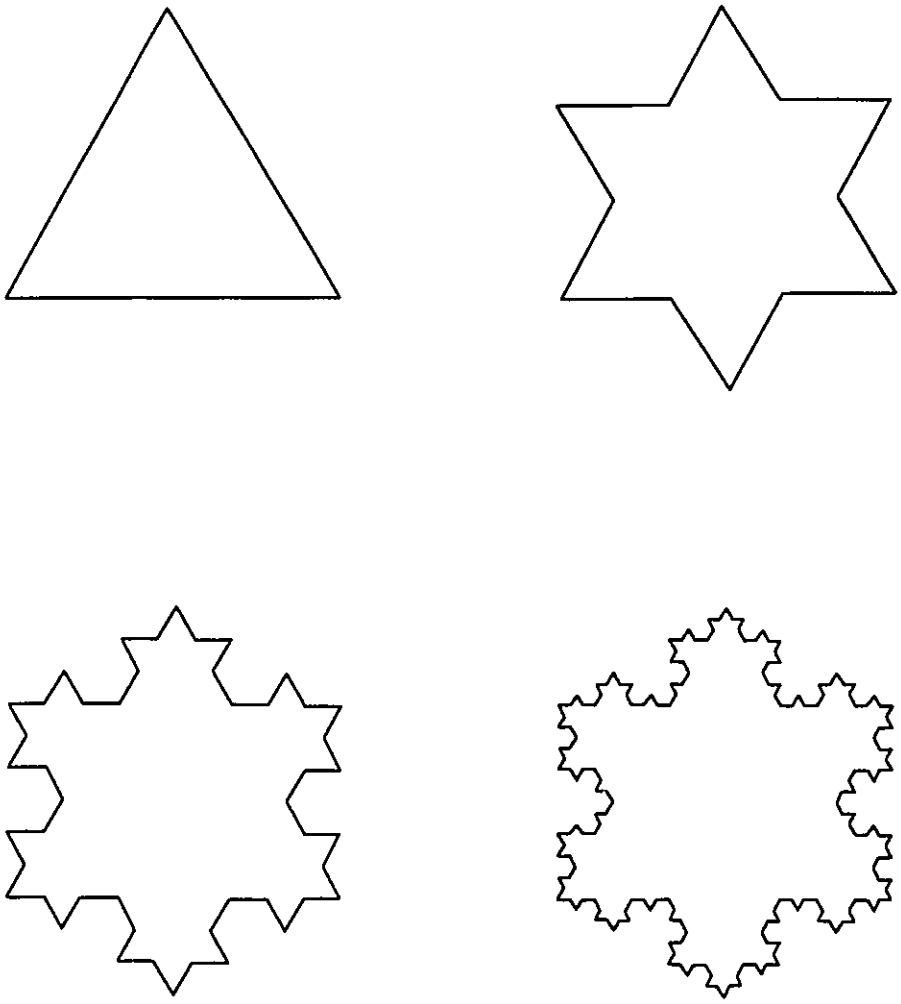

FIGURE 16. Construction of the triadic Koch Curve by recursively replacing the middle portion of each straight line by an equilateral triangle. $D_F = 1.26$ (after Mandelbrot, 1982).

sides of length 1/9 are then placed over the middle third portion of each segment, and so on. After an infinite number of iterations have been completed, the length of the curve is infinite, yet the area remains less than that of a circle drawn around the original triangle.

The fractal dimension of the Triadic Koch Curve is calculated by remembering that each generator is composed of N= 4 subintervals of length r= 1/3. Thus,

$$D_f = \frac{\text{LOG } N}{\text{LOG } 1/r} = \frac{\text{LOG } 4}{\text{LOG } 3} = 1.26$$

The perimeter has a topological dimension of one since it is represented by a line, but a fractal dimension of 1.26 since that line is tortuous and partially fills up the plane.

A snowflake is a fractal object found in nature that is very difficult to describe and compare, apart from possessing a typical 6-fold anisotropy. It is often said that no two snowflakes are alike. This is because they swirl around in clouds, hence no two experience identical conditions during their formation. A very systematic and reliable method of comparing snowflake morphologies is to quantify them by calculating their fractal dimension. Since the distribution of matter in a snowflake is not constant over a range of scales, its fractal dimension is measured by evaluating the rate of change of the object's density as a function of distance in a two-dimensional plane.

The snowflake illustrated in Figure 17a, duplicated from a photograph by Bentley and Humphreys (1962), was enlarged by a factor of six from the original picture to facilitate calculations. A total of 15 concentric shells of radius ranging from 0.7 to 18 cm were drawn about six randomly selected points on the structure. Density of material within each circle was measured by placing a square grid over the figure and dividing the number of tiny squares which were part of the snowflake by the total amount counted within the entire area of the shell. This ratio is referred to as the correlation function (C(R)) (Witten and Meakin, 1983). Values were then averaged for each shell of radius R. Figure 17b shows a double logarithmic plot of R vs C(R) where the fractal dimension of the snowflake is a function of the slope and is given by:

D_F = slope + 2 = -0.16 + 2 = 1.84

The amount of material in items of constant density doubles as a function of the square of radius (D_F=2), whereas the density of material of fractal objects scales to a lesser power, the fractal dimension, since the amount of void space within the structure progressively increases with radius.

A sudden rapid decrease in the correlation function is observed at a radius of about 8 cm, the drop-off resulting from a sharp diminution in the amount of matter as the edges of the snowflake are attained.

A.

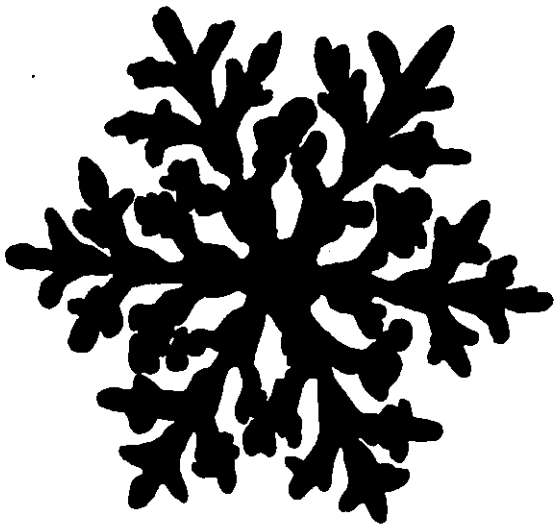

B.

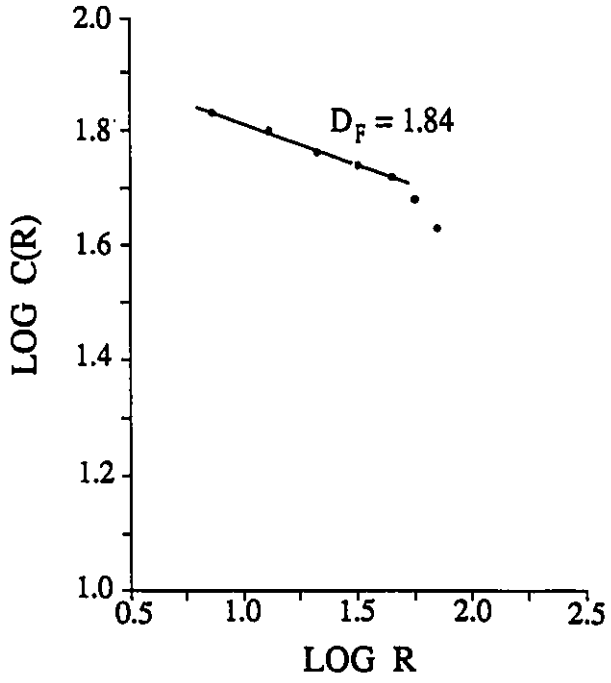

FIGURE 17. a) Sketch of a snowflake after a photograph by Bentley and Humphreys (1962). b) Fractal dimension of snowflake calculated from the correlation function method of Witten and Meakin (1983).

6.2.2 Fractal dimension of olivine crystals

Branching crystal morphologies are typically formed at temperatures below the liquidus. Their growth is thus governed by disequilibrium processes, which explains their occurrence as random, self-similar patterns. The fractal nature of the branching crystals is significant, as it is possible to quantify these textures using fractal geometry.

The fractal dimension of three branching crystals of olivine was determined using the box method, a modified version of the sandbox method of Daccord et al. (1986). The box method is much like the correlation function method applied for the snowflake, in that the two-dimensional density of material is evaluated for reducing box sizes.

The box method consists in placing a square grid over an object and counting the number of boxes (N) which contain part of that object. The process is iterated for smaller box width (b), and the slope of a log-log plot of N(b) vs 1/b is equal to the fractal dimension. Figure 18a illustrates the method, by which three square grids containing 4, 100, and 900 boxes respectively were placed over an hypothetical branching crystal. In the middle grid for example, 63 of 100 boxes of width equal to 1/10 the size of the template contained part of the texture. The log-log plot of N(b) vs 1/b (Figure 18b) yields a straight line having a slope of 1.64 (i.e. the fractal dimension of the branching form).

Prior to evaluating their fractal dimensions, the branching olivine crystals were first outlined on paper and digitized into

A.

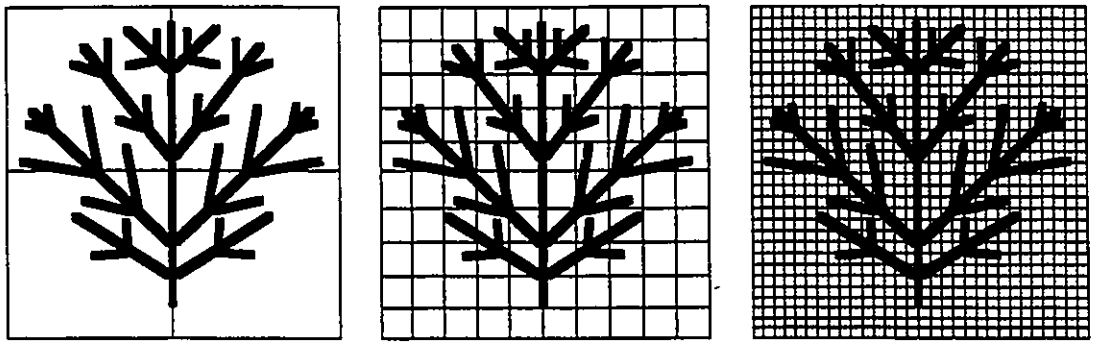

b = 1/2
N = 4

b = 1/10
N = 63

b = 1/30
N = 336

B.

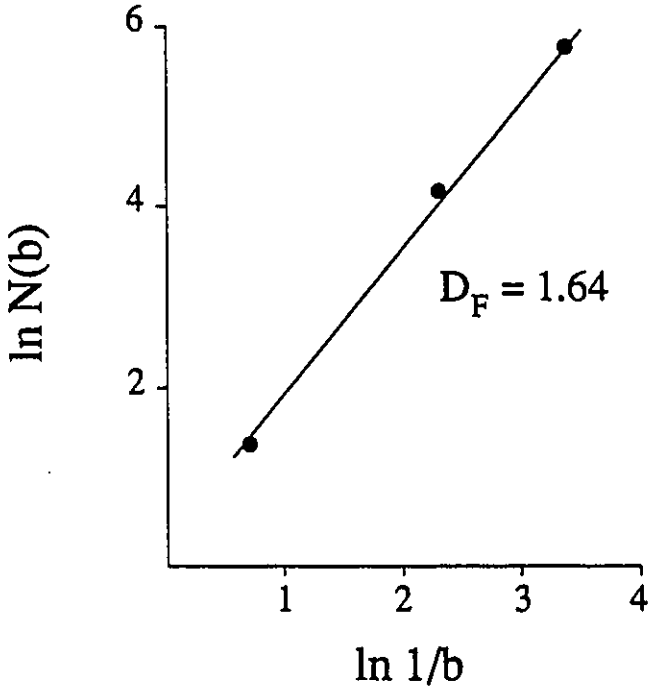

FIGURE 18. a) Determination of the fractal dimension of an hypothetical branching crystal using the box method. b = box width relative to size of template; N = number of boxes that contain part of the crystal. b) Log-log plot of N(b) vs 1/b. The slope of the regression line is equal to the fractal dimension (D_F).

a computer using a tracing tablet. Each crystal was placed in the center of a 400x400 pixel matrix on the computer screen, and a program was run that calculated N(b) values for box sizes ranging from 1 to 200 pixels in width. The iterative process operated for 14 different grid configurations. Each run yielded a set of ln N(b) and ln 1/b values, from which a linear regression was calculated to find the slope of the curve, hence the fractal dimension.

Results of the fractal dimension of three branching olivine crystals are presented in Figures 19 to 21. Fractal dimensions show little variation, ranging from 1.58 to 1.62. It is nevertheless apparent that branching crystals with the largest fractal dimension have slightly more compact structures. Results are statistically very accurate, as correlation coefficients of the linear regressions all exceed 0.999.

6.3 CRYSTAL GROWTH SIMULATIONS

6.3.1 Previous work

Experimental simulations of disequilibrium growing structures have been carried out in a variety of disciplines to investigate the relationship between growth mechanisms and morphology (Mullins and Sekerka, 1963; Meakin, 1983; Buka et al., 1986; Daccord et al., 1986; Nittmann and Stanley, 1986; Daccord and Lenormand, 1987; and Fowler et al. 1989a, 1989b, 1990). The irreversible aggregation of particles to form clusters having intricate multi-branched forms is one aspect of this problem that

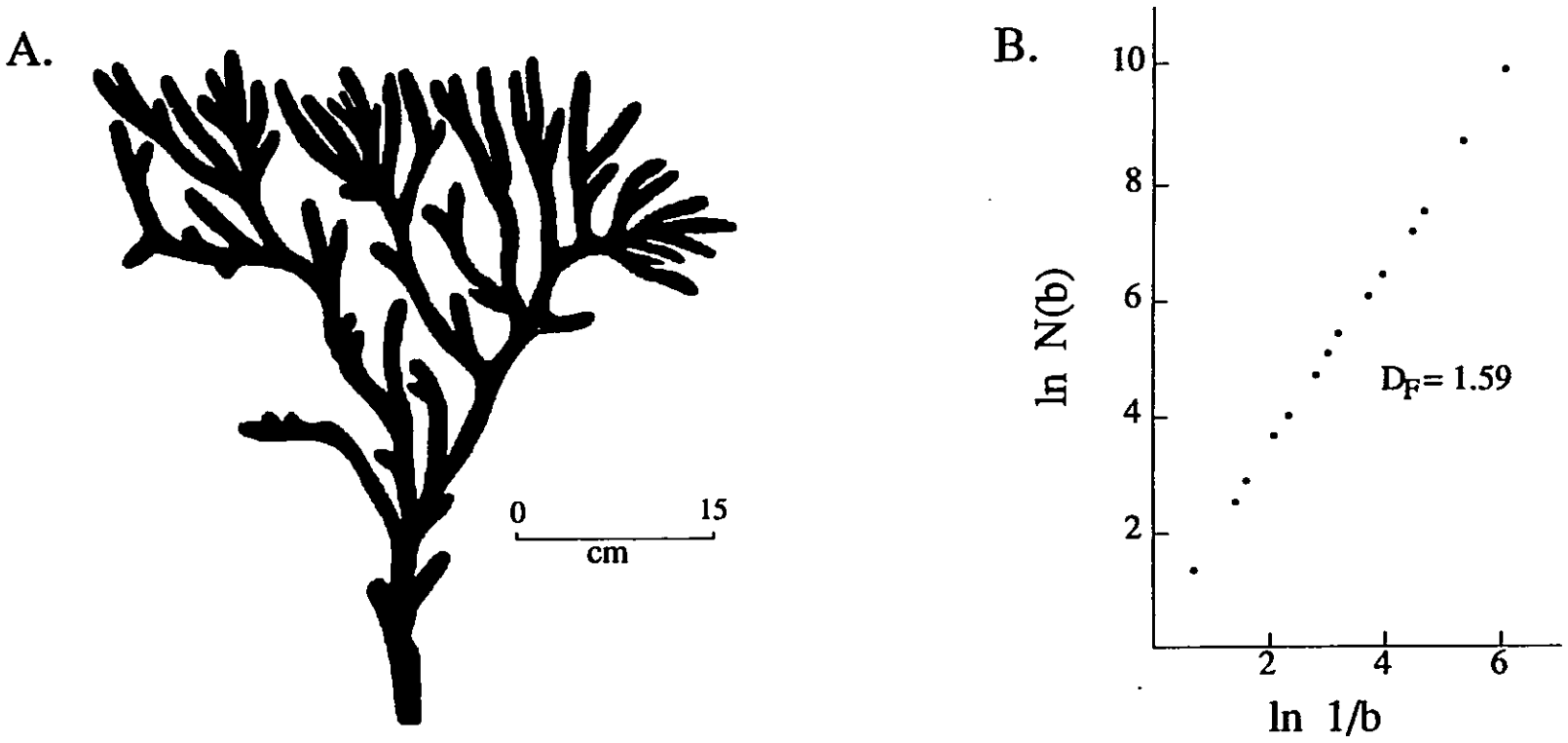

FIGURE 19. a) Schematic diagram of branching crystal (see Plate 9). b) Fractal dimension of crystal determined from the box method.

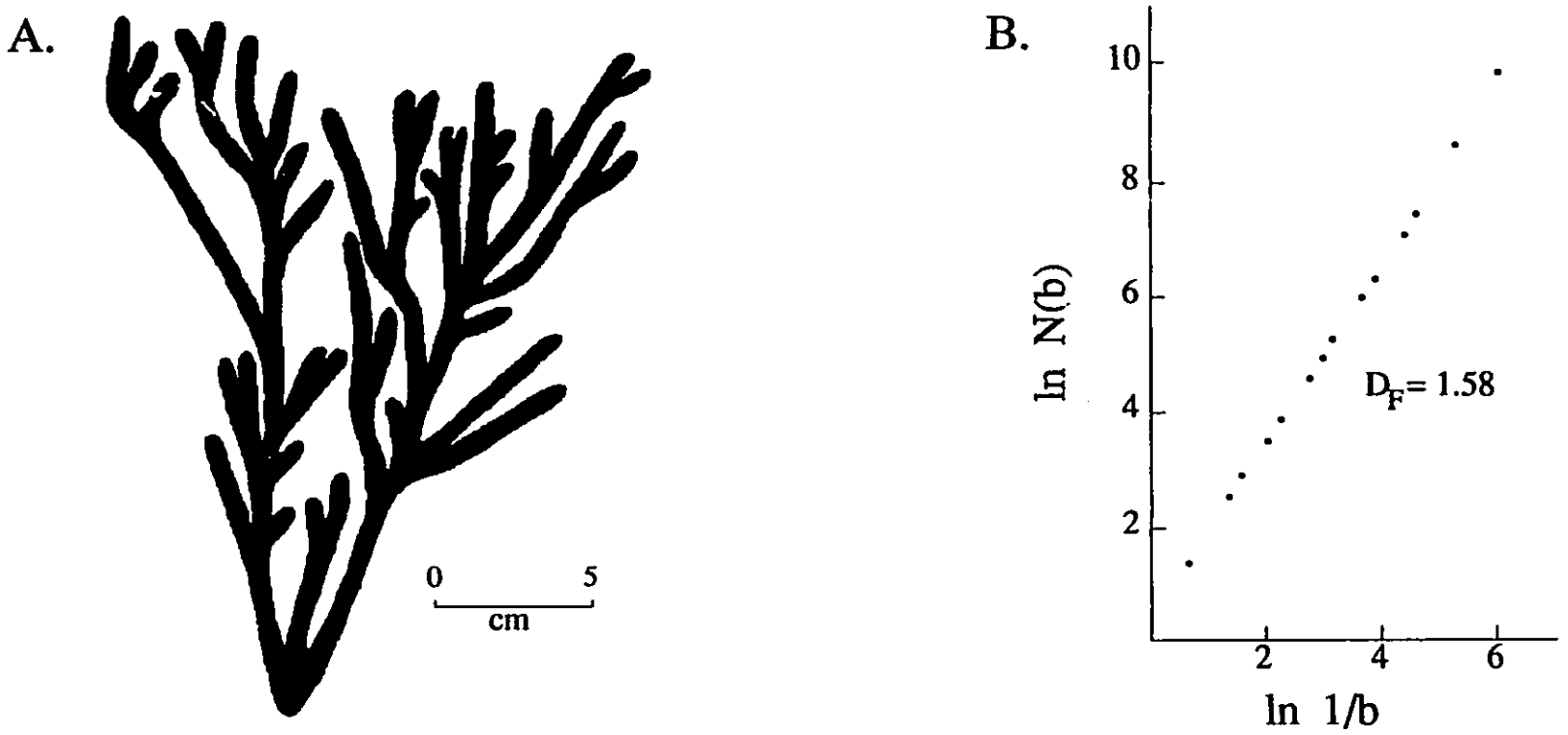

FIGURE 20. a) Schematic diagram of branching crystal (see Plate 10). b) Fractal dimension of crystal determined from the box method.

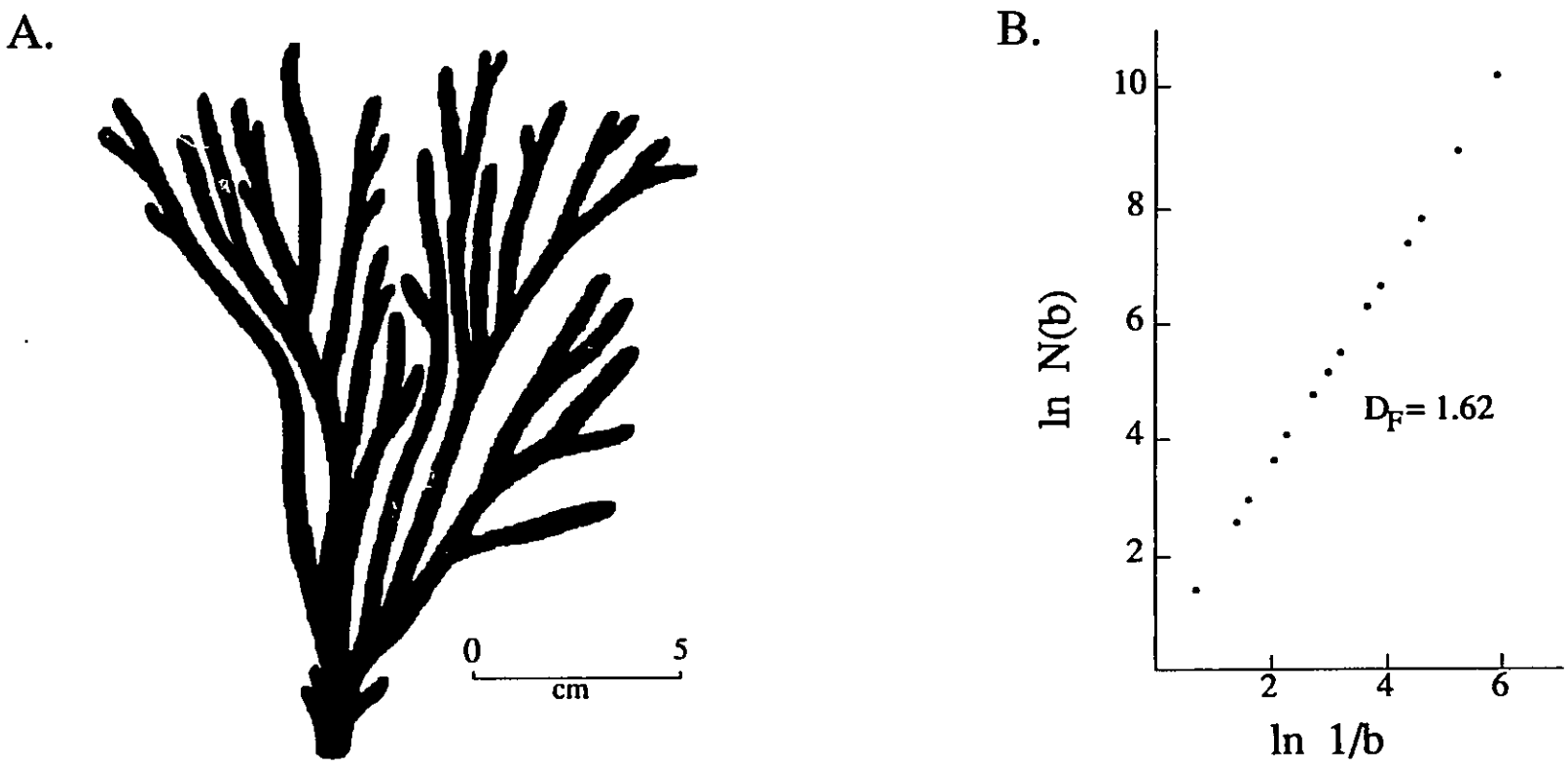

FIGURE 21. a) Schematic diagram of branching crystal (see Plate 12). b) Fractal dimension of crystal determined from the box method.

has received much attention lately. The process of particle aggregation explains the formation of soot, dust balls, colloids, and branching ice crystals on automobile windshields (Sander, 1986). The rate-limiting step in the development of such aggregates is the diffusion of matter to the growing cluster (Witten and Sander, 1983). The diffusion-limited conditions lead to the proliferation of microscopic instabilities and ultimately to the formation of complicated multi-branched aggregates.

Witten and Sander (1981) developed a lattice model that simulates the growth of a single isolated cluster by the process of diffusion-limited aggregation (DLA). The computer-generated model starts with a seed pixel (nuclei) at the centre of the lattice (computer screen). To simulate the random motion of a growth particle, pixels are illuminated sequentially at random within the lattice, and the locus of their points defines a Brownian trail (Lavenda, 1985). For ease in conceptualization, pixels will be referred to as walkers or particles. When a particle reaches a lattice site adjacent to the seed, it sticks, and another diffusing walker is released at random until it collides with the two occupied sites. An indefinitely large aggregate may be formed by the iteration of such process. Aggregates produced by the DLA algorithm of Witten and Sander display a branching structure having a fractal behaviour. A typical DLA aggregate of 3000 particles is shown in Figure 22. Note the distinct dilation symmetry of the object, which is caused by the preferred growth of the protruding arms at the

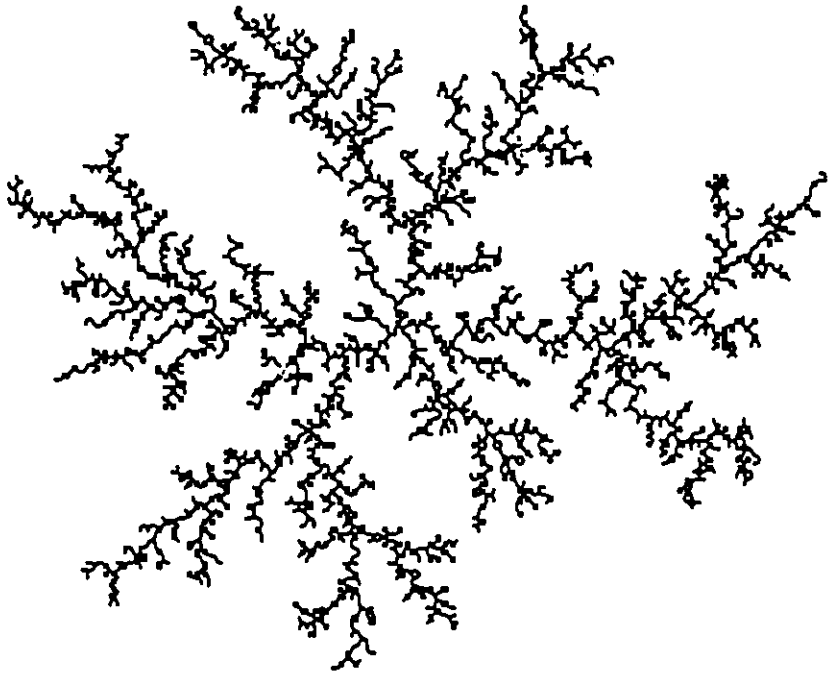

FIGURE 22. Aggregate produced using the original DLA algorithm of Witten and Sander (1981). The DLA aggregate is formed of 3000 particles and has a fractal dimension of 1.57 (after Fowler, 1990).

expense of the interior, the latter being shielded from growth. This arises because a random walker cannot penetrate the branches without collision. The DLA structure has a fractal dimension of 1.57, which is quantitatively similar to the fractal dimension of the branching olivine crystals.

Because growth processes in most natural systems occur at several growth sites and involve a large number of diffusing species, a model has been developed by Witten and Meakin (1983) to investigate the influence of multiple seeds and finite concentration of particles on DLA. Simulations were started with an array of 16 growth sites that were either ordered or randomly placed within a 200x200 lattice. Between 5000 and 20000 sites were then selected at random to represent the initial positions of the diffusing walkers. During each iteration, one of these particles is randomly chosen to move to one of its nearest-neighbour sites. The move is completed only if the selected site is unoccupied, otherwise another particle is chosen. Particles which move adjacent to a seed or cluster become part of the aggregate and are no longer selected. The process is iterated until no unconnected walkers remain. This model yields aggregates that are equivalent to those produced by the Witten-Sander model for simulations having less than 10000 particles. For larger concentrations, their is a crossover from a fractal to uniform density structure with increasing scale of observation, as clusters eventually become attached to each other and form a continuous network of particles. Hence for more realism,

simulations should be carried out using a low concentration of seeds and particles.

A feature of great importance to the multiple growth site model of Witten and Meakin is that interconnections between clusters appear only after available void spaces become infinitesimally small. The screening mechanism that prevents particles from penetrating without collision into the "fjords" of a growing cluster apparently also prevents particles from entering the "channels" between adjacent clusters.

Computer simulations have been carried out by Meakin (1983) to investigate the deposition of particles on surfaces under diffusion-limited conditions. Particles were deposited on a "surface" represented by a line of 300 growth sites at the bottom of the screen. As with the Witten-Sander model, particles were released one by one and allowed to undergo a random walk until they reached a site adjacent to the deposit. The resulting cluster is formed of a series of self-similar, open branching structures that extend vertically out of the surface. Here again, the random walkers were added largely to the protruding tips of the aggregate, with very little growth taking place in the screened inner regions.

By contrast, a simulation was performed in which particles were released vertically from the top of the screen (i.e. in the absence of diffusion). In comparison to clusters grown where particles had Brownian trajectories, this deposit developed a very dense structure having a constant distribution of matter

(i.e. $D_f = 2$). Hence deposits formed under diffusion-limited conditions have a completely different morphology than those formed when diffusional motion is not important.

Simulations were also carried out by adding a noise parameter to the original model. Two-dimensional surface deposits were grown using a sticking probability less than 1.0, implying that particles may not necessarily stick to the aggregate upon their first collision. Such simulations lead to deposits having a denser structure, as walkers can penetrate the "fjords" and stick deep within the cluster. Similar simulations have also been performed by Witten and Sander (1983).

This noise parameter was also applied by Nittmann and Stanley (1986) in simulating the growth of dendritic snowflakes. A molecular anisotropy parameter was added to the model in order to produce structures with a six-fold anisotropy characteristic of snowflakes. This was done by favouring growth in six principal directions of the lattice, leading to the development of tall, straight branches having fewer ramifications.

The disequilibrium growth of branching crystals has been simulated by Fowler et al. (1989a, 1989b) using variants of the original DLA model of Witten and Sander (1981). DLA simulations appropriately model the growth of branching crystals in a highly undercooled silicate melt, as diffusion of species rather than surface kinetics is the dominant growth-controlling factor under these conditions.

Witten and Meakin (1983) type DLA simulations have been

carried out by Fowler et al. (1989a) in order to mimic the simultaneous growth of numerous branching crystals from a melt containing a large number of molecules. A series of simulations run using progressively smaller sticking probabilities showed a gradual progression in morphology from open branching forms to more compact structures. This phenomenon was compared to the systematic change in crystal morphology observed frequently near the cooling margins of lava flows or sills, as the number of crystal-molecule collisions increases away from the margin, and surface kinetics gradually become the growth-controlling factor.

Furthermore, branching olivine crystals observed beneath the quenched margin of a basaltic flow were simulated by adding an anisotropy parameter to the Witten-Sander DLA model (Fowler et al., 1989b). The anisotropy was established by increasing the sticking probability for growth when a visited perimeter site was co-linear with two or more cluster sites. The resulting structure is comprised of branches displaying preferential growth along horizontal and vertical directions, and is qualitatively and quantitatively similar to the observed crystals.

6.3.2 DLA simulations of branching olivine crystals

The branching olivine crystals observed within the banded zone of the upper layer of gabbro have been experimentally simulated using variants of the DLA algorithm of Witten and Sander (1981). The performed experiments are a follow up of the initial work of Fowler et al. (1989a, 1989b) on computer

simulations of disequilibrium mineral growth using a DLA model.

Significant modifications have been made to the original model of Witten and Sander. All the simulations were carried out using a single seed (nuclei) placed at the bottom centre of a 250x250 pixel matrix. Particles were then randomly disposed within the lattice, and allowed to undergo a partially controlled random walk, "raining down" erratically towards the bottom of the screen. This was accomplished by preventing particles from moving in an upward direction. Each time a walker collided with the growing cluster, a new particle was re-seeded at random along the upper margin of the screen. The same procedure was followed in the case where walkers failed to strike the aggregate, either hitting the side walls or reaching the bottom of the lattice. Hence the concentration of random walkers remained constant throughout each simulation. This model conceivably simulates the unidirectional growth of branching crystals extending away from the upper margin, in response to thermal and compositional gradients.

Movement of particles within the lattice takes place following the same procedure as with the original DLA model. A particle is first selected at random and an attempt is made to transfer it to one of its nearest-neighbour sites. If the selected site is vacant, the move is completed. If it is occupied, a new particle is chosen at random and the procedure is repeated. When a particle moves adjacent to the aggregate, it becomes part of the cluster and is no longer selected.

An anisotropy parameter was added to ensure that particles gradually meandered towards the bottom seed. Different probabilities for selection were given to the eight nearest-neighbour sites surrounding a particle. Figure 23 illustrates the four different probability sets used throughout the experiments, and an approximation of the resulting path taken by the particles. In all simulations, the probability to select one of the three neighbouring sites above a particle was evidently set at zero.

The parameters used in the simulations include: 1) size of cluster; 2) concentration of walkers; 3) sticking probability; 4) anisotropic sticking probability; and 5) path of walkers.

6.3.2.1 Size of clusters

Each simulation was carried out until either 3500 or 4000 particles were part of the growing cluster, such that each aggregate had approximately the same height. The general rule was to allow the denser structures to grow to the maximum of 4000 particles. The size of each cluster is specified in the figure captions.

6.3.2.2 Concentration of walkers

A series of four simulations were produced to study the change in branch morphology using varying concentration of walkers (Figure 24). This parameter corresponds to the concentration of olivine-forming components present in the melt during crystallization of the branching olivine crystals.

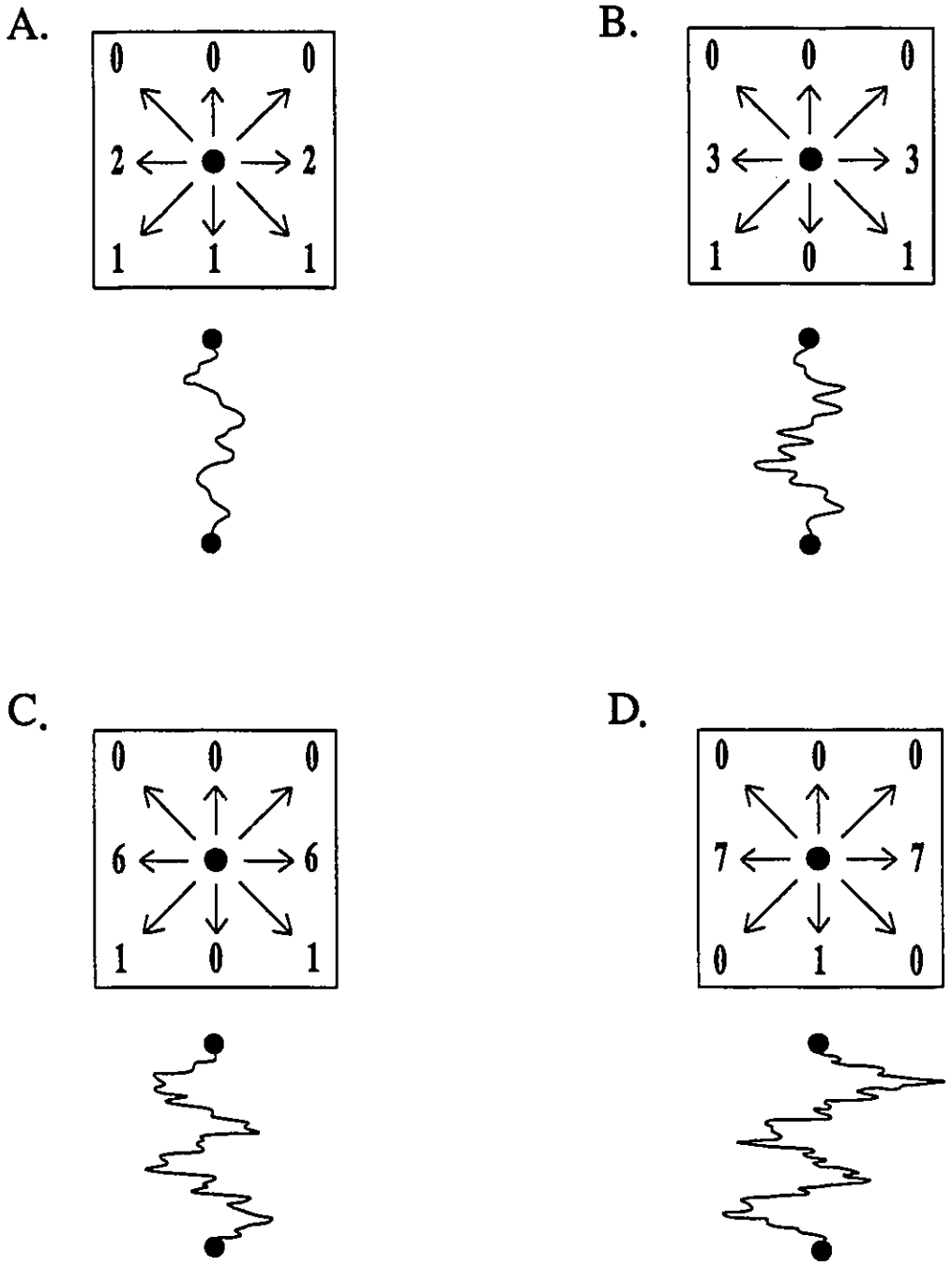

FIGURE 23. Schematic diagram showing the probability for selection assigned to the eight nearest -neighbour sites of a walking particle, and the approximate path taken by the walker. The different walker paths shown above were used in the simulations, and are referred in the text as follow: a) 21112; b) 31013; c) 61016; d) 70107.

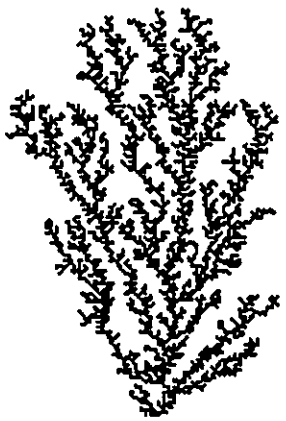

1 walker

$D_F = 1.61$

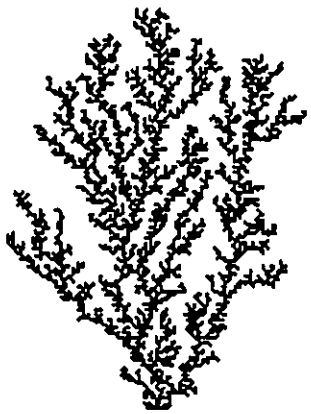

100 walkers

$D_F = 1.61$

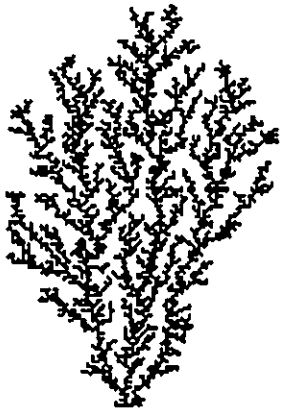

1000 walkers

$D_F = 1.62$

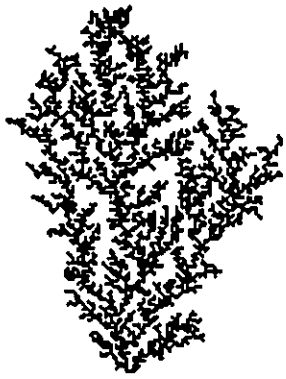

5000 walkers

$D_F = 1.63$

FIGURE 24. Simulations showing the change in aggregate morphology with increasing concentration of walkers. Note the slight increase in fractal dimension at concentrations greater than 100 walkers. Aggregates contain 4000 particles and were formed using the walker path 31013.

Each simulation was carried out using the walker path 31013 (see Figure 23b), and halted when 4000 particles were part of the cluster. As shown by Figure 24, the morphology of branches is slightly influenced by the number of walkers "raining down" during a simulation. There is a general decrease in void space between branches with increasing concentration of walkers, which is quantitatively supported by the slight increase in fractal dimension. The change in morphology is likely due to the increasing degree of interference between diffusing walkers at higher concentrations. From these results, it is clearly apparent that the change in morphology is negligible at concentrations below 1000 walkers. Hence all of the subsequent simulations were performed using a concentration of 100 walkers.

6.3.2.3 Sticking probability

Figure 25 shows the results of two series of simulations done under decreasing sticking probability (i.e. the probability that a walker will freeze to the cluster upon collision). Experiments conducted under decreasing sticking probabilities simulate melt conditions that gradually approach an equilibrium state, such that molecules may collide a large number of times before actually "solidifying" to the crystal interface. In other words, the resulting aggregates simulate the growth of branching crystals under conditions where surface kinetics gradually become the controlling factor of growth relative to diffusion kinetics.

The clusters of each series were grown to different sizes

and formed using separate walker paths: Figure 25a contains clusters of 4000 particles grown with the walker path 31013; Figure 25b includes clusters of 3500 particles formed using the walker path 70107. In each series, three simulations were carried out using sticking probabilities of 100%, 60%, and 20% respectively. At low sticking probabilities, the chance that a walker has of wandering down between two branches is greatly enhanced, as the particle may collide a number of times before actually sticking to the aggregate. This process explains why aggregates become gradually denser with decreasing sticking probability, as shown by the progressive increase in fractal dimension. Note that simulations grown with the walker path 31013 (Figure 25a) have a higher fractal dimension (i.e. denser structure) than those formed using the walker path 70107 (Figure 25b). The relationship between walker path and cluster morphology will be discussed hereafter.

6.3.2.4 Anisotropic sticking probability

Two series of simulations were completed by adding an anisotropy to the sticking probability parameter considered above (Figure 26). The anisotropy was established by assigning different sticking probabilities to the colliding walkers, whether or not they were vertically aligned with an adjacent cluster-forming particle. In the case where an incoming walker moved to a site directly above one of the particles from the aggregate, the sticking probability was fixed at 100% for all

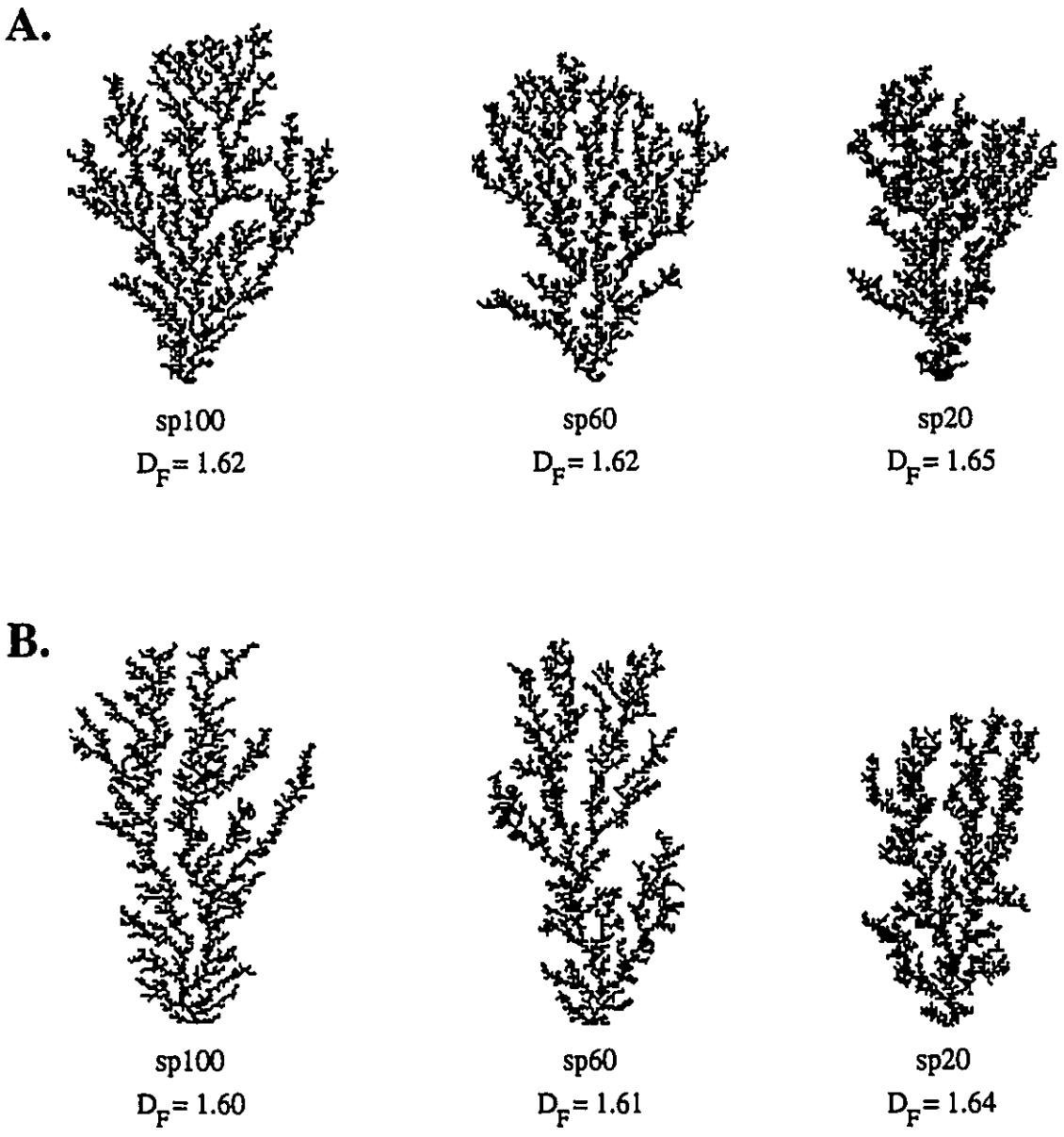

FIGURE 25. Simulations showing the change in aggregate morphology with decreasing sticking probability (sp). a) Aggregates contain 4000 particles and were formed using the walker path 31013. b) Aggregates contain 3500 particles and were formed with the walker path 70107.

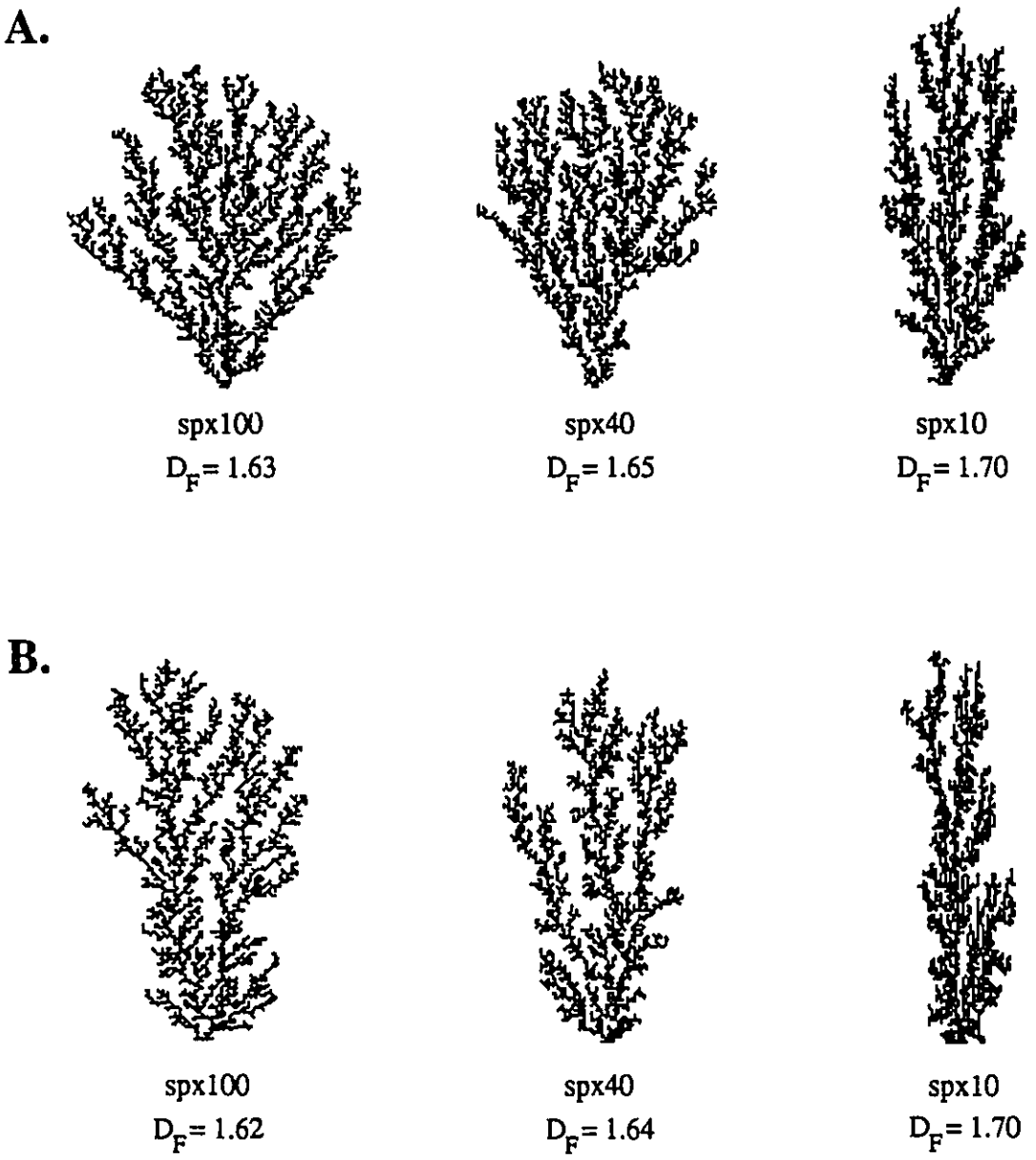

FIGURE 26. Simulations showing the change in aggregate morphology with decreasing anisotropic sticking probability (spx). a) Aggregates contain 4000 particles and were formed using the walker path 31013. b) Aggregates contain 3500 particles and were formed with the walker path 61016.

simulations. When the walker moved to any of the other neighbouring sites surrounding a cluster-forming particle, the sticking probability was gradually decreased throughout each series of simulations from 100%, to 40%, and finally to 10%. Note that the first simulations of both series (spx100) are analogous to experiments where the "isotropic" sticking probability is set at 100% (see Figure 25). The introduction of an anisotropic sticking probability parameter is an attempt to simulate conditions where the crystallography of the mineral (internal crystal structure) partially controls the positioning of molecules onto the crystal interface.

Similar to the preceding experiment, the two series of simulations were produced using different parameter values. Clusters of Figure 26a were grown to 4000 particles from the walker path 31013, whereas simulations of Figure 26b contain 3500 particles and were produced using the walker path 61016. As expected, clusters become gradually denser with decreasing anisotropic sticking probability, because walkers that are not vertically aligned with a neighbouring cluster-forming particle upon collision have an increasing chance of resuming their course towards the bottom of a "fjord". The progression in cluster density is also explained by the increasing probability that a colliding walker will stick on a perimeter site directly above a cluster-forming particle relative to other less favoured perimeter sites. The evolution of such process is apparent from the simulations, as branches gradually extend in a more upright

position to form clusters having lower opening angles and fewer branches. The change in morphology is quantitatively supported by the progressive increase in fractal dimension with degree of anisotropy. As in the previous experiment, a decrease in fractal dimension is observed when comparing simulations from both series, as the path taken by the "raining" walkers is more sinuous.

Although more work is needed, this type of DLA experiment (i.e. anisotropic sticking probability) qualitatively simulates physical growth where crystallographic properties of the mineral (i.e. surface kinetics) progressively control the morphology with decreasing undercooling, resulting in more compact structures having fewer ramifications. It must be stressed that such anisotropy could have been established to favour growth along any other directions (e.g. laterally), leading to more open aggregates. However, the main conclusion to be drawn from this experiment is that a crystallographic control may be introduced to the DLA model.

6.3.2.5 Path of walkers

Figure 27 shows the results of aggregates grown with different walker paths. Simulations were carried out using progressively more tortuous walker paths, as illustrated in Figure 23a to 23e. This parameter was set up in order to simulate possible trajectories taken by molecules in a melt solidifying under thermal and compositional gradients.

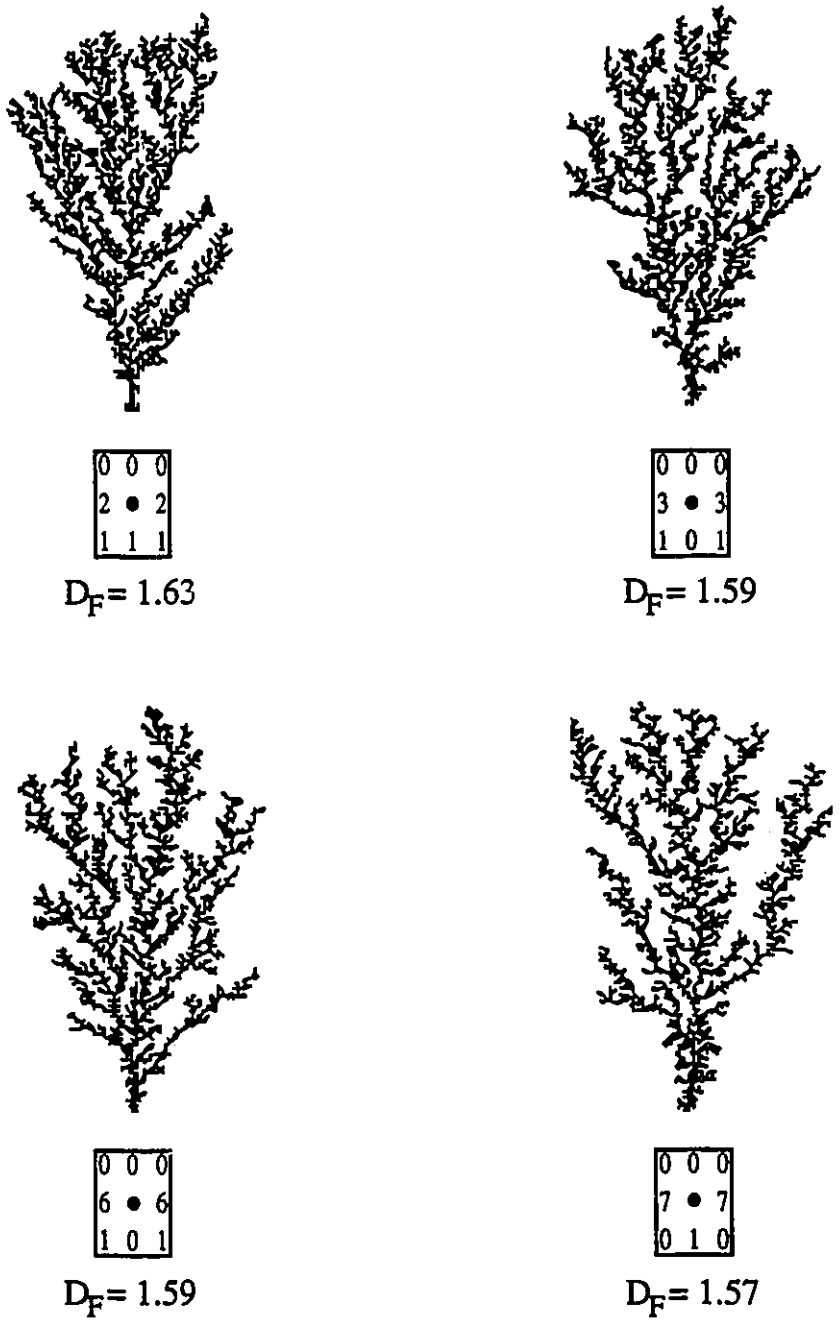

FIGURE 27. Simulations showing the change in aggregate morphology produced by increasing the sinuosity of the walker path. Aggregates contain 3500 particles and were formed using an anisotropic sticking probability (spx) of 3% for the first 100 walkers to stick, followed by a "standard" sticking probability of 100% for the remaining ones to aggregate.

The clusters were all grown to a size of 3500 particles using a sticking probability of 100%. However, an anisotropic sticking probability of 3% identical to that of the previous experiment was set for the first 100 walkers to stick, such that the formation of side branches was temporarily hindered in the earliest stages of growth. The resulting clusters are nonetheless nearly identical to those formed under sticking probabilities of 100% in the preceding experiments.

A gradual decrease in the density of clusters is observed when increasing the degree of sinuosity of the walker path, which is supported by the systematic change in fractal dimension from 1.63 to 1.57. The increase in void spaces between branches is explained by the fact that a walker having a high lateral component of diffusion is likely to aggregate along the extremities of branches before having the chance of meandering towards the bottom of a "fjord". In other words, the probability of causing growth between two branches is significantly reduced by favouring lateral movement of walkers.

It is concluded that clusters grown using the walker paths 31013 and 61016 most closely simulate the branching olivine morphologies of the banded zone.

6.3.3 Suggestions to improve the DLA model

In light of the strong resemblance (both qualitatively and quantitatively) between the computer-generated aggregates and the observed branching olivine crystals, it is concluded that: 1) the

DLA algorithm is an appropriate model for qualitatively simulating the process of disequilibrium growth of crystals from an undercooled melt; and 2) the diffusion of species to the growing crystal is likely the dominant factor controlling the formation of these textures. Further modifications to the DLA algorithm would be required to better simulate the mechanisms involved during diffusion and growth, ultimately giving the computer-generated branches, a more natural appearance.

One of the main problems with the DLA algorithm is that it yields aggregates containing a profusion of very narrow branches (i.e. one pixel in width), whereas the olivine crystals are formed of wide branches having fewer ramifications. This discrepancy is probably related to the fact that in the simulations, branching occurs at random and is not controlled by properties intrinsic to the aggregate, whereas in a crystallizing melt, branching is partly controlled by surface kinetic features inherent to the crystal structure of the mineral. For branching to occur, a protuberance must develop along the interface and extend far enough to become a favoured site for the attachment of growth species. Since this branching process occurred less frequently in an olivine crystal than in a DLA cluster, given the lower number of observed ramifications, it is interpreted that small perturbations forming along the crystal interface were readily obliterated due to the control exerted by the internal structure of the crystal.

The series of simulations produced using an anisotropic

sticking probability (Figure 26) was an attempt at trying to simulate conditions where crystallographic properties partly control the development of crystals. As the anisotropy was set up to progressively favour growth in a vertical direction, the resulting aggregates gradually showed a reduction in the frequency of branching. However, the amount of third and fourth order branches (i.e. small scale branches), although grown significantly shorter in the most anisotropic aggregate, remained fairly constant throughout. The difficulties enccuntered in producing aggregates having few branches is apparently directly related to the nature of the anisotropy imposed on the growing cluster. Perhaps more severe constraints must be set when defining an anisotropy parameter, such that the chance of sticking in an undesired position is highly improbable. An alternative solution would be to allow recently aggregated particles the opportunity of relocating along the perimeter. This process is known to occur during the development of crystals grown at temperatures closer to equilibrium conditions, as molecules rearrange their orientation in accordance with the crystal lattice (Fowler, 1990).

Further modifications which could be appended to the DLA model to better simulate the growth of crystals are: 1) the use of walkers having different sizes, shapes, and charges; 2) allow walkers to combine and disassemble like components in a melt; and 3) the production of three-dimensional simulations.

6.4 DISCUSSION

The origin of skeletal, dendritic and branching crystal morphologies typically has been ascribed to rapid cooling and undercooling of a silicate liquid. These conditions have been postulated to explain the skeletal and dendritic olivine crystals from both Archean volcanic spinifex rocks (Viljoen and Viljoen, 1969, Lajoie and Gélinas, 1978, and Huppert et al., 1984) and harrisitic rocks of the Rhum intrusion (Wadsworth, 1961, Wager and Brown, 1967). The presence of these textures in rocks that have crystallized from such two contrasting environments is certainly not coincidental. Hence crystal growth kinetics may also be governed by particular melt characteristics in addition to the thermal history of these rocks. Among the parameters which could have influenced the growth of the branching olivine crystals are: 1) the concentration of olivine components in the melt; 2) the nucleation rate; 3) the growth rate and diffusion rate; 4) the volatile content; and 5) the oxygen fugacity.

6.4.1 Olivine content

An experimental investigation of olivine crystal morphology by Donaldson (1976) showed that the cooling rate at which a particular olivine shape grows decreases with increasing olivine content of the melt. For example, dendritic crystals were formed at a cooling rate of 3°C/n in an olivine eucrite melt (40% normative olivine), but at a rate of 300°C/h in an olivine basalt melt (9% normative olivine). He concluded that the Archean

spinifex rocks were not formed by rapid cooling, but rather by rapid crystal growth caused by the supersaturation of olivine in the melt.

Supersaturation of olivine is attained at a relatively low degree of undercooling, olivine-enriched melts having very shallow liquidus slopes in temperature-composition space (Figure 28) (Wyllie, 1960). The initiation of supersaturation necessary to form the harrisitic rocks of the Rhum pluton have been attributed to changing water content or adiabatic expansion of the magma (Donaldson, 1974).

At Centre Hill, saturation of fayalitic olivine in the highly fractionated residual melt may have promoted rapid growth of crystals at low cooling rates and slight undercooling. However, the branching olivine crystals are not solely characterized by their significant grain size, but also by their low crystal population density.

6.4.2 Nucleation rate

The number of olivine crystals per unit of volume in bands of BTG is estimated at 100 individuals per cubic metre. This low population density of crystals indicates that nucleation was fairly restricted during the growth of the branching crystals. Dynamic crystallization experiments have shown that nucleation does not occur as readily in melts that have been superheated well above their liquidus temperature, because all potential nucleation sites are destroyed (Donaldson, 1976, Lofgren et al.,

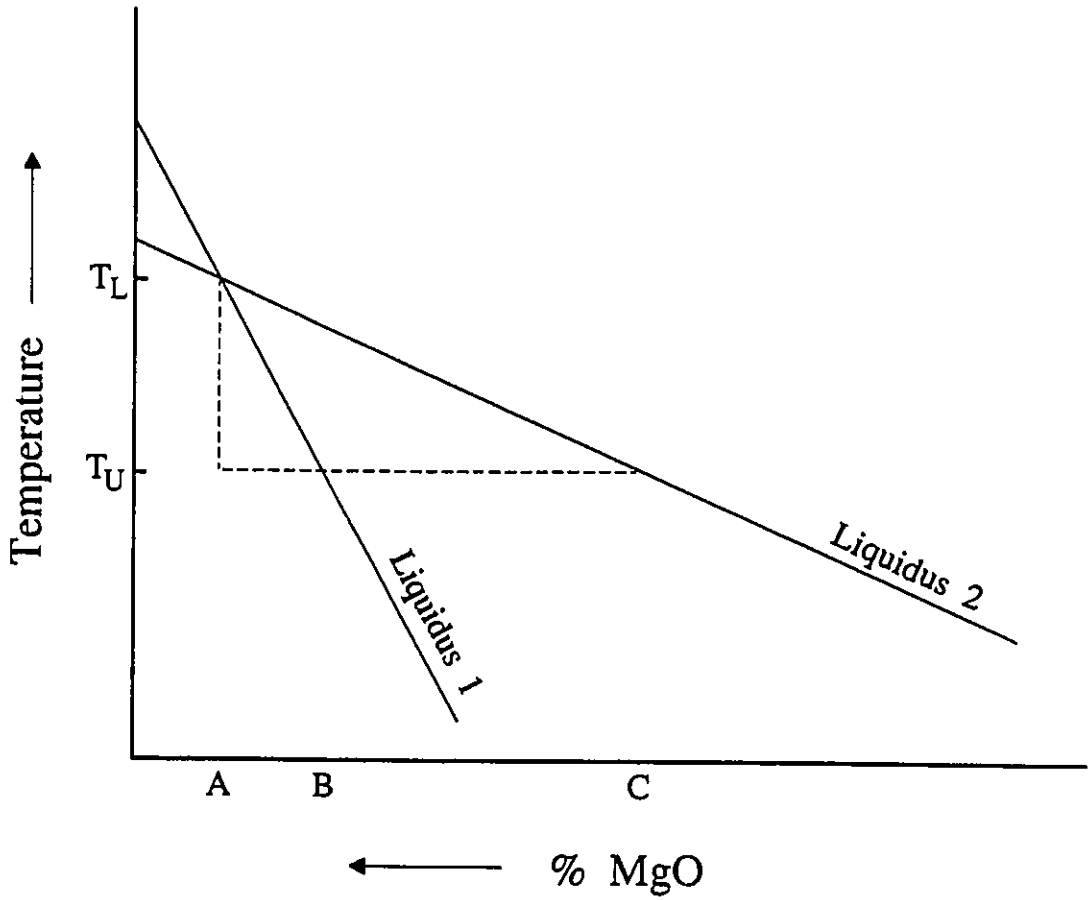

FIGURE 28. Effect of liquidus slope on supersaturation at a given degree of undercooling. For the same degree of undercooling (T_L - T_U), melt A of steep liquidus slope (liquidus 1) is slightly supersaturated (A-B), whereas the degree of MgO supersaturation is much greater (A-C) if it has a shallow liquidus slope (liquidus 2). T_L = liquidus temperature; T_U = undercooling temperature.

1978, and Lofgren, 1983). However, considerable superheating is required to eliminate olivine remnants or substrates favourable to heterogeneous nucleation (i.e. "nucleation" on a pre-existing substrate) (Lofgren, 1983). Spontaneous nucleation of a crystal (i.e. homogeneous nucleation) probably never occurs in magmas of basaltic composition, as the free energy of activation for nucleation is considered insurmountable (Lofgren, 1975, and Berkebile and Dowty, 1982). In any case, it is very unlikely that the low crystal population density is due to superheating of the magma prior to emplacement, as forsterite crystals nucleated abundantly in the early stages of fractionation.

Work by Spohn et al. (1988) on the crystallization of a two-component melt shows that the nucleation and growth rate functions are very sensitive to undercooling, and that both parameters attain peak amplitudes at different undercooling. It is shown from figure 29 that crystal growth dominates at low undercooling, as the nucleation rate is close to zero. Olivine crystals produced in the laboratory by Donaldson (1977) at 30-50 °C of undercooling were few in number and characterized by large branching forms, further supporting the theoretical model.

Accordingly, the branching olivine crystals of the BTG are interpreted to have formed under slightly undercooled conditions in light of their very low crystal population density. Further evidence supporting such interpretation include the occurrence of long acicular crystals of plagioclase throughout the banded zone, and skeletal crystals of plagioclase and clinopyroxene within the

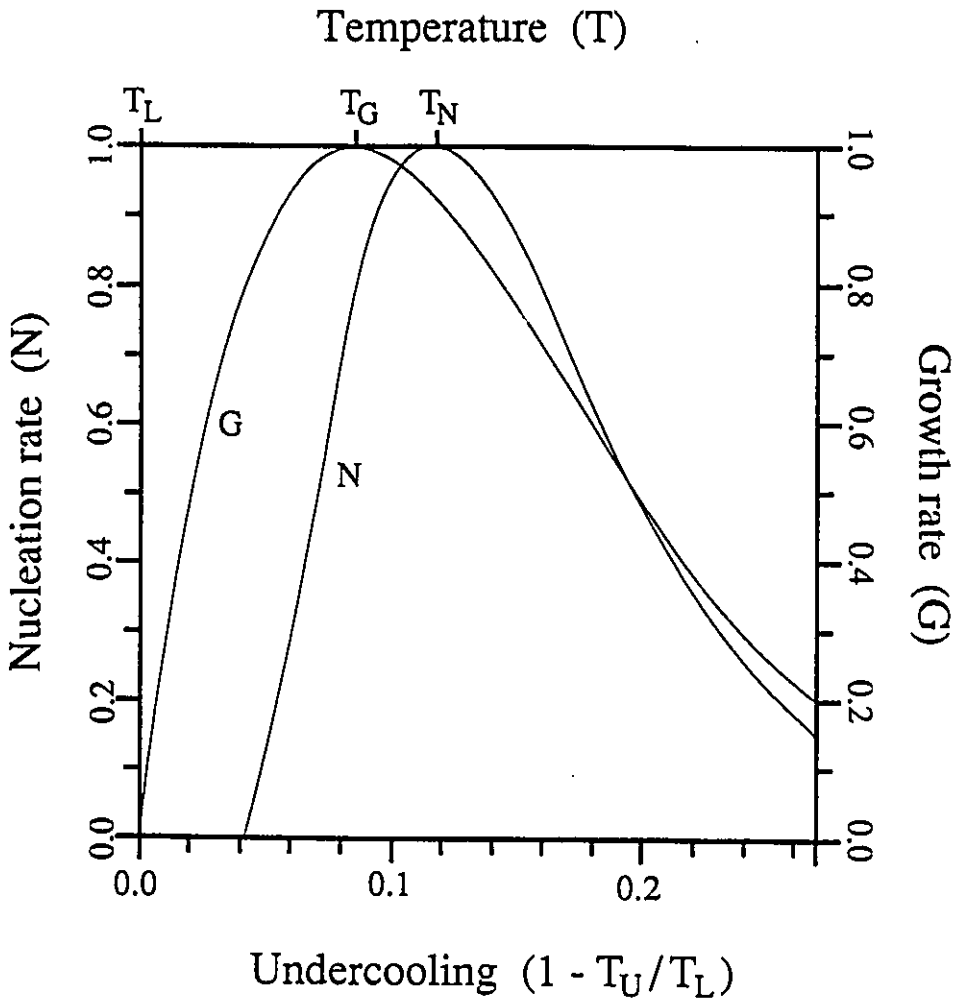

FIGURE 29. Effect of undercooling on nucleation rate and growth rate. Both functions are dimensionless and scaled according to their peak amplitudes. Temperature is in K. T_L = liquidus temperature; T_G = maximum growth rate temperature; T_N = maximum nucleation rate temperature; T_U = undercooled temperature (modified after Spohn et al., 1988).

marginal gabbro.

As it is assumed that the branching olivine crystals originate from a highly fractionated melt that ponded from the interior of the chamber, it thus becomes difficult to explain their irregular distribution in the banded zone, being abundant in bands of BTG, and very scarce or absent in bands of CTG. The actual distribution of branching crystals in the banded zone may in fact reflect the dispersion of preexisting olivine nuclei prior to the upwelling of the differentiated melt. The fact that numerous branching crystals were found "anchored" along the lower contact of bands of CTG, growing into underlying bands of BTG, indicates that some olivine nuclei formed directly along the contact plane on pre-existing crystals. Knowing that Mg-rich olivine was the first phase to crystallize following each postulated magma replenishment event, it is conceivable that olivine nuclei may have been trapped into the advancing crystallization front during formation of a band of BTG. The rare occurrence of branching crystals within bands of CTG is thus to be expected, as clinopyroxene and plagioclase were the dominant liquidus phases in the later stage of each cyclic episode.

6.4.3 Growth rate and diffusion rate

One of the most intriguing feature of the branching olivine crystals is their extremely large size, as observed crystals range from 15 to 55 cm in length. Rapid growth rate is commonly proposed in explaining the origin of such large crystals in mafic

intrusions (Donaldson, 1974, 1977, and Berg, 1980).

Study of crystal growth phenomena in silicate melts has been carried out by several workers (Kirkpatrick, 1975, Fenn, 1977, Swanson, 1977, Swanson and Fenn, 1986, and Muncill and Lasaga, 1988). The growth rate of a crystal may be controlled by any of the following processes: 1) interface kinetics (i.e. the attachment of atoms and molecules and diffusion along the growing surface of a crystal); 2) diffusion in the melt (i.e. transport of material through the melt); and 3) heat transfer (i.e. removal of latent heat of crystallization away from the crystal-liquid interface) (Dowty, 1980). Interface reactions are expected to control the growth rate at very small degrees of undercooling, as in the case of most large magma bodies (Kirkpatrick, 1974). Diffusion becomes the controlling factor with increasing degree of undercooling. It has been experimentally demonstrated that the growth rate of an individual phase will increase to a maximum, and then decrease with progressively higher degrees of undercooling, as diffusion of material is greatly reduced (Kirkpatrick et al., 1976, and Swanson, 1977).

A dynamic crystallization experiment by Lofgren (1974) on plagioclase crystal morphology showed a progression in habit from tabular to skeletal, to dendritic, and finally to spherulitic crystals with increasing undercooling. The systematic variation was attributed to a gradual decrease of the diffusion rate to growth rate ratio (D/G). Under equilibrium conditions, the rate of advance of a growing crystal is comparable to the rate at

which rejected components diffuse away from the crystal-liquid boundary. The interface is stable and the growth of smooth, planar crystal faces arise, as the crystal assumes its equilibrium shape. When a melt is undercooled, an impurity layer enriched in rejected, low-temperature melting components surrounds the growing crystal, creating a constitutionally undercooled zone (Kirkpatrick, 1975). The concentration of impurity in the melt gradually decreases away from the interface, causing a gradual increase in the liquidus temperature and degree of undercooling until the outer limit of the impurity layer is reached (Figure 30). A decrease in the width of the impurity layer is observed with increasing undercooling, as the D/G ratio is gradually lowered. Since both the undercooling and concentration of growth components gradually increase away from the crystal-liquid interface, random perturbations forming along the planar interface are forced to grow more rapidly, as they protrude into a region of greater undercooling and higher concentration of growth components. This results in the breakdown of the planar interface to produce crystals having a skeletal, dendritic, spherulitic, or ultimately a branching morphology (Lofgren, 1980).

Stating that branching crystal morphologies grow at a very low D/G ratio does not necessarily imply rapid growth rate. A considerable reduction in the mobility of the slowest crystal-forming components in a melt is sufficient to create a zone of undercooled rejected solute around the growing crystal. This

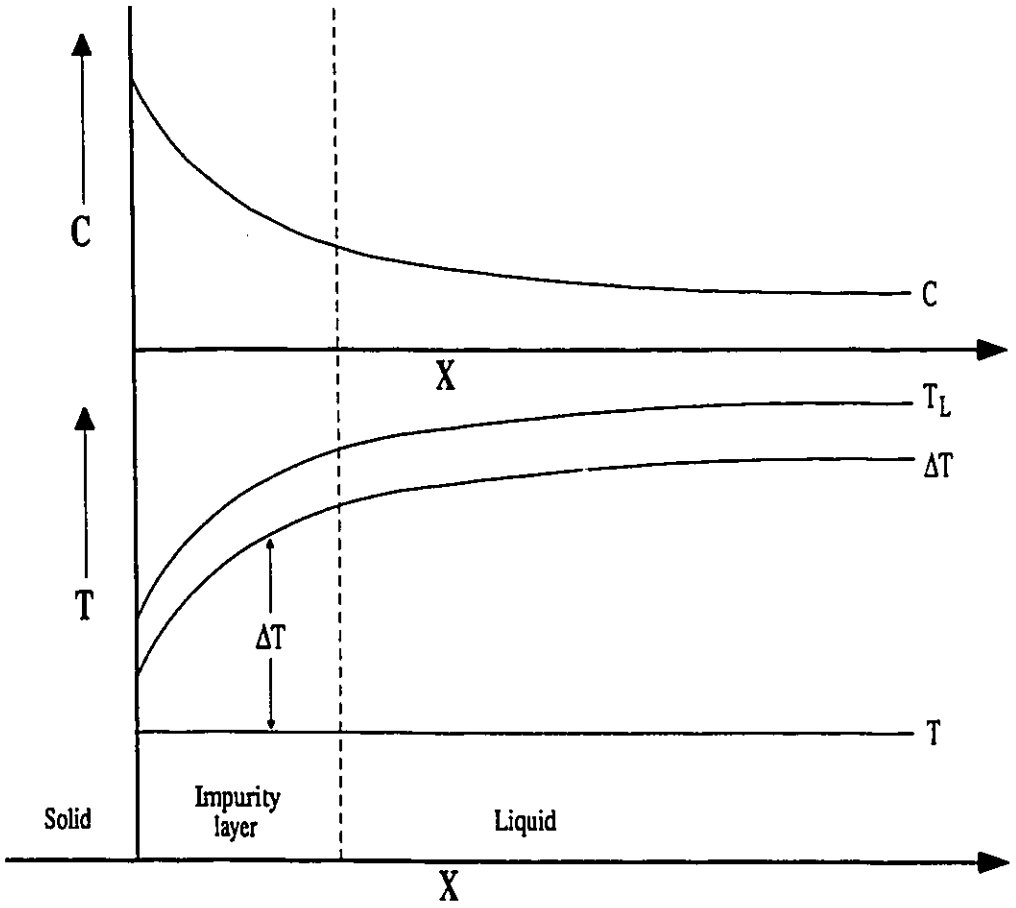

FIGURE 30. Plot of temperature and impurity gradients adjacent to a growing crystal interface. X = distance from the crystal interface; C = impurity concentration; T = actual temperature; T_L = liquidus temperature; ΔT = amount of undercooling (modified after Lofgren, 1974).

behaviour is expected particularly at low crystallizing temperatures, as diffusion rates are known to decrease exponentially with decreasing temperature (Baker and Grove, 1985). The decrease in diffusion rate with temperature is attributed to the increasing viscosity of the melt, and to a reduction in atomic vibration frequency. Viscosity-temperature relations of mafic melts have been investigated by Scarfe (1973), and show a general increase in viscosity with decreasing melt temperature. The viscosity of a melt is also affected by pressure, melt composition, volatile content, and oxygen fugacity (Lofgren, 1980).

The branching olivine crystals of Centre Hill are interpreted to have crystallized from a highly fractionated melt under diffusion limited conditions and increasing melt viscosity. Such interpretation is supported by: 1) the low melt temperature of the evolved liquid relative to the temperature of the primary magma; 2) the silica and iron content of the melt; and 3) the shallow level of emplacement of the sill. Volatile content and oxygen fugacity, which may also influence viscosity and diffusivity, are considered later.

As it is well established that the branching crystals formed in the later stage of fractionation, they must have crystallized from a relatively viscous melt enriched in low melting components.

The silica content was evidently high in the residual melt, owing to the presence of large quartz grains and significant postcumulus granophyric intergrowths in the middle portion of the

upper layer of gabbro. SiO_2 is a strong network former, meaning that it polymerizes the melt and thus increases melt viscosity. Furthermore, precipitation of ilmenite in the upper layer of gabbro was relatively abundant, and likely occurred through strong iron enrichment of the melt prior to the formation of fayalitic olivine. The latter statement is supported by the presence of ilmenite enclosed within the BTG olivine oikocrysts. Precipitation of ilmenite increases the $Fe^{3+}/\Sigma Fe$ ratio of the residual melt, thereby increasing its viscosity, as ferric iron is generally a network forming cation in iron-bearing silicate melts (Mysen et al., 1985, and Dingwell et al., 1988).

The Munro Lake sill and several other differentiated sills in the vicinity of Munro Township are interpreted to have crystallized at very shallow levels of the crust (MacRae, 1969, Eakins, 1972, and Johnstone, 1987). Measurements by Scarfe (1986) on the viscosity of anhydrous melts as a function of pressure show a small gradual increase in viscosity with decreasing pressure. Furthermore, the chemical diffusivity of oxygen in basaltic melts was shown by Dunn (1983) to gradually decrease with reducing pressure. Hence diffusion limited conditions in the residual melt may have been enhanced by low pressures.

6.4.4 Effect of volatiles

Water and some other volatile phases such as fluorine and chlorine are known to have a depolymerizing effect on melt structure, thus reducing the viscosity of a melt (Scarfe, 1986,

and Dingwell and Mysen, 1985). The decrease in viscosity is significantly greater for more felsic melts, as the addition of water to already depolymerized basic melts as little effect on their melt structure. Increasing water content of a melt was also shown by Watson (1981) to dramatically increase the diffusivity of certain elements such as phosphorous, calcium, and zirconium.

The residual melt from which quartz and fayalite precipitated was seemingly enriched in silica, implying that the melt viscosity would have been affected by the concentration of a volatile phase. However, that a significant amount of volatiles was present in the residual melt at Centre Hill remains doubtful. Miarolitic cavities, which are occasionally found in the granophyric zone of shallow level sills and dykes (Hyndman, 1985), were not observed.

6.4.5 Oxygen fugacity

Dynamic crystallization experiments conducted by Lofgren (1974) on natural oceanic ridge basalt samples showed that decreasing the oxygen fugacity increased the liquidus temperature of the basalt, thereby increasing the degree of undercooling. Hence at the same crystallization temperature, acicular pyroxene crystals were formed at log fO_2 = -8, while spherulitic crystals grew at log fO_2 = -14. A similar experiment by Donaldson (1976) on olivine crystal morphology showed that varying the oxygen fugacity had no influence on crystal shape.

A decrease in oxygen fugacity may be attained by the escape

of a volatile-rich vapour phase in the later stage of fractionation. However, no evidence of such an event has been observed at Centre Hill. It is suggested that the oxygen fugacity of the Centre Hill liquid had no influence on the development of the branching olivine crystals, as it apparently remained at a fairly low level throughout fractionation. Based on petrography, the fO_2 lay approximately along the fayalite-magnetite-quartz (FMQ) buffer reaction towards the end of fractionation (Morse, 1980).

CONCLUSIONS

When this project was undertaken, the main objective was to explain the origin of the conspicuous branching textures emerging near the upper margin of the Centre Hill complex. From petrological observations and geochemical data, as well as computer-generated simulations of the textures, a link was made between the intricate morphology, the crystal growth kinetics, and the physical and chemical characteristics of the melt.

The branching textures are in remarkable contrast with the surrounding rock matrix. Apart from their spectacular shape, the branching structures have a distinct brick red colouration on weathered outcrop surfaces, reach substantial dimensions (they average 25 cm in length), display a very low population density, and consistently extend perpendicular to the layering. Based on the geochemical composition of the secondary metamorphic assemblage, the branches were found to have been originally composed of fayalite (~Fa_{95}), an Fe-rich olivine.

The fayalite crystals are interpreted to have grown within a crystal-liquid mush, as they enclose smaller crystals of plagioclase, clinopyroxene and Fe-Ti oxide that abound in the surrounding matrix. The late fractionation of fayalite is further supported by phase equilibria, as iron enrichment of the residual melt and the reappearance of olivine as a liquidus phase are typical features associated with reduced tholeiitic magmas.

The branching morphologies have been identified as fractal

objects, being composed of a hierarchy of branching parts that are self-similar over a large range of scale. Two-dimensional imprints of the textures consistently yielded fractal dimensions approximating 1.6.

The branching textures were qualitatively and quantitatively simulated on the computer using a variation of the Witten-Sander diffusion limited aggregation algorithm. From the DLA simulations, it was established that the growth of branching crystals was limited by diffusion of molecules to the crystal-liquid interface, and that the resulting morphology was controlled by two opposing phenomenon: 1) the random aggregation of growth molecules along the crystal periphery without relocation; and 2) the systematic arrangement of molecules onto the growing interface according to the internal crystal structure of the mineral. It is suggested that these two competing "forces" dictate the morphological development of crystals, from well faceted crystals where the internal structure of the mineral is the dominant growth-controlling factor (i.e. near liquidus temperatures), to disequilibrium shapes where growth species aggregate under diffusion limited conditions (i.e. undercooled state).

Apart from the low diffusivity of growth molecules in the melt, other factors that may have contributed to the development of disequilibrium crystals of olivine include: 1) the high concentration of olivine components in the melt; 2) the very low nucleation rate of olivine; 3) the rapid growth of olivine

crystals; and 4) the viscous nature of the residual liquid.

Although not an important goal of this thesis, a petrogenetic model was nonetheless established to explain the origin of cyclic layering in the Centre Hill complex. It was postulated that cyclic units formed by fractional crystallization through repeated injection of fresh magma to the chamber. Based on the petrography and field examinations, cyclic units apparently developed simultaneously at the bottom (peridotite/clinopyroxenite cycles) and top (branching-textured and clotted-textured gabbro cycles) of the sill following each magma replenishment event.

Two different hypotheses have been envisaged to explain the appearance of the branching olivine crystals within the petrogenetic framework: 1) the final portion of residual liquid from the last batch of injected magma migrated upwards through the banded zone and crystallized Fe-rich olivine within the bands of BTG (model 1); and 2) branching olivine crystallized in the later stages of each cyclic event from the stagnant interstitial liquid trapped within bands of BTG (model 2).

Although several occurrences of branching crystal morphologies have been reported from mafic plutonic rocks, the branching olivine crystals of the Centre Hill complex are clearly unprecedented in terms of their unusual size and spectacular branching framework. The severe disequilibrium conditions under which they formed may have been caused by extremely high concentrations of iron in the residual melt, enhanced by episodic replenishment of

parental magma, or perhaps by atypical cooling conditions induced by the thin sialic crust of Archean time.

REFERENCES

Arndt, N.T., Naldrett, A.J. and Pyke, D.R. 1977. Komatiitic and Fe-rich Tholeiitic Lavas of Munro Township, Northeastern Ontario. J. of Petrology, Vol.18, Part 2, p.319-369.

Arndt, N.T. and Nesbitt, R.W. 1984. Magma Mixing in Komatiitic Lavas from Munro Township, Ontario. In Archean Geochemistry, Hansen, G., Kroner, A. and Goodwin, A.W. (Eds.), Springer-Verlag, Berlin, p.99-114.

Baker, M.B. and Grove, T.L. 1985. Kinetic Controls on Pyroxene Nucleation and Metastable Liquid Lines of Descent in a Basaltic Andesite. Am. Min., Vol.70, p.279-287.

Bentley, W.A. and Humphreys, W.J. 1962. Snow Crystals. Dover Publications Inc., New York, 227 p.

Berg, J.H. 1980. Snowflake Troctolite in the Hettasch Intrusion, Labrador: Evidence for Magma-Mixing and Supercooling in a Plutonic Environment. Contrib. Min. Pet., Vol.72, p.339-351.

Berkebile, C.A. and Dowty, E. 1982. Nucleation in Laboratory Charges of Basaltic Compositions. Am. Min., Vol.67, p.886-899.

Bottinga, Y. and Weill, D.F. 1970. Densities of Liquid Silicate Systems Calculated from Partial Molar Volumes of Oxide Components. Am. J. Sci., Vol.269, p.169-182.

Buddington, A.F. and Lindsley, D.H. 1964. Iron-titanium Oxide Minerals and Synthetic Equivalents. J. of Petrology, Vol.5, p.310-357.

Buka, A., Kertész, J. and Vicsek, T. 1986. Transitions of Viscous Fingering Patterns in Nematic Liquid Crystals. Nature, Vol.323, p.424-425.

Campbell, I.H. 1977. A Study of Macro-Rhythmic Layering and Cumulate Processes in the Jimberlana Intrusion, Western Australia. Part 1: The Upper Layered Series. J. of Petrology, V.18, Part 2, p.183-215.

Campbell, I.H. and Nolan, J. 1974. Factors Effecting the Stability Field of Ca-Poor Pyroxene and the Origin of the Ca-Poor Minimum in Ca-Rich Pyroxenes from Tholeiitic Intrusions. Contrib. Min. Pet., Vol.48, p.205-219.

Campbell, I.H., Roeder, P.L. and Dixon, J.M. 1978. Plagioclase Buoyancy in Basaltic Liquids as Determined With a Centrifuge Furnace. Contrib. Min. Pet., Vol.67, p.369-377.

Coad, P.R. 1976. The Potter Mine. Unpublished M.Sc. thesis, University of Toronto, 239 p.

Daccord, G., Nittmann, J. and Stanley, H.E. 1986. Radial Viscous Fingers and Diffusion-Limited Aggregation: Fractal Dimension and Growth Sites. Phys. Rev. Let., Vol.56, No.4, p.336-339.

Daccord, G. and Lenormand, R. 1987. Fractal Patterns from Chemical Dissolution. Nature, Vol.325, No.6099, p.41-43.

Deer, W.A., Howie, R.A. and Zussman, J. 1966. An Introduction to the Rock-Forming Minerals. Longman Group Limited, John Wiley and Sons, U.S.A., 528 p.

Dimroth, E. and Dressler, B. 1978. Metamorphism of the Labrador Trough. In Metamorphism in the Canadian Shield, Geol. Surv. Can., Paper 78-10, p.215-236.

Dingwell, D.B. and Mysen, B.O. 1985. Effects of Water and Fluorine on the Viscosity of Albite Melt at High Pressure: a Preliminary Investigation. Earth and Plan. Sci. Let., Vol.74, p.266-274.

Dingwell, D.B., Brearley, M. and Dickinson, J.E. 1988. Melt Densities in the Na_2O-FeO-Fe_2O_3-SiO_2 System and the Partial Molar Volume of Tetrahedrally-Coordinated Ferric Iron in Silicate Melts. Geochim. Cosmochim. Acta, Vol.52, p.2467-2475.

Donaldson, C.H. 1974. Olivine Crystal Types in Harrisitic Rocks of the Rhum Pluton and in Archean Spinifex Rocks. Geol. Soc. Am. Bull., Vol.85, p.1721-1726.

———, 1976. An Experimental Investigation of Olivine Morphology. Contrib. Min. Pet., Vol.57, p.187-213.

———, 1977. Laboratory Duplication of Comb Layering in the Rhum Pluton. Min. Mag., Vol.41, p.323-336.

———, 1982a. Origin of some of the Rhum Harrisite by Segregation of Intercumulus Liquid. Min. Mag., Vol.45, p.201-209.

———, 1982b. Spinifex-textured Komatiites: a Review of Textures, Compositions and Layering. In Komatiites, Arndt, N.T., and Nisbet, E.G. (Eds.), George Allen and Unwin, London, Chap.16, p.213-244.

Dowty, E. 1980. Crystal Growth and Nucleation Theory and the Numerical Simulation of Igneous Crystallization. In Physics of Magmatic Processes, Hargraves, R.B. (Ed.), Princeton University Press, New Jersey, U.S.A., p.419-485.

Dunham, A.C. and Wadsworth, W.J. 1978. Cryptic Variation in the Rhum Layered Intrusion. Min. Mag., Vol.42, p.347-356.

Dunn, T. 1983. Oxygen Chemical Diffusion in Three Basaltic Liquids at Elevated Temperatures and Pressures. Geochim. Cosmochim. Acta, Vol.47, p.1923-1930.

Eakins, P. 1972. Roquemaure Township, Abitibi-West County. Quebec Dept. Nat. Res., Geol. Report 150, 69 p.

Emeleus, C.H. 1987. The Rhum Layered Complex, Inner Hebrides, Scotland. In Origins of Igneous Layering, Parsons, I. (Ed.), D. Reidel Publishing Company, Holland, p.263-286.

Fenn, P.M. 1977. The Nucleation and Growth of Alkali Feldspars from Hydrous Melts. Can. Min., Vol.15, Part 2, p.135-161.

Fleet, M.E. and MacRae, N.D. 1975. A Spinifex Rock from Munro Township, Ontario. Can. J. Earth Sci., Vol.12, p.928-939.

Fowler, A.D. 1990. Self-Organized Mineral Textures of Igneous Rocks: the Fractal Approach. Earth-Sci. Rev., Vol.29, p.47-55.

Fowler, A.D. and Jensen, L.S. 1989. Quantitative Trace-Element Modelling of the Crystallization History of the Kinojévis and Blake River Groups, Abitibi Greenstone Belt, Ontario. Can. J. Earth Sci., Vol.26, p.1356-1367.

Fowler, A.D., Stanley, H.E. and Daccord, G. 1989a. Disequilibrium Silicate Mineral Textures: Fractal and Non-fractal Features. Nature, Vol.341, No.6238, p.134-138.

Fowler, A.D., Roach, D. and Thériault, R. 1989b. Statistical and Fractal Models of Nonequilibrium Mineral Growth. In Statistical Applications in the Earth Sciences, Agterberg, F.P. and Bonham-Carter, G.F. (Eds.), Geol. Surv. Can., Paper 89-9, p.249-254.

Freeman, P.V. 1954. A Petrological Study of the Munro Asbestos 'A' Orebody, Matheson. Unpublished M.Sc. thesis, McGill University, Montreal, Quebec, 92 p.

Grubb, P.L.C. 1962. Serpentinization and Chrysotile Formation in the Matheson Ultrabasic Belt, Northern Ontario. Econ. Geol., Vol.57, p.1228-1246.

Hendry, N.W. 1951. Chrysotile Asbestos in Munro and Beatty Townships, Ontario. Can. Inst. Min. Met., Vol.54, p.28-35.

Hughes, C.J. 1973. Spilites, Keratophyres, and the Igneous Spectrum. Geol. Mag., Vol.109, Part 6, p.513-527.

Huppert, H.E. and Sparks, R.S.J. 1980. The Fluid Dynamics of a Basaltic Magma Chamber Replenished by Influx of Hot, Dense, Ultrabasic Magma. Contrib. Min. Pet., Vol.75, p.279-289.

Huppert, H.E., Sparks, R.S., Turner, J.S. and Arndt, N.T. 1984. Emplacement and Cooling of Komatiitic Lavas. Nature, Vol.309, p.19-22.

Hyndman, D.W. 1985. Petrology of Igneous and Metamorphic Rocks, Second Edition. International Series in the Earth and Planetary Sciences, McGraw-Hill Book Company, U.S.A., 786 p.

Irvine, T.N. 1980. Magmatic Infiltration Metasomatism, Double-Diffusive Fractional Crystallization, and Adcumulus Growth in the Muscox Intrusion and other Layered Intrusions. In Physics of Magmatic Processes, Hargraves, R.B. (Ed.), Princeton University Press, New Jersey, U.S.A., p.325-383.

———, 1982. Terminology for Layered Intrusions. J. of Petrology, Vol.23, Part 2, p.127-162.

Irvine, T.N. and Smith, C.H. 1967. The Ultramafic Rocks of the Muscox Intrusion. In Ultramafic and Related Rocks, Wyllie, P.J. (Ed.), John Wiley and Sons Inc., New York, U.S.A., p.38-49.

Jackson, E.D. 1961. Primary Textures and Mineral Associations in the Ultramafic Zone of the Stillwater Complex, Montana. U.S. Geol. Surv. Prof. Pap., Vol.358.

Jensen, L.S. 1985. Stratigraphy and Petrogenesis of Archean Metavolcanic Sequences, Southwestern Abitibi Subprovince, Ontario. In Evolution of Archean Supracrustal Sequences, Ayres, L.D., Thurston, P.C., Card, K.D. and Weber, W. (eds.), Geol. Ass. Can. Sp. Paper 28, p.65-87.

Jensen, L.S. and Langford, F.F. 1983. Geology and Petrogenesis of the Archean Abitibi Belt in the Kirkland Lake Area, Ontario. Ont. Geol. Surv. Open File Report 5455, 520 p.

Johnstone, R.M. 1987. Geology of the Stoughton-Roquemaure Group, Beatty and Munro Townships, Northeastern Ontario. Unpublished M.Sc. thesis, University of Carleton, Ottawa, Ontario, 244 p.

Jolly, W.T. 1978. Metamorphic History of the Archean Abitibi Belt. In Metamorphism in the Canadian Shield, Fraser, G.A. and Heywood, W.W. (eds.), Geol. Surv. Can. Paper 78-10, p.63-78.

Kirkpatrick, R.J. 1974. A Kinetic Model for Magma Crystallization. Trans. Am. Geophys. Union, Vol.55, p.486.

———, 1975. Crystal Growth from the Melt: A Review. Am. Min., Vol.60, p.798-814.

Kirkpatrick, R.J., Gilpin, R.R. and Hays, J.F. 1976. Kinetics of Crystals Growth from Silicate Melts: Anorthite and Diopside. J. of Geophys. Res., Vol.81, p.2565-2571.

Kozu, S. and Ueda, J. 1933. Thermal Expansion of Plagioclase. Proc. Imp. Acad. Japan, Vol.9, p.262-264.

Kretz, R. 1983. Symbols for Rock-forming Minerals. Am. Min., Vol.68, p.277-279.

———, 1986. Metamorphism. Laboratory manual for the course GEO 3142, Department of Geology, University of Ottawa, Ottawa, 284 p.

Kretz, R., Hartree, R., Garrett, D. and Cermignani, C. 1985. Petrology of the Grenville Swarm of Gabbro Dikes, Canadian Precambrian Shield. Can. J. Earth Sci., Vol.22, No.1, p.53-71.

Kushiro, I., Yoder, H.S. and Mysen, B.O. 1976. Viscosities of basalt and andesite melts at high pressures. J. of Geophys. Res., Vol.81, p.6351-6356.

Lajoie, J. and Gélinas, L. 1978. Emplacement of Archean Peridotitic Komatiites in Lamotte Township, Québec. Can. J. Earth Sci., Vol.15, p.672-677.

Lavenda, B.H. 1985. Brownian Motion. Sci. Am., Vol.252, No.2, p.70-85.

Lofgren, G.E. 1974. An Experimental Study of Plagioclase Crystal Morphology: Isothermal Crystallization. Am. J. Sci., Vol.274, p.243-273.

———, 1975. Dynamic Crystallization Experiments on Mare Basalts. In Origins of Mare Basalts and Their Implications for Lunar Evolution, Lunar Science Institute, Houston, p.99-103.

———, 1980. Experimental Studies on the Dynamic Crystallization of Silicate Melts. In Physics of Magmatic Processes, Princeton University Press, Chap.11, p.487-551.

———, 1983. Effect of Heterogeneous Nucleation on Basaltic Textures: A Dynamic Crystallization Study. J. of Petrology, Vol.24, Part 3, p.229-255.

Lofgren, G.E., Smith, D.P. and Brown, R.W. 1978. Dynamic Crystallization and Kinetic Melting of the Lunar Soil. Proc. Lunar Planet. Sci. Conf. 9th, p.959-975.

Maaloe, S. 1978. The Origin of Rhythmic Layering. Min. Mag., Vol.42, p.337-345.

MacRae, N.D. 1963. Petrology of the Centre Hill Complex, Northern Ontario. Unpublished M.Sc. thesis, McMaster University, Hamilton, Ontario, 102 p.

———, 1965. Petrology and Geochemistry of Ultramafic Gabbroic Intrusions in the Abitibi Area, Ontario. Ph.D. thesis, McMaster University, Hamilton, Ontario.

———, 1969. Ultramafic intrusions of the Abitibi Area, Ontario. Can. J. Earth Sci., Vol.6, p.281-303.

MacRae, N.D. and Crockett, J.H. 1977. The Distribution of Gold and some Platinum Group Elements in Selected Komatiitic Ultramafic Volcanics from Munro Township, Ontario. In Programs with Abstracts, GAC/MAC Annual Meeting, Vol.2, p.34.

Mandelbrot, B.B. 1982. The Fractal Geometry of Nature. W.H. Freeman Company, New York, 468 p.

McBirney, A.R. and Noyes, R.M. 1979. Crystallization and Layering of the Skaergaard Intrusion. J. of Petrology, Vol.20, Part 3, p.487-554.

McCallum, I.S., Raedeke, L.D. and Mathez, E.A. 1980. Investigations of the Stillwater Complex: Part 1. Stratigraphy and Structure of the Banded Zone. Am. J. Sci., Vol.280-A, p.59-87.

Meakin, P. 1983. Diffusion-Controlled Deposition on Fibers and Surfaces. Phys. Rev. A, Vol.27, No.5, p.2616-2623.

Morimoto, N. 1989. Nomenclature of Pyroxenes. Can. Min., Vol.27, p.143-156.

Morse, S.A. 1980. Basalts and Phase Diagrams: An Introduction to the Quantitative Use of Phase Diagrams in Igneous Petrology. Springer-Verlag, New York, U.S.A., 493 p.

Mullins, W.W. and Sekerka, J. 1963. Morphological Stability of a Particle Growing by Diffusion or Heat Flow. J. of Appl. Phys., Vol.34, No.2, p.323-329.

Muncill, G.E. and Lasaga, A.C. 1988. Crystal-Growth Kinetics of Plagioclase in Igneous Systems: Isothermal H_2O-Saturated Experiments and Extension of a Growth Model to Complex Silicate Melts. Am. Min., Vol.73, p.982-992.

Mysen, B.O., Virgo, D., Scarfe, C.M. and Cronin, D.J. 1985. Viscosity and Structure of Iron- and Aluminum-Bearing Calcium Silicate Melts at 1 Atmosphere. Am. Min., Vol.70, p.487-498.

Nittmann, J. and Stanley, H.E. 1986. Tip Splitting Without Interfacial Tension and Dendritic Growth Patterns Arising from Molecular Anisotropy. Nature, Vol.321, p.663-668.

Petersen, J.S. 1985. Columnar-dendritic Feldspars in the Lardalite Intrusion, Oslo Region, Norway: 1. Implications for Unilateral Solidification of a Stagnant Boundary Layer. J. of Petrology, Vol.26, Part 1, p.223-252.

Pyke, D.R. 1976. On the Relationship between Gold Mineralization and Ultramafic Rocks in the Timmins Area, Northeastern Ontario. Can. Inst. Min. Met. Bull., Vol.69, No.773, p.79-87.

Pyke, D.R., Naldrett, A.J. and Eckstrand, A.P. 1973. Archean Ultramafic Flows in Munro Township, Ontario. Geol. Soc. Am. Bull., Vol.84, p.955-978.

Raedeke, L.D. and McCallum, I.S. 1984. Investigations in the Stillwater Complex: Part II. Petrology and Petrogenesis of the Ultramafic Series. J. of Petrology, Vol.25, Part 2, p.395-420.

Robins, B. 1973. Crescumulate Layering in a Gabbroic Body on Seiland, northern Norway. Geol. Mag., Vol.109, Part 6, p.533-542.

Robins, B., Haukvik, L. and Jansen, S. 1987. The Organization and Internal Structure of Cyclic Units in the Honningsvag Intrusive Suite, North Norway: Implications for Intrusive Mechanisms, Double-Diffusive Convection and Pore-Magma Infiltration. In Origins of Igneous Layering, Parsons, I. (Ed.), D. Reidel Publishing Company, Holland, p.287-312.

Sander, L.M. 1986. Fractal Growth Processes. Nature, Vol.322, No.6082, p.789-793.

Satterly, J. 1952. Geology of Munro Township. Ont. Dept. of Mines, Annual Report for 1951, Vol.60, Part 8, 60 p.

Scarfe, C.M. 1973. Viscosity of Basic Magmas at Varying Pressure. Nature, Vol.241, p.101-102.

———, 1986. Viscosity and Density of Silicate Melts. In MAC Short Course in Silicate Melts, Scarfe, C.M. (Ed.), Vol.12, Chap.2, p.36-56.

Shirley, D.N. 1987. Differentiation and Compaction in the Palisades Sill, New Jersey. J. of Petrology, Vol.28, Part 5, p.835-865.

Skippen, G. 1974. An Experimental Model for Low Pressure Metamorphism of Siliceous Dolomitic Marble. Am. J. Sci., Vol.274, p.487-509.

Spohn, T., Hort, M. and Fischer, H. 1988. Numerical Simulation of the Crystallization of Multicomponent Melts in Thin Dikes or Sills: 1. The Liquidus Phase. J. of Geophys. Res., Vol.93, No.B5, p.4880-4894.

Swanson, S.E. 1977. Relation of Nucleation and Crystal Growth Rate to the Development of Granitic Textures. Am. Min., Vol.62, p.966-978.

Swanson, S.E. and Fenn, P.M. 1986. Quartz Crystallization in Igneous Rocks. Am. Min., Vol.71, p.331-342.

Swinden, H.S. 1987. Ordovician Volcanism and Mineralization in the Wild Bight Group, Central Newfoundland: A Geological, Petrological, Geochemical and Isotopic Study. Unpublished Ph.D. thesis, Memorial University of Newfoundland, St. John's, Newfoundland.

Taubeneck, W.H. and Poldervaart, A. 1960. Geology of the Elkhorn Mountains, Northeastern Oregon: Part 2. Willow Lake Intrusion. Bull. Geol. Soc. Am., Vol.71, p.1295-1322.

Taylor, F.C. 1955. The Petrology of the Serpentine Bodies in the Matheson District, Ontario. Unpublished Ph. D. Thesis, McGill University, Montreal, Quebec.

Turner, F.J. 1981. Metamorphic Petrology: Mineralogical, Field, and Tectonic Aspects. Second Edition. Hemisphere Publishing Corporation, McGraw-Hill Book Company, U.S.A., 524 p.

Viljoen, M.J. and Viljoen, R.P. 1969. Evidence for the Existence of a Mobile Extrusive Peridotitic Magma from the Komati Formation of the Onverwacht Group. Sp. Publ. Geol. Soc. S. Afr., Vol.2, p.27-112.

Wadsworth, W.J. 1961. The Layered Ultrabasic Rocks of Southwest Rhum, Inner Hebrides. Royal Soc. London Philos. Trans., Vol.244, p.21-64.

Wager, L.R., and Brown, G.M. 1951. A Note on Rhythmic Layering in the Ultrabasic Rocks of Rhum. Geol.Mag., Vol.88, p.166-168.

———, 1967. Layered Igneous Rocks. W. H. Freeman and Company, San Francisco, 588 p.

Walker, L.R. 1969. The Palisades Sill, New Jersey: A Reinvestigation. Geol. Soc. Am. Sp. Paper 3, p.1-178.

Walker, R.J., Shirey, S.B. and Stecher, O. 1988. Comparative Re-Os, Sm-Nd and Rb-Sr Isotope and Trace Element Systematics for Archean Komatiite Flows from Munro Township, Abitibi Belt, Ontario. Earth and Plan. Sci. Let., Vol.87, p.1-12.

Watson, E.B. 1981. Diffusion in Magmas at Depth in the Earth: The Effects of Pressure and Dissolved H_2O. Earth and Plan. Sci. Let., Vol.52, p.291-301.

Wicks, F.J., Wan, P. and Hedjran, K. 1984. Mineralogy and Geochemistry of the Chrysotile Asbestos Deposits of Ontario, Munro Mine and Garrison Deposit. In Geoscience Research Grant Program, Summary of Research for 1983-1984, Milne, V.G. (Ed.), Ont. Geol. Surv. Misc. Paper 121, 252 p.

Winkler, H.G.F. 1979. Petrogenesis of Metamorphic Rocks. Fifth Edition. Springer-Verlag New York Inc., U.S.A., 348 p.

Witten, T.A. and Sander, L.M. 1981. Diffusion Limited Aggregation, a Kinetic Critical Phenomenon. Phys. Rev. Let., Vol.47, p.1400-1403.

———, 1983. Diffusion-Limited Aggregation. Phys. Rev. B, Vol.27, No.9, p.5686-5697.

Witten, T.A. and Meakin, P. 1983. Diffusion-Limited Aggregation at Multiple Growth Sites. Phys. Rev. B, Vol.28, No.10, p.5632-5642.

Wyllie, P.J. 1960. The System CaO-MgO-FeO-SiO_2 and its Bearing on the Origin of Ultrabasic and Basic Rocks. Min. Mag., Vol.32, p.459-470.

Yoder, H.S. and Tilley, C.E. 1962. Origin of Basalt Magmas: An Experimental Study of Natural and Synthetic Rock Systems. J. of Petrology, Vol.3, p.342-532.

APPENDIX 1

X-RAY FLUORESCENCE ANALYSES OF MAJOR OXIDES AND TRACE ELEMENTS

Whole rock samples were analysed for major element oxides and trace elements at the University of Ottawa using a Phillips 1410 X-ray fluorescence spectrometer. All analyses were performed by exposing a fused glass disc of the sample to X-rays produced by a Rh α tube. The precision of results in relative % is given below for the major oxides and trace elements.

	abundance (wt.%)	
	0.1-1.0	1.0-100
SiO_2	---	±1.25
Al_2O_3	±10	±1.5
Fe_2O_3	±5	±2
MgO	±25	±3
CaO	±5	±2
Na_2O	±15	±8
K_2O	±5	±1
TiO_2	±2	±1
P_2O_5	±10	±1
MnO	±10	---
S	±10	---

	abundance (ppm)		
	<10	10-30	>30
Ba	±10	±50	±10
Cr	"	"	"
Zr	"	"	"
Sr	"	"	"
Rb	"	"	"
Y	"	"	"
Nb	"	"	"
Zn	"	"	"
Ni	"	"	"
V	"	"	"

Ferrous iron was determined by titration using a solution of ammonium metavanadate. Loss on ignition (LOI) was determined by weighing a powdered sample before and after heating to 1000 °C for 2 hours.

Two samples of marginal gabbro (Mgb-1, Mgb-4) were analysed for Au, Pt and Pd at Bondar-Clegg and Company Ltd. by DC plasma spectroscopy. The lower detection limits are 1 ppb for Au and Pd, and 5 ppb for Pt.

Tables A to E show the results of 24 whole rock analyses along with the mean composition of each rock type. Totals include loss on ignition (LOI). The abbreviation *X* stands for the following weight fraction ratio of oxides ($MgO/MgO+FeO+Fe_2O_3$).

APPENDIX 1

TABLE A. X-ray fluorescence analyses of peridotite.

		Pd-1	Pd-2	Pd-3	Pd-4	Pd-5	Mean
(wt%)	SiO_2	36.64	37.81	37.87	40.92	39.25	38.50
	Al_2O_3	1.39	2.20	1.85	1.31	2.76	1.90
	Fe_2O_3	13.58	10.69	12.59	10.63	10.07	11.51
	FeO	4.41	4.25	5.58	7.75	12.88	6.97
	MgO	29.95	28.86	28.23	27.30	25.44	27.96
	CaO	1.87	3.34	2.93	5.30	4.10	3.51
	Na_2O	0.62	0.34	0.61	0.40	1.29	0.65
	K_2O	-	0.01	-	0.03	0.05	0.02
	TiO_2	0.20	0.27	0.23	0.17	0.33	0.24
	P_2O_5	0.01	-	-	-	0.01	0.00
	MnO	0.22	0.22	0.26	0.25	0.34	0.26
	S	0.02	0.01	0.01	0.01	-	0.01
	LOI	9.33	8.60	8.29	4.59	3.19	6.80
	TOTAL	98.24	96.60	98.45	98.66	99.71	98.33
(ppm)	Ba	22	41	27	55	51	39
	Cr	3760	5030	3170	1950	101	2800
	Zr	<10	<10	<10	22	33	13
	Sr	-	-	-	<10	12	<10
	Y	<10	<10	<10	<10	12	<10
	Zn	98	126	78	85	111	100
	Ni	1530	1540	1450	1150	880	1310
	V	78	112	106	59	79	87
	Fe^{2+}/FeT	0.26	0.31	0.33	0.45	0.59	0.39
	X	0.62	0.65	0.60	0.59	0.51	0.59

APPENDIX 1

TABLE B. X-ray fluorescence analyses of clinopyroxenite.

		Cp-1	Cp-2	Cp-3	Cp-4	Mean
(wt%)	SiO_2	49.18	50.24	49.48	49.72	49.65
	Al_2O_3	3.24	2.97	3.86	5.32	3.85
	Fe_2O_3	2.14	2.05	2.79	2.66	2.41
	FeO	5.06	6.26	8.60	8.43	7.09
	MgO	16.61	16.13	15.32	13.40	15.36
	CaO	19.70	18.03	16.04	15.34	17.28
	Na_2O	0.71	0.66	0.96	1.48	0.95
	K_2O	-	0.03	0.04	0.06	0.03
	TiO_2	0.44	0.45	0.54	0.74	0.54
	P_2O_5	-	-	-	-	-
	MnO	0.17	0.17	0.20	0.21	0.19
	S	-	-	0.01	-	-
	LOI	1.80	1.23	1.33	1.00	1.34
	TOTAL	99.05	98.22	99.17	98.36	98.70
(ppm)	Ba	59	43	57	41	50
	Cr	2440	2050	762	255	1380
	Zr	14	10	19	25	17
	Sr	<10	19	<10	29	16
	Y	10	<10	15	15	12
	Zn	24	33	42	46	36
	Ni	1080	353	399	231	516
	V	190	212	252	338	248
	Fe^{+2}/FeT	0.72	0.77	0.77	0.78	0.76
	X	0.68	0.64	0.55	0.53	0.60

APPENDIX 1

TABLE C. X-ray fluorescence analyses of marginal gabbro.

		Mgb-1	Mgb-2	Mgb-3	Mgb-4	Mgb-5	Mean
(wt%)	SiO_2	49.51	50.66	49.22	49.29	51.80	50.10
	Al_2O_3	8.34	9.41	9.82	9.14	9.18	9.18
	Fe_2O_3	3.01	2.94	3.43	3.20	2.85	3.09
	FeO	9.03	9.21	9.95	9.59	8.49	9.25
	MgO	11.43	9.94	9.92	9.57	8.11	9.79
	CaO	10.10	10.34	9.02	11.71	11.23	10.48
	Na_2O	2.31	3.02	2.90	2.37	3.48	2.82
	K_2O	0.18	0.07	0.07	0.07	0.12	0.10
	TiO_2	1.07	1.16	1.18	1.09	1.09	1.12
	P_2O_5	0.05	0.05	0.08	0.06	0.03	0.05
	MnO	0.22	0.21	0.17	0.20	0.15	0.19
	S	0.01	0.06	0.02	0.01	-	0.02
	LOI	1.81	1.50	2.63	1.59	2.29	1.96
	TOTAL	97.07	98.57	98.41	97.89	98.82	98.15
(ppm)	Ba	73	38	43	76	43	55
	Cr	462	573	399	731	246	482
	Zr	63	69	69	60	63	65
	Sr	134	131	123	125	83	119
	Y	21	19	22	19	18	20
	Zn	107	45	46	79	26	61
	Ni	124	155	108	176	116	135
	V	258	294	293	286	273	281
(ppb)	Au	207	-	-	211	-	-
	Pt	<5	-	-	27	-	-
	Pd	<1	-	-	15	-	-
	Fe^{+2}/FeT	0.77	0.78	0.76	0.77	0.77	0.77
	X	0.47	0.43	0.41	0.41	0.40	0.42

APPENDIX 1

TABLE D. X-ray fluorescence analyses of branches of BTG.

		Br-1	Br-2	Br-3	Br-4	Br-5	Mean
(wt%)	SiO_2	43.44	42.24	43.05	43.61	43.72	43.21
	Al_2O_3	13.43	14.17	13.95	14.34	14.79	14.14
	Fe_2O_3	6.73	8.22	8.99	5.92	6.43	7.26
	FeO	15.85	15.41	14.80	13.02	13.07	14.43
	MgO	4.29	3.99	4.31	3.93	4.72	4.25
	CaO	7.38	7.11	7.11	8.51	9.49	7.92
	Na_2O	2.76	2.49	2.83	2.50	2.25	2.57
	K_2O	0.29	0.21	0.28	0.09	0.10	0.19
	TiO_2	2.01	1.95	2.09	1.16	1.43	1.73
	P_2O_5	0.08	0.10	0.10	0.15	0.12	0.11
	MnO	0.35	0.34	0.36	0.24	0.25	0.31
	S	0.01	-	-	0.01	0.02	0.01
	LOI	2.11	2.14	1.91	2.28	2.23	2.14
	TOTAL	98.73	98.37	99.78	95.76	98.62	98.26
(ppm)	Ba	41	46	58	<10	13	33
	Cr	35	34	27	33	30	32
	Zr	88	86	88	118	93	95
	Sr	240	211	229	236	256	234
	Y	29	28	29	31	33	30
	Nb	-	<10	<10	-	<10	<10
	Zn	105	132	107	90	94	106
	Ni	27	22	18	27	41	27
	V	291	250	311	126	224	240
	Fe^{+2}/FeT	0.72	0.68	0.65	0.71	0.69	0.69
	X	0.16	0.14	0.15	0.17	0.19	0.16

APPENDIX 1

TABLE E. X-ray fluorescence analyses of matrix of BTG.

		Mtx-1	Mtx-2	Mtx-3	Mtx-4	Mtx-5	Mean
(wt%)	SiO_2	53.64	52.18	55.98	57.04	53.81	54.53
	Al_2O_3	13.62	13.09	14.29	12.98	13.20	13.44
	Fe_2O_3	3.52	3.85	4.02	3.27	2.39	3.41
	FeO	9.92	10.17	8.31	9.16	10.36	9.58
	MgO	3.73	4.10	2.22	3.06	4.15	3.45
	CaO	7.33	7.79	5.99	6.65	6.96	6.94
	Na_2O	4.52	4.31	5.79	4.67	4.32	4.72
	K_2O	0.42	0.50	0.20	0.38	0.29	0.36
	TiO_2	1.73	1.90	1.28	1.67	1.75	1.67
	P_2O_5	0.10	0.07	0.15	0.11	0.11	0.11
	MnO	0.20	0.21	0.20	0.22	0.22	0.21
	S	0.01	0.07	0.03	0.02	0.02	0.03
	LOI	0.83	0.85	0.48	0.63	1.27	0.81
	TOTAL	99.57	99.09	98.94	99.86	98.85	99.26
(ppm)	Ba	112	137	89	103	92	107
	Cr	23	31	31	41	35	32
	Zr	147	125	167	152	138	146
	Sr	272	281	313	293	217	275
	Rb	<10	<10	-	<10	<10	<10
	Y	40	38	44	42	42	41
	Nb	<10	<10	<10	<10	11	<10
	Zn	78	64	51	74	63	66
	Ni	28	38	15	20	38	28
	V	197	266	37	162	176	168
	Fe^{+2}/FeT	0.76	0.75	0.70	0.76	0.83	0.76
	X	0.22	0.23	0.15	0.20	0.25	0.21

APPENDIX 2

ELECTRON MICROPROBE MINERAL ANALYSES

The chemical composition of clinopyroxene, plagioclase, actinolite, tremolite, Fe-Ti oxides, epidote and olivine was analyzed at McGill University using a CAMECA MB1 electron microprobe with four wavelength dispersive spectrometers.

The analyses were performed using a beam current of 8 Na and an accelerating voltage of 15 Kv. The counting time was set at 25 seconds. Standards used for calibration are andradite, pyrophanite, albite, diopside and orthoclase. The accuracy of the totals was approximated at 1% under these analytical conditions.

Tables A to E show the results of 94 mineral analyses which have been all recalculated to a total of 100 wt.%. The abbreviations *X* and *An* stand for the Mg number ($MgO/MgO+FeO+Fe_2O_3$) and the anorthite content of plagioclase (mole ratio An/An+Ab), respectively. Sample numbers are given for mineral analyses from peridotite, clinopyroxenite and marginal gabbro.

APPENDIX 2

TABLE A. Mineral analyses from peridotite layers.

	OLIVINE		CLINOPYROXENE						TREMOLITE				
	ol-1	ol-2	cpx-1	cpx-2	cpx-3	cpx-4	cpx-5	cpx-6	tr-1	tr-2	tr-3	tr-4	tr-5
SiO_2	37.30	37.08	53.57	53.61	54.08	52.02	52.99	53.03	58.60	58.37	57.51	57.98	58.05
Al_2O_3	0.02	0.03	1.70	1.22	0.30	1.22	1.43	1.34	0.35	0.40	0.21	0.15	0.67
FeOT	25.95	26.56	5.14	5.23	4.38	6.56	7.13	6.98	2.47	2.57	2.88	2.89	2.91
MgO	35.97	35.74	17.68	17.93	17.07	16.27	16.90	16.99	23.28	23.44	25.25	23.66	23.53
MnO	0.52	0.40	0.07	0.14	0.10	0.32	0.20	0.15	0.07	0.06	0.09	0.12	0.12
CaO	0.23	0.18	21.20	21.40	23.81	22.84	20.82	20.98	12.83	12.72	11.61	12.61	12.43
Na_2O	-	-	0.33	0.27	0.22	0.35	0.25	0.24	0.13	0.16	0.13	0.28	0.03
K_2O	-	0.01	0.01	-	-	-	-	-	0.02	0.02	0.08	0.08	0.02
TiO_2	0.01	-	0.30	0.20	0.04	0.42	0.28	0.29	0.05	0.06	0.04	0.04	0.05
H_2O	-	-	-	-	-	-	-	-	2.20	2.20	2.20	2.19	2.19
X	0.71	0.71	0.86	0.86	0.87	0.82	0.81	0.81	0.94	0.94	0.94	0.94	0.94
sample	Pd-5	Pd-5	Pd-1	Pd-3	Pd-3	Pd-3	Pd-5	Pd-5	Pd-1	Pd-1	Pd-3	Pd-3	Pd-4

TABLE B. Mineral analyses from clinopyroxenite layers.

	CLINOPYROXENE								
	cpx-7	cpx-8	cpx-9	cpx-10	cpx-11	cpx-12	cpx-13	cpx-14	cpx-15
SiO_2	52.81	54.32	53.66	54.10	52.53	53.51	53.34	53.23	53.32
Al_2O_3	1.95	0.92	0.95	0.89	2.13	0.54	1.09	1.19	1.12
FeOT	6.16	5.10	5.66	4.83	5.94	7.25	6.34	6.86	6.91
MgO	17.48	18.49	18.50	18.37	17.18	15.61	17.63	17.28	17.06
MnO	0.11	0.13	0.20	0.12	0.08	0.20	0.18	0.16	0.23
CaO	20.78	20.58	20.59	21.21	21.27	22.27	20.91	20.82	20.82
Na_2O	0.27	0.25	0.23	0.32	0.36	0.50	0.23	0.16	0.22
K_2O	-	-	-	0.02	-	0.01	-	-	0.03
TiO_2	0.43	0.21	0.21	0.14	0.51	0.11	0.28	0.30	0.29
X	0.83	0.87	0.85	0.87	0.84	0.79	0.83	0.82	0.82
sample	Cp-1	Cp-1	Cp-1	Cp-2	Cp-2	Cp-3	Cp-3	Cp-4	Cp-4

APPENDIX 2

TABLE C. Mineral analyses from marginal gabbro.

	CLINOPYROXENE			
	cpx-16	cpx-17	cpx-18	cpx-19
SiO_2	51.56	52.93	53.31	53.06
Al_2O_3	3.07	2.39	1.59	1.89
FeOT	8.31	6.84	6.18	6.94
MgO	15.67	17.28	17.64	17.23
MnO	0.20	0.20	0.13	0.20
CaO	20.28	19.55	20.59	20.05
Na_2O	0.31	0.30	0.27	0.24
K_2O	-	-	-	-
TiO_2	0.60	0.51	0.29	0.39
X	0.77	0.82	0.84	0.82
sample	Mgb-3	Mgb-3	Mgb-1	Mgb-1

TABLE D. Mineral analyses from matrix of BTG.

	CLINOPYROXENE											
	cpx-20	cpx-21	cpx-22	cpx-23	cpx-24	cpx-25	cpx-26	cpx-27	cpx-28	cpx-29	cpx-30	cpx-31
SiO_2	51.07	50.59	51.68	50.94	50.98	51.65	51.00	50.89	50.95	50.63	50.79	50.23
Al_2O_3	1.81	1.67	0.27	1.38	1.45	0.25	1.56	1.84	1.47	1.25	2.06	1.59
FeOT	13.89	15.71	16.60	15.22	15.52	16.39	16.32	14.29	15.31	17.45	12.68	16.89
MgO	13.85	12.33	10.10	12.20	12.46	10.29	11.98	12.78	12.63	11.60	13.89	10.97
MnO	0.32	0.45	0.43	0.39	0.40	0.48	0.34	0.35	0.28	0.35	0.37	0.47
CaO	18.27	18.33	20.52	19.00	18.19	20.52	17.88	19.01	18.63	18.01	19.26	18.79
Na_2O	0.3[illegible]	0.42	0.38	0.42	0.48	0.30	0.44	0.29	0.27	0.30	0.32	0.41
K_2O	0.03	0.03	0.02	0.05	0.06	0.06	0.05	0.01	-	-	0.01	0.03
TiO_2	0.46	0.47	-	0.40	0.46	0.06	0.43	0.54	0.46	0.41	0.62	0.62
X	0.64	0.58	0.52	0.59	0.59	0.53	0.57	0.61	0.60	0.54	0.66	0.54

APPENDIX 2

TABLE D. Mineral analyses from matrix of BTG (continued).

	CLINOPYROXENE			PLAGIOCLASE									
	cpx-32	cpx-33	cpx-34	pl-1	pl-2	pl-3	pl-4	pl-5	pl-6	pl-7	pl-8	pl-9	pl-10
SiO_2	50.23	50.12	49.66	65.96	67.76	67.16	67.25	68.09	68.14	67.17	66.84	66.91	66.81
Al_2O_3	1.51	1.58	0.78	21.38	20.05	20.26	20.22	19.59	19.50	20.34	20.21	20.63	20.69
FeOT	17.02	17.63	22.21	0.09	0.06	0.16	0.03	0.05	0.02	0.05	0.05	0.06	0.04
MgO	11.37	11.05	7.42	0.01	0.02	0.02	0.01	-	0.02	-	-	-	0.01
MnO	0.36	0.38	0.51	0.06	-	-	-	-	0.03	0.02	-	-	0.02
CaO	18.63	18.33	18.78	1.10	0.36	1.16	0.73	0.77	0.43	0.60	0.59	1.13	1.27
Na_2O	0.30	0.32	0.29	11.29	11.69	11.18	11.68	11.43	11.58	11.71	12.19	11.07	11.03
K_2O	0.02	0.01	-	0.11	0.06	0.06	0.08	0.07	0.28	0.11	0.12	0.19	0.13
TiO_2	0.56	0.58	0.35	-	-	-	-	-	-	-	-	0.01	-
X/An	0.54	0.53	0.37	5.08	1.65	5.38	3.34	3.58	1.98	2.74	2.53	5.24	5.90

	ACTINOLITE							Fe-Ti OXIDE			
	act-1	act-2	act-3	act-4	act-5	act-6	act-7	oxi-1	oxi-2	oxi-3	oxi-4
SiO_2	49.27	51.82	48.30	47.43	49.26	47.28	50.29	0.14	0.11	0.13	0.12
Al_2O_3	2.60	0.69	3.72	5.54	3.55	5.55	1.60	0.22	0.42	2.40	0.26
Cr_2O_3	-	-	-	-	-	-	-	1.81	0.91	-	0.38
Fe_2O_3	-	-	-	-	-	-	-	14.29	44.27	55.45	55.60
FeO	28.59	25.46	25.67	24.08	25.88	26.50	27.09	38.13	24.88	36.26	36.81
MgO	7.87	7.63	7.25	7.99	7.01	6.24	7.00	0.01	0.04	0.03	0.05
MnO	0.91	0.52	0.55	0.44	0.52	0.44	0.56	1.93	1.14	0.21	0.20
CaO	7.51	11.30	11.45	11.16	10.94	10.93	11.04	-	0.01	0.02	0.05
Na_2O	0.85	0.43	0.52	0.83	0.65	0.83	0.29	-	-	-	-
K_2O	0.09	0.11	0.16	0.33	0.10	0.17	0.03	-	-	-	-
TiO_2	0.10	0.08	0.44	0.22	0.14	0.13	0.16	43.47	28.22	5.50	6.53
H_2O	1.94	1.96	1.95	1.96	1.95	1.94	1.94	-	-	-	-
X	0.33	0.35	0.33	0.37	0.33	0.30	0.32	-	-	-	-

APPENDIX 2

TABLE E. Mineral analyses from branches of BTG.

	ACTINOLITE												
	act-8	act-9	act-10	act-11	act-12	act-13	act-14	act-15	act-16	act-17	act-18	act-19	act-20
SiO_2	53.30	50.87	47.77	48.52	52.37	50.52	46.64	47.65	47.70	45.80	50.90	52.10	51.62
Al_2O_3	1.93	3.59	5.66	5.66	2.80	3.32	7.48	6.98	6.74	6.74	3.43	2.70	2.98
FeOT	19.18	22.78	27.63	26.83	18.64	24.32	26.12	22.89	23.17	24.62	25.20	22.31	22.84
MgO	10.57	7.72	8.15	8.09	11.07	6.82	6.13	6.97	6.70	5.14	6.40	8.40	7.76
MnO	0.58	0.45	0.81	0.66	0.42	0.43	0.59	0.30	0.44	0.42	0.44	0.42	0.40
CaO	12.02	11.52	7.03	7.29	11.96	11.78	9.87	11.72	11.36	11.01	10.90	11.40	11.67
Na_2O	0.25	0.65	0.67	0.67	0.41	0.55	0.82	1.05	1.42	1.79	0.57	0.50	0.55
K_2O	0.04	0.12	0.11	0.10	0.13	0.12	0.15	0.30	0.26	0.34	0.08	0.08	0.11
H_2O	2.05	2.01	1.99	2.00	2.05	1.99	1.98	2.00	2.00	1.98	2.00	2.02	2.01
TiO_2	0.07	0.29	0.18	0.17	0.14	0.14	0.21	0.16	0.32	0.15	0.08	0.06	0.05
X	0.50	0.38	0.34	0.35	0.51	0.33	0.30	0.35	0.34	0.27	0.31	0.40	0.38

	PLAGIOCLASE						CLINOPYROXENE					
	pl-11	pl-12	pl-13	pl-14	pl-15	pl-16	cpx-35	cpx-36	cpx-37	cpx-38	cpx-39	cpx-40
SiO_2	66.11	67.24	67.63	62.69	67.12	65.91	51.21	50.33	50.28	50.31	50.63	50.38
Al_2O_3	21.52	20.89	19.98	23.19	19.96	20.23	1.97	1.41	2.59	2.05	1.45	1.40
FeOT	0.11	0.25	0.07	0.56	0.37	0.79	12.60	15.25	15.19	14.59	16.16	16.14
MgO	0.02	-	-	0.11	-	0.10	14.08	13.38	11.89	12.28	11.36	11.68
MnO	0.01	0.05	0.03	0.01	-	0.03	0.30	0.45	0.45	0.40	0.35	0.38
CaO	1.23	0.74	0.73	2.88	1.18	1.95	18.91	18.35	18.75	19.42	19.27	18.99
Na_2O	10.00	10.76	11.49	9.21	11.30	10.84	0.35	0.33	0.37	0.34	0.33	0.52
K_2O	0.08	0.07	0.07	1.31	0.07	0.14	0.02	0.02	0.01	0.01	0.03	0.02
TiO_2	0.02	-	-	0.04	-	0.01	0.56	0.48	0.47	0.60	0.42	0.49
An/X	5.82	3.64	3.36	13.67	5.46	8.96	0.67	0.61	0.58	0.60	0.56	0.56

APPENDIX 2

TABLE E. Mineral analyses from branches of BTG (continued).

	CLINOPYROXENE			EPIDOTE		Fe-Ti OXIDE			
	cpx-41	cpx-42	cpx-43	ep-1	ep-2	oxi-5	oxi-6	oxi-7	oxi-8
SiO_2	53.30	50.87	47.77	38.32	37.95	0.01	0.04	-	0.03
Al_2O_3	1.93	3.59	5.66	23.08	23.66	-	0.04	0.01	0.05
Cr_2O_3	-	-	-	-	-	1.44	1.24	2.98	1.47
Fe_2O_3	-	-	-	13.11	15.02	6.11	4.87	4.30	5.98
FeO	19.18	22.78	27.63	-	0.03	42.06	42.43	41.86	41.66
MgO	10.57	7.72	8.15	-	-	0.02	0.03	0.02	-
MnO	0.58	0.45	0.81	0.18	0.24	2.02	2.21	2.73	2.42
CaO	12.02	11.52	7.03	23.12	20.42	0.02	0.08	-	0.14
Na_2O	0.25	0.65	0.67	0.20	0.70	-	-	-	-
K_2O	0.04	0.12	0.11	-	-	-	-	-	-
TiO_2	0.07	0.29	0.18	0.10	0.09	48.32	49.06	48.10	48.25
H_2O	-	-	-	1.89	1.89	-	-	-	-
X	0.50	0.38	0.34	-	-	-	-	-	-

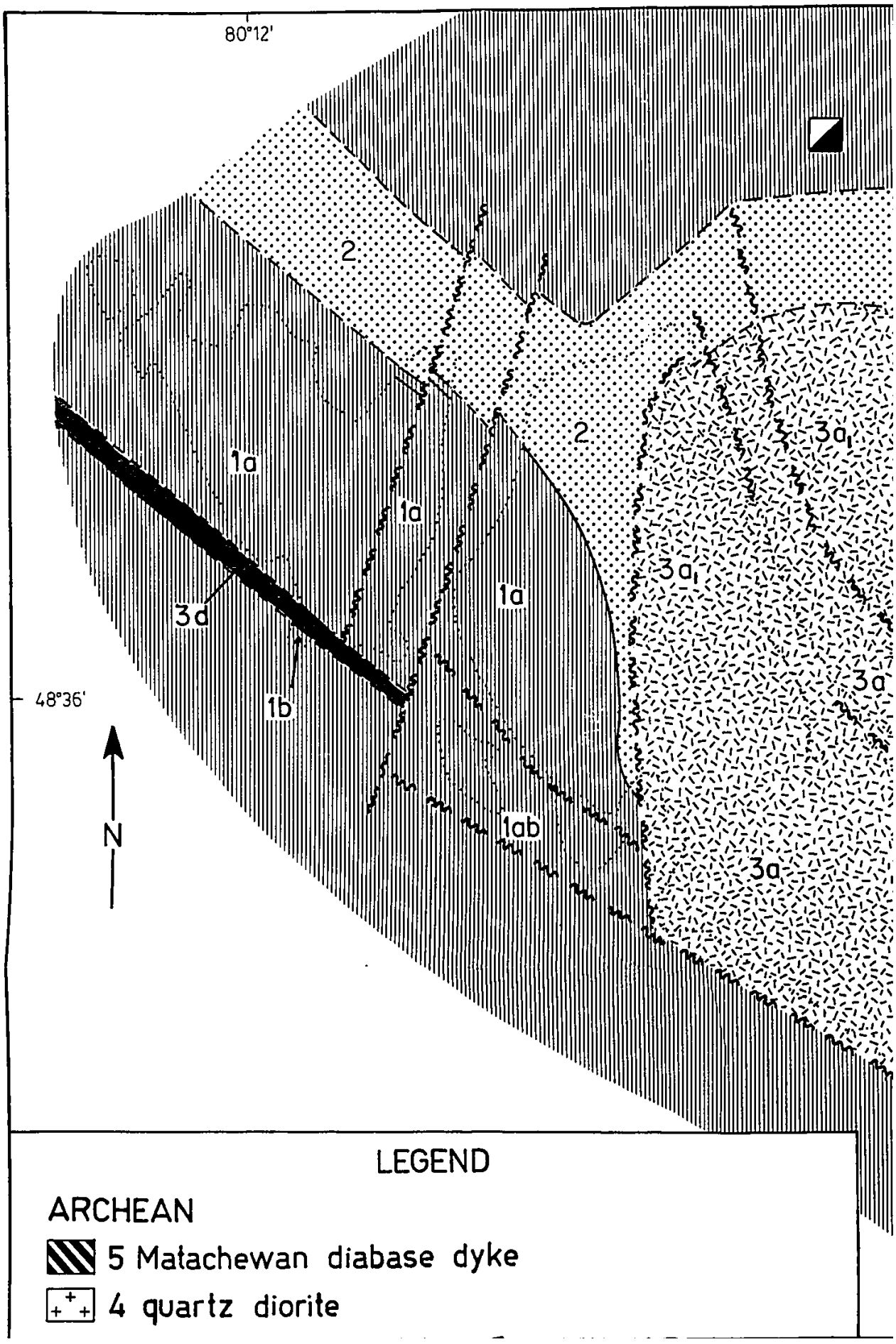
80°12'
48°36'
N
2
2
1a
1a
1a
1ab
1b
3d
3a1
3a1
3a
3a
LEGEND
ARCHEAN
5 Matachewan diabase dyke
4 quartz diorite

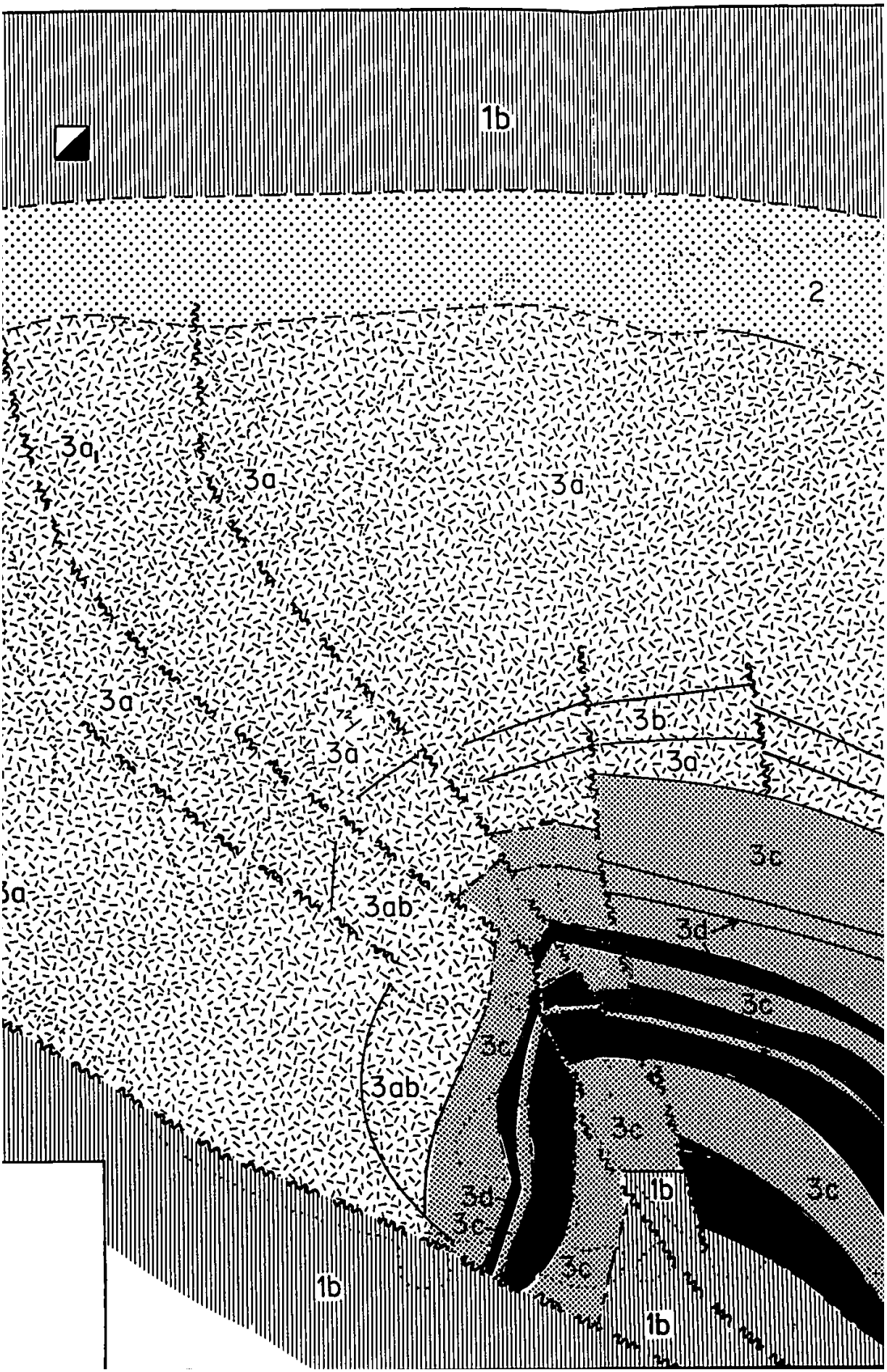
1b
2
3a
3a
3a
3a
3a
3a
3b
3a
3c
3d
3c
3c
3ab
3ab
3c
3c
3a
3c
3c
1b
1b
1b
1b


2
5
3b
3a
3c
3d
3d
3c
3c
3ab
3c
1b
3c
1b
5

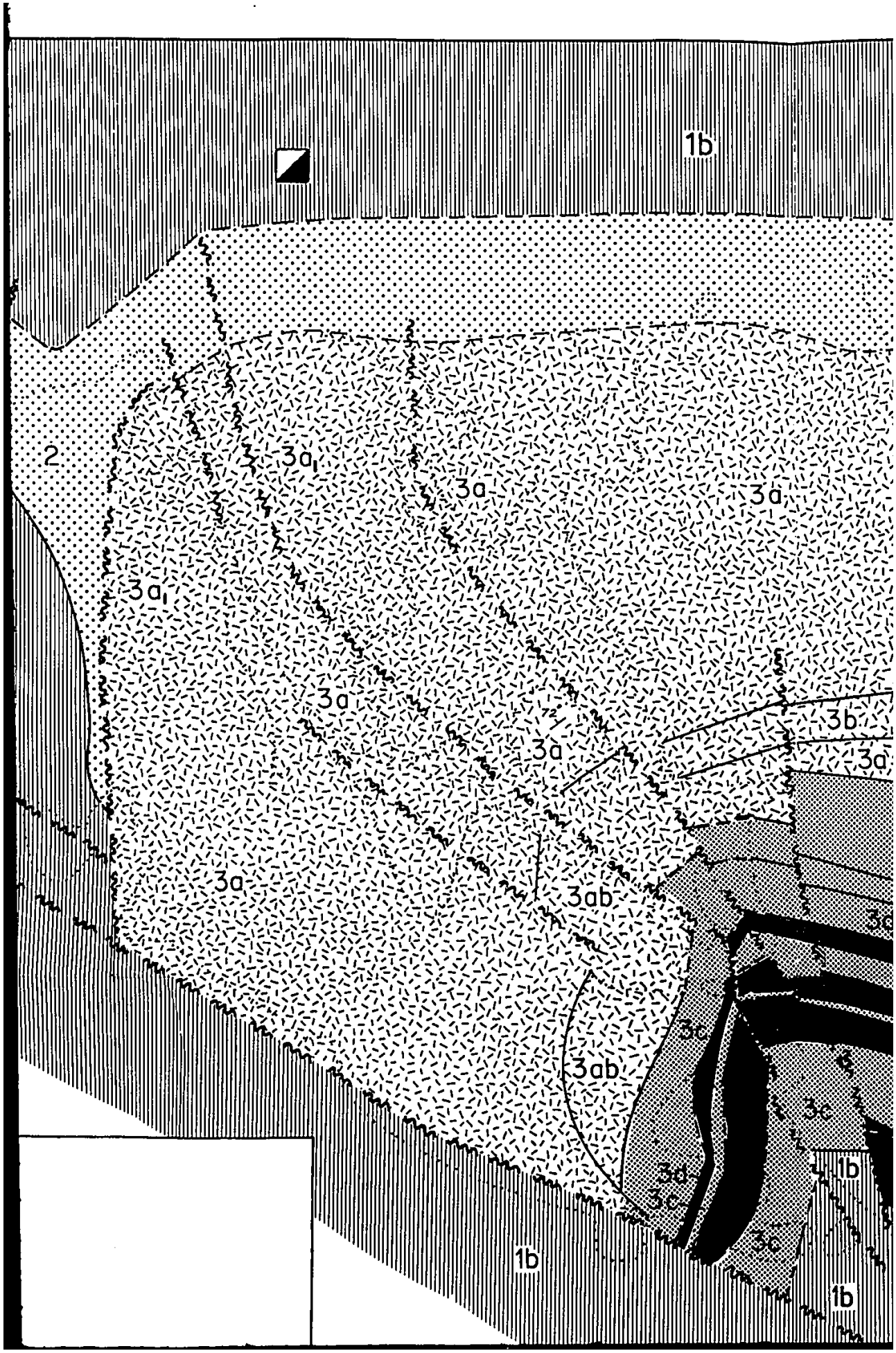
1b
2
3a1
3a
3a1
3a
3a
3a
3b
3a
3a
3ab
3c
3c
3ab
3c
3a
3c
1b
1b
1b

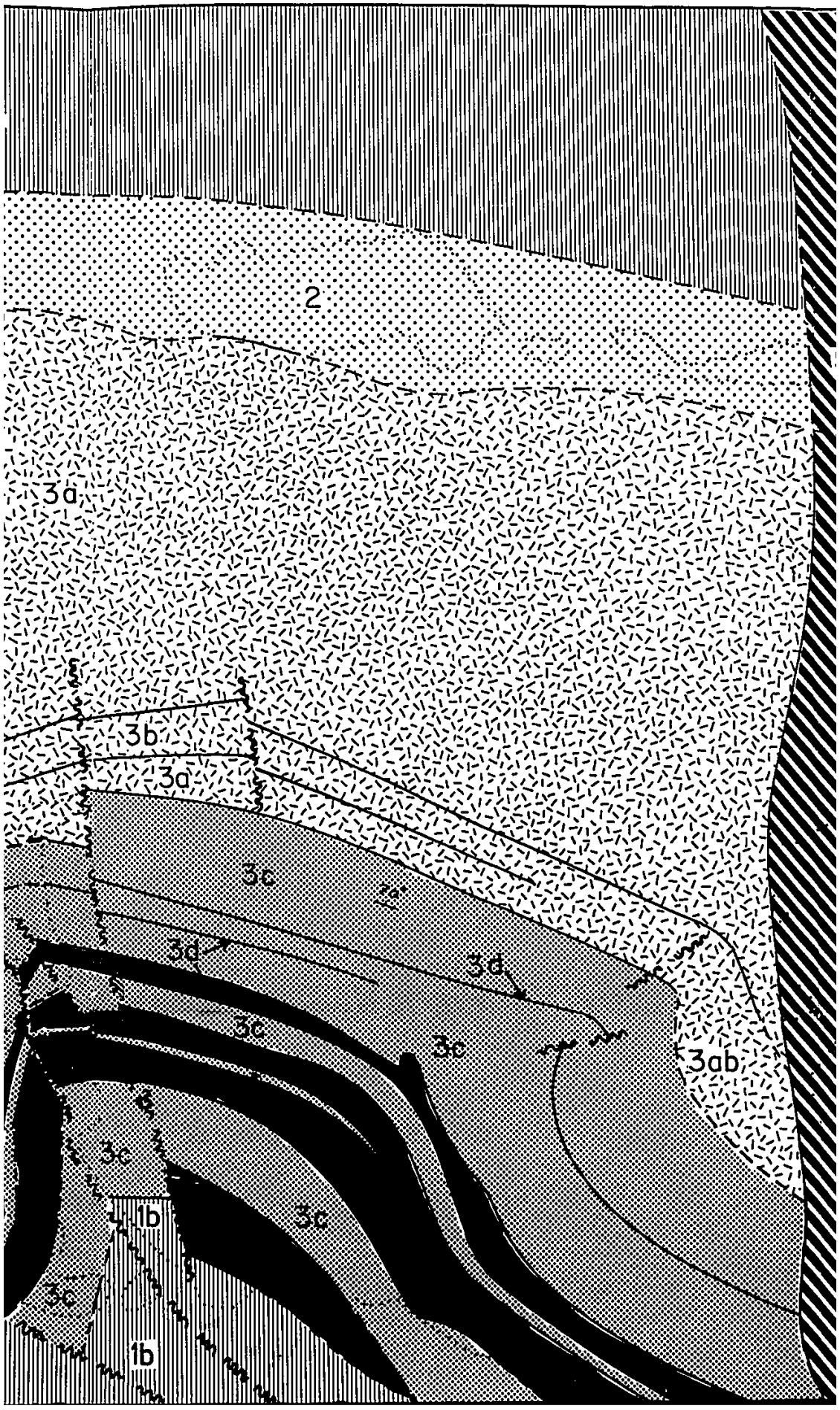
2
3a
3b
3a
3c
3d
3d
3c
3c
3ab
3c
1b
3c
3c
1b

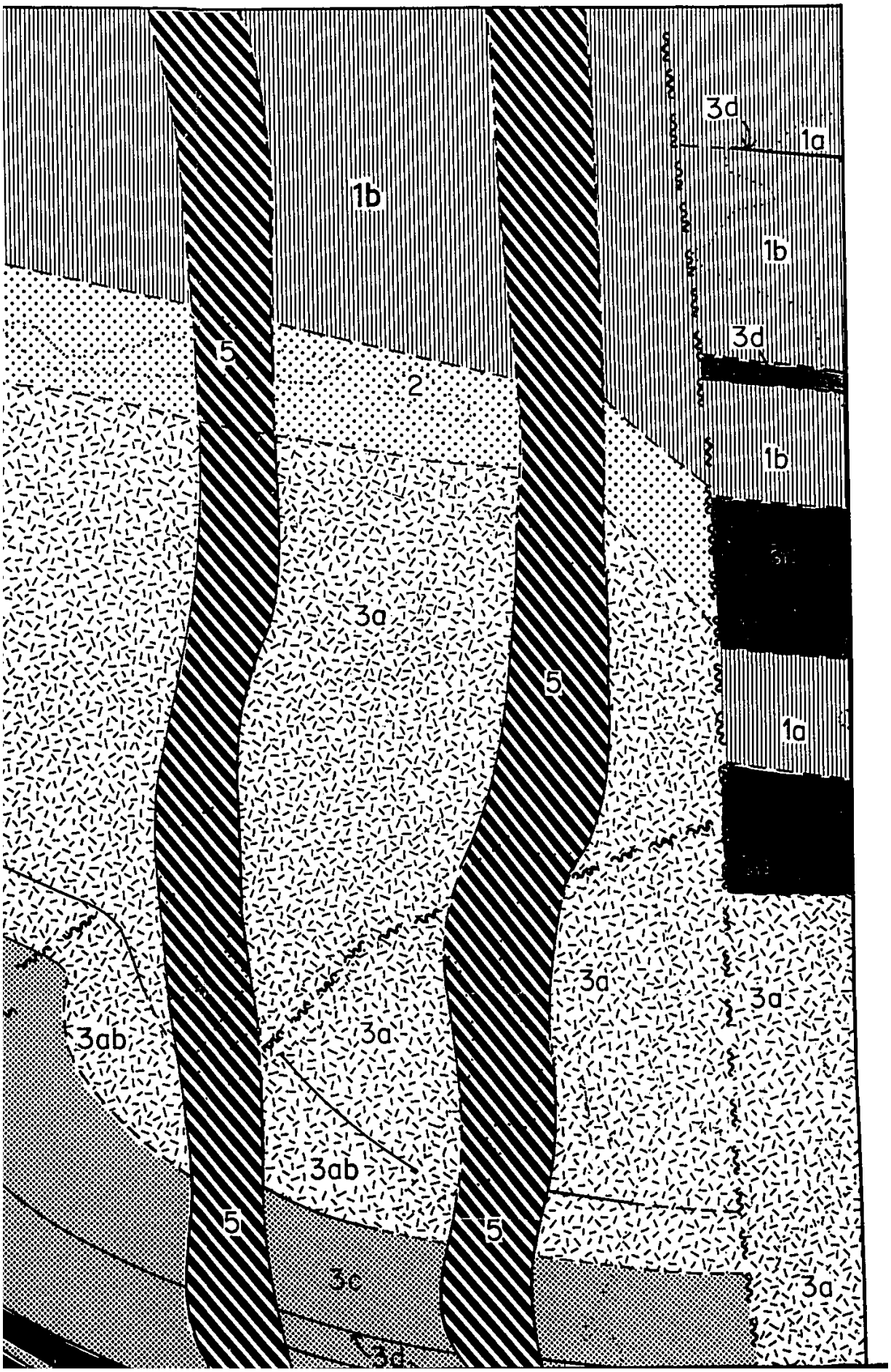
3d
1a
1b
1b
3d
1b
1a
5
2
3a
5
3a
3a
3a
3ab
3a
3ab
5
5
3c
3a
3d

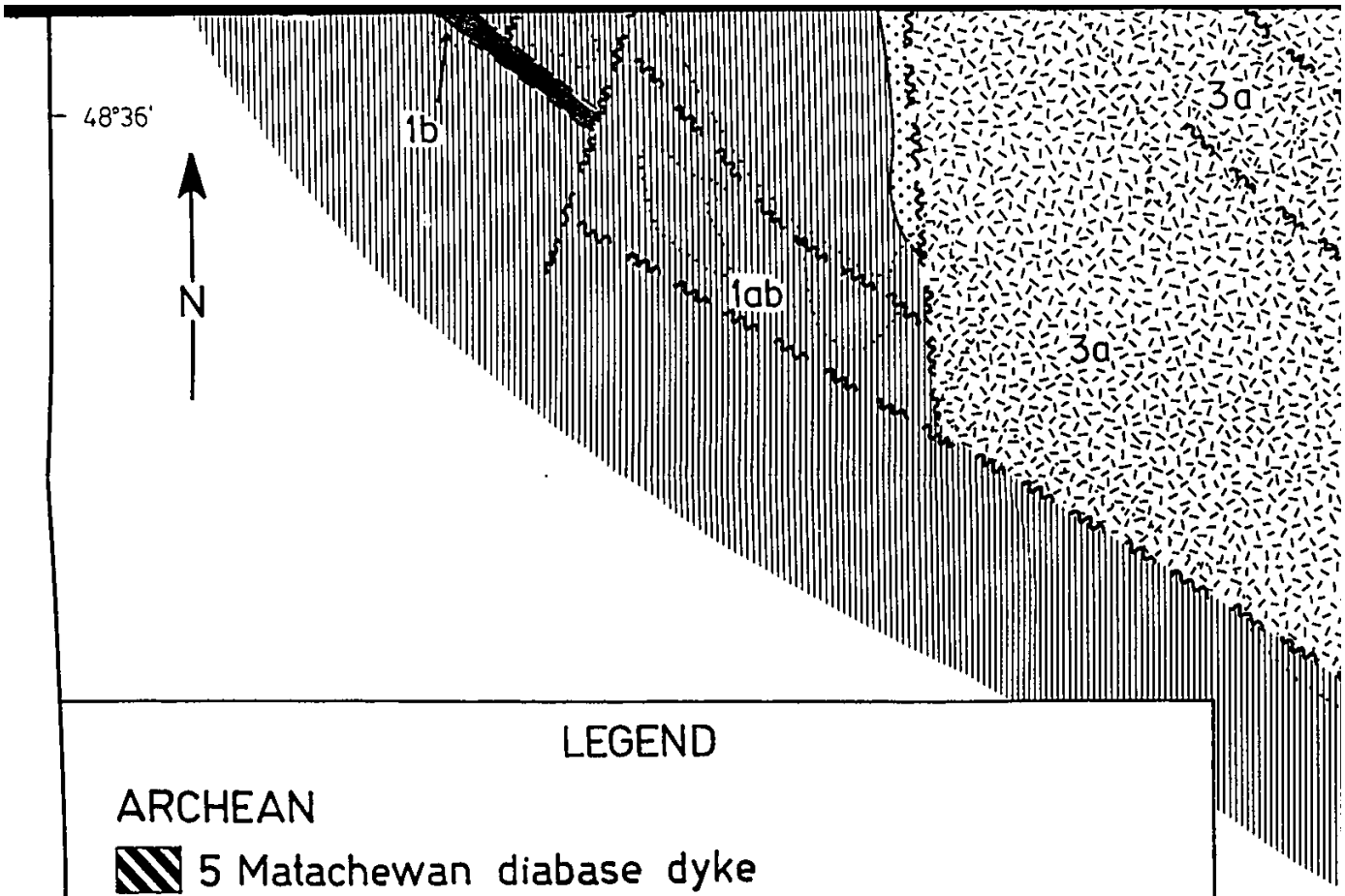

LEGEND

ARCHEAN

5 Matachewan diabase dyke

4 quartz diorite

STOUGTON-ROQUEMAURE GROUP

Centre Hill complex

3a gabbro; 3a, gabbro with branching textures; 3b melagabbro

3c clinopyroxenite

3d peridotite

2 brecciated tholeiitic basalt

1a peridotitic komatiite; 1b basaltic komatiite

boundary of rock outcrop

geological contact (observed, interpreted)

fault

70° strike and dip of layering

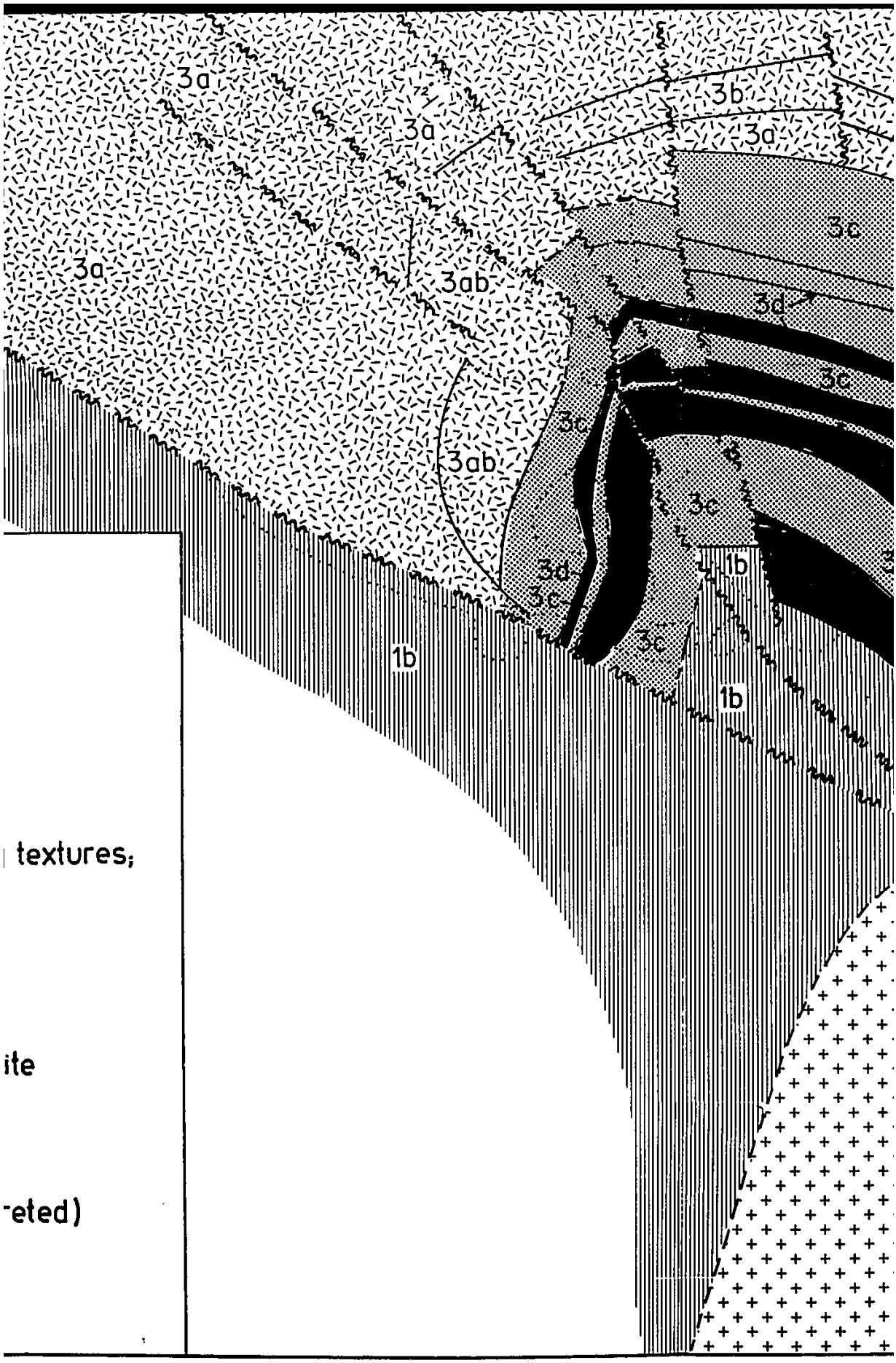

textures;

ite

-eted)


3b
3a
3c
3a'
3d
3d
3c
3c
3ab
3c
1b
3c
1b
1b
3c
3
5
4
0
100
200 m

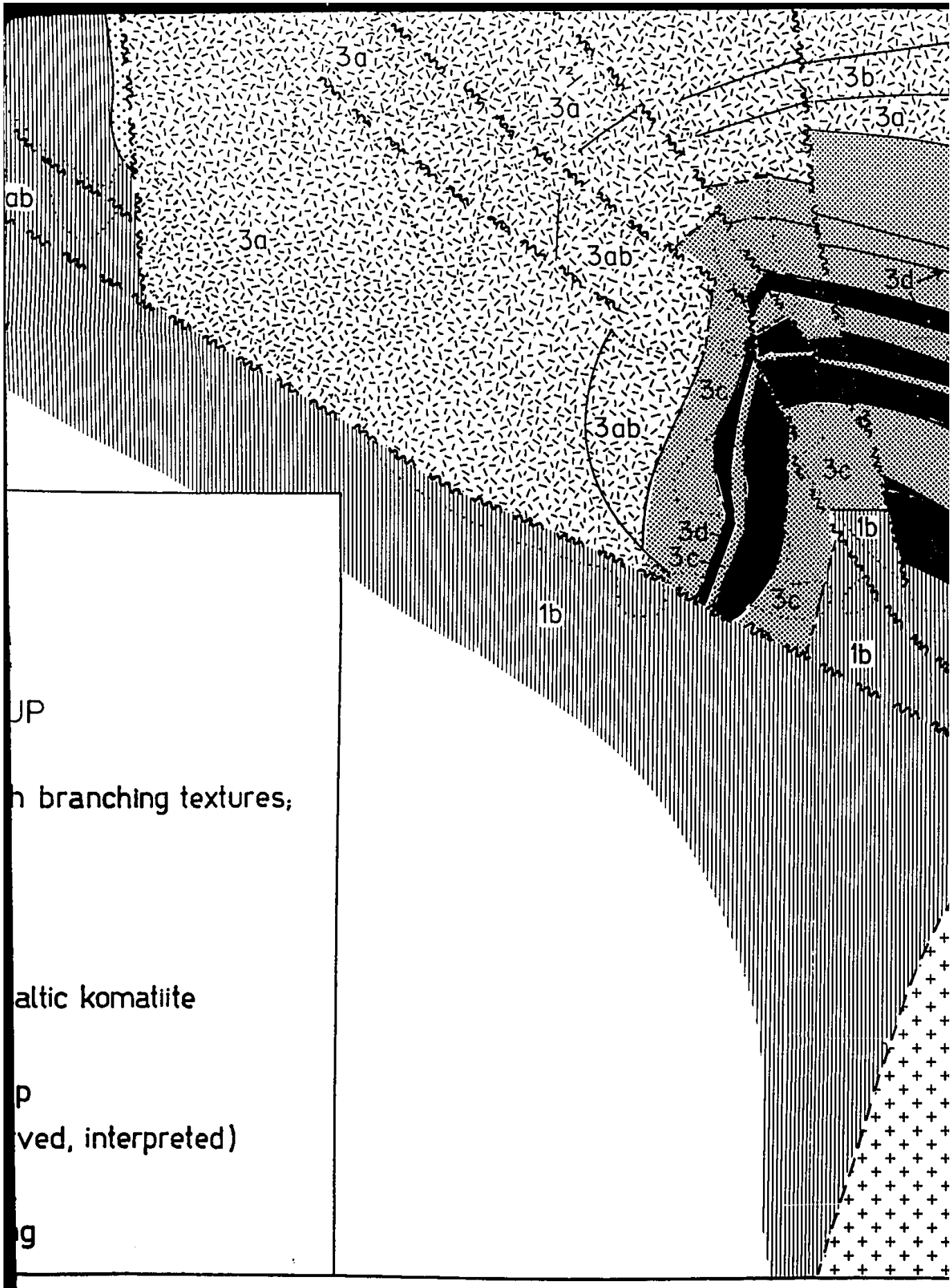

UP

n branching textures;

altic komatiite

p

ved, interpreted)

g

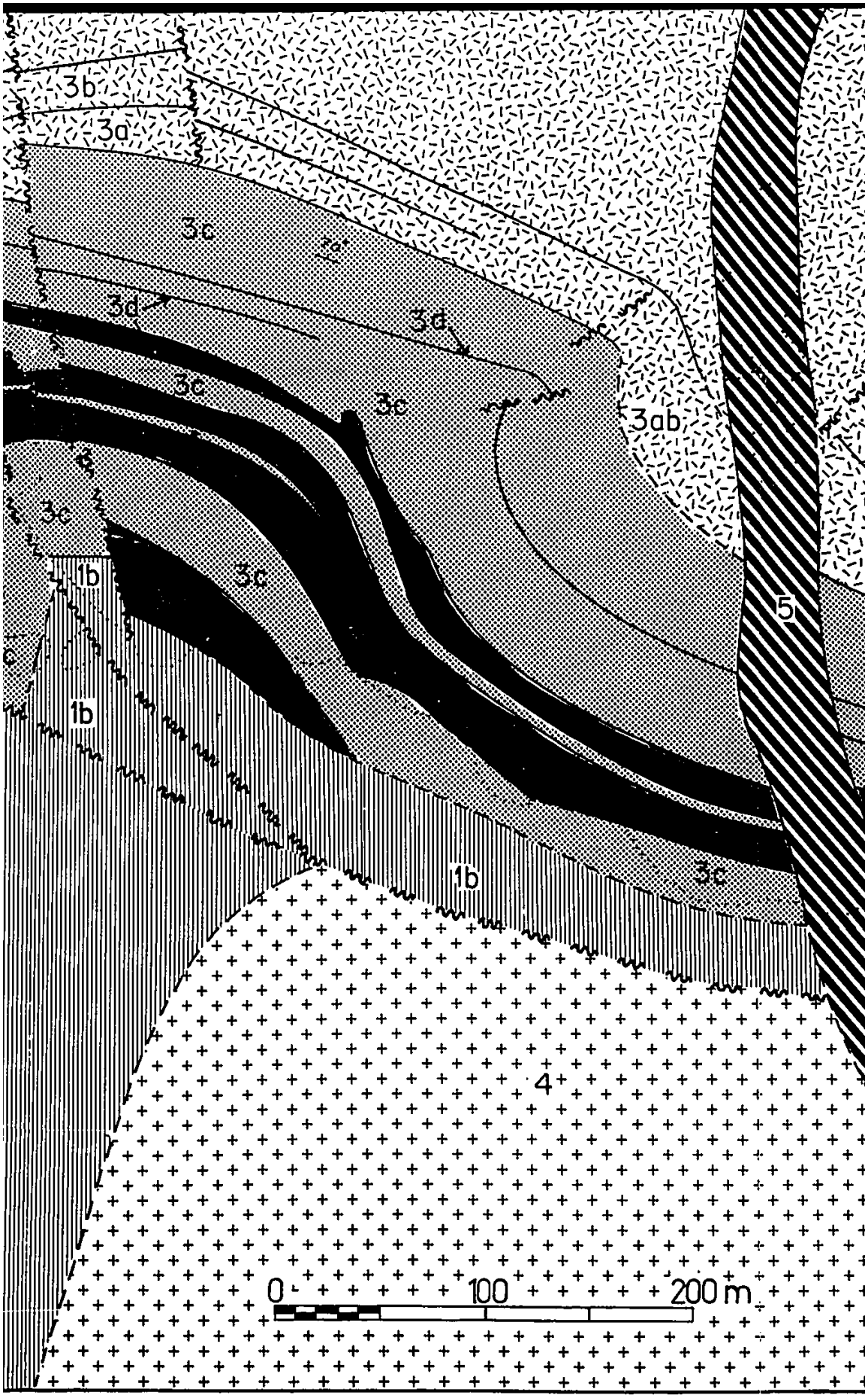
3b
3a
3c
3d
3d
3c
3c
3ab
3c
3c
1b
1b
1b
3c
3c
5
4
0
100
200 m

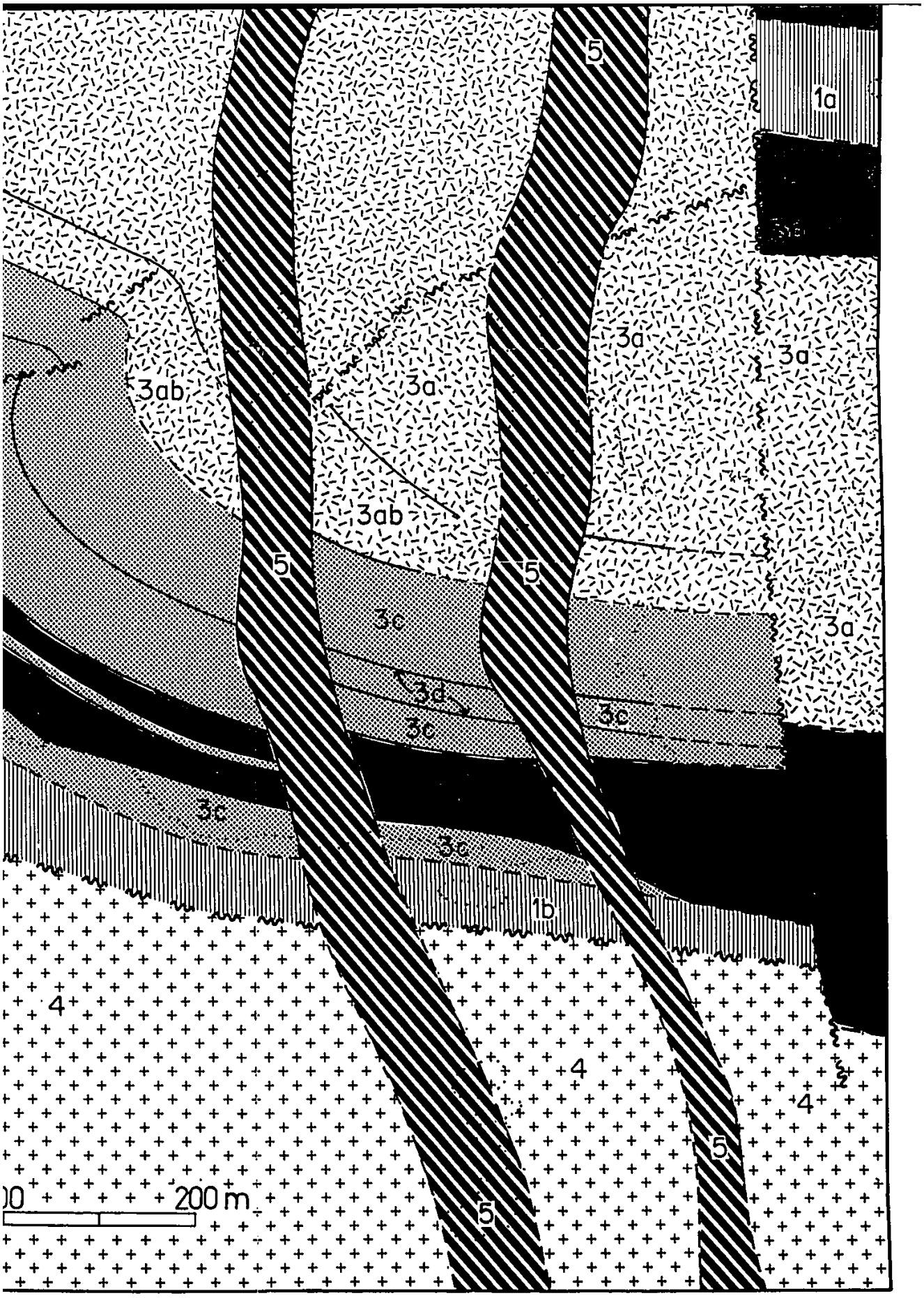
5
1a
3ab
3a
3a
3ab
3a
5
5
3c
3a
3d
3c
3c
3c
1b
4
4
4
5
5
5
200 m